UNIVERSIDAD DE CHILE
FACULTAD DE CIENCIAS FÍSICAS Y MATEMÁTICAS
DEPARTAMENTO DE INGENIERÍA ELÉCTRICA

DEVELOPMENT OF NEW HETERODYNE-DOWNCONVERTER ARCHITECTURES FOR THE NEXT GENERATION OF RADIO-ASTRONOMY INSTRUMENTATION

TESIS PARA OPTAR AL GRADO DE DOCTOR EN INGENIERÍA ELÉCTRICA

DAVID ALEJANDRO MONASTERIO LAGOS

PROFESOR GUÍA:
PATRICIO MENA MENA

PROFESOR CO-GUÍA:
NICOLÁS REYES GUZMÁN

MIEMBROS DE LA COMISIÓN:
MARCOS DÍAZ QUEZADA
ÁLVARO GONZÁLEZ GARCÍA
MATTHEW MORGAN
JOSÉ SILES PÉREZ

Este trabajo ha sido parcialmente financiado por CONICYT-PFCHA/Doctorado Nacional/2019-21190632, CONICYT-ANID project Basal AFB-170002, CONICYT-ANID Fondecyt 1180700 y Chinese Academy of Sciences, South American Center for Astronomy.

SANTIAGO DE CHILE
2022

RESUMEN DE LA MEMORIA PARA OPTAR
AL TÍTULO DE PHD EE
POR: DAVID ALEJANDRO MONASTERIO LAGOS
FECHA: 2022
PROFESSOR GUÍA: PATRICIO MENA MENA

DESARROLLO DE NUEVAS ARQUITECTURAS DE CONVERTIDOR DESCENDENTE HETERODINO PARA LA NUEVA GENERACIÓN DE INSTRUMENTACIÓN RADIO-ASTRONÓMICA

Durante los últimos años ha aumentado el interés por desarrollar nuevas arquitecturas de receptores para la próxima generación de instrumentación de radioastronomía, con el fin de reducir el tiempo de observación y estudiar nuevos casos científicos que requieran de un gran ancho de banda instantáneo. En esta tesis presentamos dos arquitecturas diferentes para receptores heterodinos, que permiten alcanzar esos objetivos.

La primera arquitectura es un convertidor descendente compacto para aplicaciones de arreglo de plano focal. Este convertidor descendente presenta una excelente pérdida de retorno y permite sintonizar su separación de banda lateral analógica con una etapa de amplificación balanceada. Además, para mejorar su rendimiento, se diseñó una metasuperficie para suprimir lazos retroalimentados en circuitos integrados de microondas estrechamente empaquetados. Se desarrolló un prototipo para la banda W que valida la arquitectura del convertidor descendente.

La segunda arquitectura es un convertidor descendente heterodino multibanda de gran ancho de banda, que cubre toda la banda RF de forma instantánea. Funciona usando multiplexación de frecuencia analógica en combinación con separación de banda lateral digital. Seleccionamos la banda W extendida (67 a 116 GHz) para validar la arquitectura. Se diseñó, construyó y caracterizó un prototipo de diplexor, que incluye un novedoso híbrido en cuadratura de última generación con un gran ancho de banda. Además, presentamos una simulación que muestra que la arquitectura propuesta tiene el potencial de cubrir todo el ancho de banda RF instantáneamente con cuatro salidas IF.

Abstract

During the last years, there has been increasing interest in developing new receiver architectures for the next generation of radio astronomy instrumentation in order to reduce the observation time and study new science cases that require more instantaneous bandwidth. In this thesis, we present two different architectures for heterodyne receivers that allow reaching those goals.

The first architecture is a compact downconverter for focal plane array applications. This downconverter presents excellent return loss and permit tuning its analog sideband separation with a balanced amplification stage. Additionally, to improve its performance, a metasurface was designed to suppress feedback loops in tightly packed microwave integrated circuit components. A prototype for the W band was developed to validate the downconverter architecture.

The second architecture is a broadband multiband heterodyne downconverter that covers the entire RF bandwidth instantaneously. It works using analog frequency multiplexing in combination with digital sideband separation. We selected the extended W band (67 to 116 GHz) to validate the architecture. A prototype diplexer, which includes a novel broadband state-of-the-art quadrature hybrid, was designed, constructed, and characterized. Moreover, we present an end-to-end simulation that shows that the proposed architecture has the potential to cover the entire RF bandwidth instantaneously with four IF outputs.

To my family.

Acknowledgments

En primer lugar, agradezco a mi profesor guía Patricio Mena por todo el apoyo, confianza y dedicación que me ha brindado en esta tesis de doctorado. Él ha sido una de las razones principales por la que el desarrollo de esta tesis ha sido expedito y sin casi ninguna complicación. Creo que el tiempo que hemos trabajado juntos ha permitido generar una relación de amistad, la que valoro mucho y espero que se mantenga en el futuro.

En segundo lugar, me gustaría agradecer a todos mis amigos y colegas del Laboratorio de Ondas Milimétricas, en particular a Camilo, Franco y Pablo. Ustedes han sido una fuente de soporte emocional durante todos los años que nos conocemos, nunca olvidaré nuestras sesiones de Smash y Rol. Espero que sigamos siendo amigos por muchos años. También quiero agradecer a Claudio Jarufe, quien me inspiró a hacer este doctorado, agradezco mucho las incontables conversaciones y ayuda que me ha dado antes y durante esta tesis.

En tercer lugar, quiero agradecer a mis amigos fuera del laboratorio, es especial a Francisco y Blas. Gracias por escuchar y aconsejarme todos estos años. También quiero agradecer a Mary, gracias por su rica comida y su indudable fe en mí. Finalmente quiero agradecer a mi familia, a mi padre Octavio, mi madre Rosalba, mi hermana María Ester. Gracias por su apoyo y confianza. Es a ustedes a quien dedico esta tesis.

Table of Content

1 Introduction **1**

1.1 Motivation . . . 1
1.2 Fundamentals . . . 1
1.2.1 Heterodyne receivers . . . 2
1.2.2 Figures of merit . . . 2
1.2.3 Mixers technologies . . . 3
1.3 Description of the general problem . . . 6
1.3.1 Focal Plane Array . . . 6
1.3.2 Multiband heterodyne receivers . . . 6
1.3.3 General requirements . . . 8
1.4 Hypothesis . . . 9
1.5 Objectives . . . 9
1.5.1 General Objective . . . 9
1.5.2 Specific objectives . . . 10
1.6 Contributions . . . 10
1.7 Outline of this thesis . . . 10

2 A Compact Sideband Separating Downconverter With Excellent Return Loss and Good Conversion Gain for the W Band **12**

2.1 Introduction . . . 12
2.2 Module Design and Construction . . . 13
2.2.1 Waveguide coupler and load . . . 16
2.2.2 Low noise amplifiers . . . 16
2.2.3 Mixers . . . 17
2.2.4 Wilkinson power divider and LO filter . . . 19
2.2.5 Simulations of the entire downconverter module . . . 20
2.2.6 Construction and assembly of the module . . . 22
2.3 Module Measurements . . . 23
2.3.1 Conversion gain and sideband rejection . . . 23
2.3.2 Return loss . . . 25
2.3.3 Noise figure . . . 27
2.4 Conclusion . . . 29

3 A Mode-Suppressing Metasurface for Large-Width MMICs Suitable for Tightly-Packaged Millimeter and Submillimeter Heterodyne Receivers 30
3.1 Introduction . . . 30
3.2 Metasurface Design and Integration into the W-Band Heterodyne Module . . . 31
3.2.1 Power Spectrum Measurements . . . 34
3.2.2 Noise Temperature Measurements . . . 35
3.3 Conclusion . . . 37

4 A 90° Waveguide Hybrid for Ultra-Broadband Operation with Low Amplitude & Phase Imbalances 38
4.1 Introduction . . . 38
4.2 Justification of the Design . . . 39
4.3 Proposed Design and Simulations . . . 40
4.4 Implementation, Measurements and Discussion . . . 42
4.5 Conclusion . . . 44

5 Development of a multiband heterodyne downconverter for the extended W band 45
5.1 Introduction . . . 45
5.2 RF Frequency Diplexer . . . 47
5.2.1 Hybrid 1 . . . 47
5.2.2 Hybrid 2 . . . 47
5.2.3 Filters . . . 48
5.2.4 Diplexer Simulation . . . 49
5.2.5 Diplexer Characterization . . . 52
5.3 Looking into the future: Proposal of a proof-of-concept wideband downconverter . . . 54
5.3.1 I/Q mixers . . . 54
5.3.2 LO distribution . . . 54
5.3.3 Additional Components . . . 55
5.3.4 Proposed design . . . 55
5.3.5 Simulations . . . 56
5.4 Conclusion . . . 58

6 Conclusions 60
6.1 General Conclusions . . . 60
6.2 Future Work . . . 61

Bibliography 62

List of Tables

2.1 Estimated average noise and gain of the module.. 22

4.1 Parameters used to model the four types of hybrids.† 40
4.2 Geometric parameters of the proposed hybrid. 41
4.3 Comparison between proposed design and other works. 44

List of Figures

1.1 Heterodyne Receiver diagram. 2
1.2 Representation of image rejection. 4
1.3 Comparison of noise temperature and frequency between the different technologies. 4
1.4 Focal Plane Array diagram. 7
1.5 Multiband Heterodyne receiver diagram. 7

2.1 Architecture of the broadband downconverter. 14
2.2 (a) Flow graph for the return loss of the module.(b) Improvement of the reflected wave when adding the 90° RF hybrid at the input for unbalanced systems. 15
2.3 Scattering parameters of the multi-branch waveguide 90^{o} hybrid simulated in HFSS. 16
2.4 LNA CGY2190 from OMMIC. 17
2.5 Schematic of the subharmonic mixer. 18
2.6 MMIC mixer. 19
2.7 Scattering parameters of the Wilkinson divider and filters simulated in HFSS. . . . 20
2.8 Simulated conversion gain of the entire module in AWR with an average LO power of 9 dBm. 21
2.9 Simulated return loss of the module in AWR. 21
2.10 Simulated sideband rejection ratio in AWR. 22
2.11 Picture of the interior of the assembled module. The inset shows details of the MMICs containing the LNA and mixer, respectively. 23
2.12 Measured conversion gain for the I/Q branches for LO frequencies of 33.5, 35, 37.5, 40, 42.5, 45, 47.5, 50 and 52.5 GHz, with an average LO power of 12 dBm. 24
2.13 Measured conversion gain with sideband separation, for LO frequencies of 35, 37.5, 40, 42.5, 45, 47.5, 50 and 52.5 GHz, with an average power of 12.3 dBm. 25
2.14 Measured SRR with an average power of 12.3 dBm.. 25
2.15 Examples of SSR improvement with changes in the bias of the amplifiers. 26
2.16 AWR simulations of the SRR considering the presence of a 96-GHz resonance between the amplifier and the mixer. 26
2.17 Test setup used to measure the return loss at the RF port. A calibration plane was used at the input port to subtract losses introduced by the setup. 27
2.18 Measured input return loss of the module for seven different bias settings. 28
2.19 Measured noise figure of the module for the I and Q branches. 28

3.1 Simulated $|S_{21}|$ and $|S_{11}|$ parameters of a transmission line inside the LNA and mixer cavities. Simulations were performed with and without the PMC metasurface. 32
3.2 Dispersion diagram of the proposed structure. 32

3.3 Representation of the cavities enclosing the amplifier and mixer. 33
3.4 Diagram of the setup used to measure the instability of the receiver at the RF and IF ports, simultaneously. 34
3.5 Power spectrum measurements. 36
3.6 Measured noise temperature with the top lid removed and the BoN structure. . . . 36

4.1 Calculated amplitude imbalance of four different types of hybrids with 10 identical branches. 40
4.2 Drawing of the proposed hybrid design indicating critical dimensions. (a) Complete CAD model. (b) E-plane view. (b) H-plane view. 41
4.3 (a) Open mechanized E-plane split-block quadrature hybrid. (b) Measurement setup. 42
4.4 Simulated and measured reflection and isolation. 43
4.5 (a) Simulated and measured amplitude imbalance. (b) Simulated and measured phase imbalance, centered in 90°. 44

5.1 General diagram of the multiband receiver. 46
5.2 Concept of a multiband heterodyne receiver with digital 2SB receivers for the extended W band. 46
5.3 Power flow diagrams explaining the fundamental working principle of the hybrid-based diplexer. 48
5.4 (a) Drawing of the proposed hybrid 2, indicating critical dimensions (in mm). The input/outputs are standard WR-10 waveguides, and each of the 8 branch lines has the same dimensions. (b) Simulated S-parameters. 49
5.5 (a) E-plane (top) and H-plane (botttom) views of the proposed high-pass filter design indicating critical dimensions (in mm). The input/output are standard WR-10 waveguides. (b) Simulated S-parameters. 50
5.6 (a) Drawing of E-plane of the proposed filter design indicating critical dimensions (in mm). The input/output are standard WR-10 waveguides. (b)S parameter simulation made in HFSS. 50
5.7 (a) HFSS model of the complete diplexer. (b)Simulated S-parameters. 51
5.8 Simulated equivalent noise temperature of the diplexer made in Cadence AWR Microwave office. 51
5.9 Picture of the constructed split-block diplexer. 52
5.10 Proposed setup configurations to measure scalar parameters. 53
5.11 (a) Scalar S parameter measurements results of the constructed diplexer. (b) Pictures obtained during metrology measurements show examples of significant construction errors. 54
5.12 Final layout of I/Q mixer CHARM012SB. 55
5.13 Diagram for the first prototype of a diplexer-based downconverter module. 56
5.14 (a) CAD image of the proposed mixer block. (b) Image of one of the mixers with all its components including the MMIC, RF and LO probes, and IF paths with a layer change. 57
5.15 AWR non-linear simulations of the normalized IF power of the proposed downconverter prototype with an ideal IF hybrid at its output. 58
5.16 Simulation of SRR utilizing the digital sideband separation method. 58

Chapter 1

Introduction

1.1 Motivation

Northern Chilean skies are privileged with excellent atmospheric conditions for astronomical observations. This attribute has motivated the installation of many astronomical observatories over the past half-century [1]. Many of these observatories are radio-telescopes such as the 1.2-m Southern Millimeter Wave telescope (1982), Atacama Pathfinder Experiment (2004), or Atacama Large Millimeter Array (2011). There are plans to continue the installation of new radio telescopes with different science objectives, such as the relocation of the Osaka 1.85-m Submilimiter Telescope to Chile [2] and the construction of the Fred Young Submillimeter Telescope [3] in the near future. It is this trend, in conjunction with international collaborations, that gives Chilean scientists and engineers an opportunity to be a participant not only in the operation but also in the development of new technologies that can be implemented for these telescopes. This initiative has taken form in the Centro de Excelencia en Astrofísica y Tecnologías Afines (CATA). The research presented in this work will be developed in one of its laboratories, the Millimeter Wave Laboratory (MWL) of Universidad de Chile.

One of the most important components of a radio-telescope is its receiver, the device that transforms the light from the sky into an electric signal that can be analyzed [4]. In recent years, there has been an interest in the international scientific community to develop new types of receiver architectures to study new science cases and reduce the telescope observation time [5]. The observation time is defined as the time that needs a telescope to completely resolve a specific sky source and is usually associated with the sensitivity of the receiver [4]. For this PhD thesis, we will center our discussion on heterodyne receivers and, more specifically, on one of their core components, the downconverter. In this work, we present two different downconverter architectures that have the potential to be implemented in the current and future radio astronomical observatories.

1.2 Fundamentals

Before we explain the general problem that needs to be solved, a series of fundamental concepts need to be introduced for a better understanding of the problem. The following subsections will give the reader the fundamental knowledge to understand this PhD thesis.

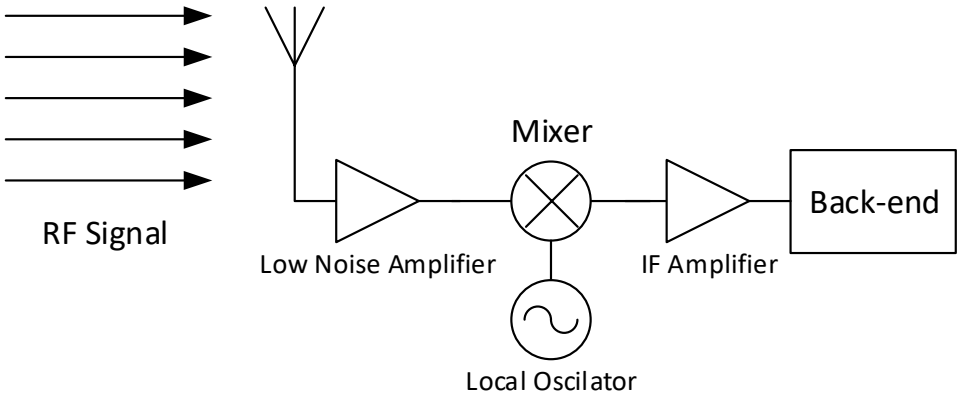

Figure 1.1: Heterodyne Receiver diagram. In its simpler form, the incoming RF signal is captured by an antenna and fed into a transmission line (such as waveguides or coaxial cables). The signal is then amplified by a low noise amplifier (LNA), a process that reduces the overall noise of the receiver increasing its sensibility. It is important to note that LNA technology is not available at high frequencies, so it is not always possible to include this stage. The signal then passes through a non-linear device called a mixer where it is intermodulated with a reference signal called a Local Oscillator (LO). The signal is then downconverted by this process to the IF frequency (after filtering all the undesired intermodulation products). The IF signal is then usually amplified and goes to the back-end (the device that processes the signal for a specific purpose such as a spectrometer.) [6].

1.2.1 Heterodyne receivers

As stated in section 1.1, in radio-astronomy, the receiver is a device that transforms electromagnetic radiation from the sky into a signal that can be analyzed by a computer. There are several types of implementations to make this process, but one of the most used is the heterodyne receiver. This type of receiver can transform, with a linear response, the incoming electromagnetic radiation at a certain frequency (RF) into a lower frequency called Intermediate Frequency (IF). This property allows making a spectrographic analysis of the incoming electromagnetic radiation utilizing standard electronic components to process the IF signal [4]. The general structure of a heterodyne receiver is presented in Fig. 1.1.

We will call a downconverter to a group of components (such as amplifier and mixers) that allows the downconversion of the RF signal and meets several requirements that will be discussed in section 1.3.

1.2.2 Figures of merit

1. **RF Bandwidth:** The bandwidth in which the receiver will work is an important aspect that will determine the type of technology that is needed for its construction. The size of the RF bandwidth is determined by the operational bandwidth of all the components of the receiver up to the mixer element, however this bandwidth is usually not proceeded instantaneously by the back-end, as it will be limited by the IF bandwidth. For radio astronomy, large bandwidth systems are usually preferred, as they allow observing an important number of

spectral lines. Moreover, they are also preferred since less instrumentation is needed in the telescope [7].

2. **Noise:** Another characteristic that is important for a downconverter is its noise figure, as it determines the sensitivity of the receiver. All microwave components generate noise, for radioastronomy is an important concern given the low intensity of the signals that come from the sky. There are several types of noise sources, such as thermal, shot and flicker (related to the material and construction process of the electronics). For a receiver, we can define its equivalent noise temperature as the physical temperature of a resistor that gives the same noise power at the input of the receiver. Therefore, using the total power at the output of the receiver is given by the Rayleigh-Jeans approximation $P = GkT_{rec}B$, with G the gain of the receiver, k the Boltzmann constant, B is the frequency bandwidth and T_{rec} is the physical temperature of the equivalent resistor [6]. In a receiver chain, its equivalent noise can be calculated by the noise contribution of each individual component using the Friss equation for noise. This equation also indicates that the gain of the first elements of the chain will have a larger impact in subsequent elements, so a LNA is preferred as the first element. Unfortunately, this is not always possible due to technological limitation or because passive elements such a orthomode transducer (with separates polarization) are needed. The noise contribution and losses of passive devices are dependent on their physical temperature, so there are usually cooled down if placed as the first elements in a receiver chain.

3. **Image rejection:** Sideband separation receivers, in contrast with the standard double-sideband receivers, are capable of separating the lower sideband (LSB) and upper sideband (USB) into two different outputs. A general representation of the difference between these two types of receivers, showing image rejection, is presented in Fig. 1.2. Sideband separation is not perfect in reality, due to not ideal components. The ratio between the received band and the leakage of the image band is called the Sideband Rejection Ratio (SRR). Image rejection is a desirable feature in radio astronomy, because it reduces the noise, increases observation efficiency, and reduces radio frequency interference [8].

4. **IF Bandwidth:** IF bandwidth has become an important concern for radio astronomy, given the interest in simultaneous observations of different spectral lines. Moreover, wider IF bandwidths would solve the always present need to reduce observation time. This increase in bandwidth has become achievable in recent years due to the increment in processing power of the back-end systems.

1.2.3 Mixers technologies

Several types of mixer technologies exists for implementation in downconverters [9]. They include superconductor insulator superconductor (SIS), hot-electron bolometers (HEBs), Schottky mixers, and hot electron mobility transistor (HEMT) mixers. This section presents the general characteristics of each type stressing its advantages and limitations. Figure 1.3 shows some examples of the noise performance of the previously mentioned technologies except for HEMT mixers, as their noise temperature is not usually reported.

1. **SIS mixers:** These devices use a SIS junction which has strong nonlinear properties to generate the heterodyne downconversion. They are the most popular alternative for mixing in the submillimeter wave range in radio-astronomy applications. This choice can be explained

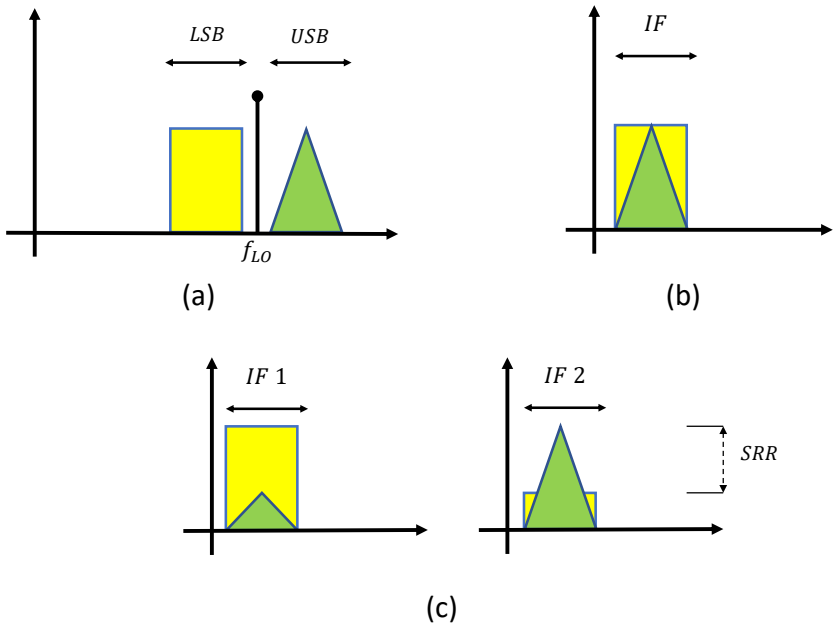

Figure 1.2: Representation of image rejection. (a) RF signal observed by a receiver at a LO frequency f_0. (b) Downconverted signal with a double side band receiver, the USB and LSB are overlapped into the same IF bandwidth. (c) Downconverted signal using sideband separation receiver, the IF is divided into two outputs, one receive the LSB and the other the USB.

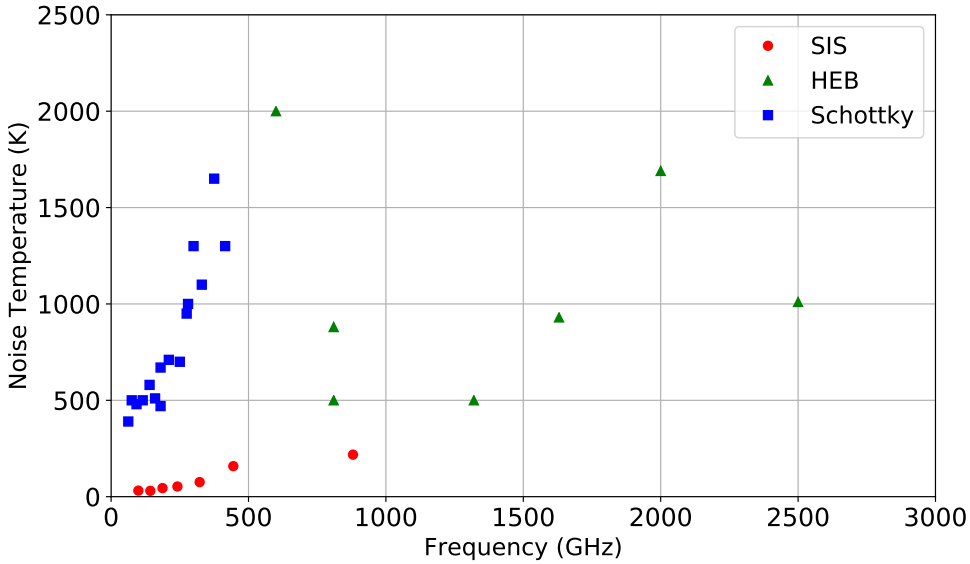

Figure 1.3: Comparison of noise temperature and frequency between the different technologies.

because of its low noise and high-frequency operation, i.e. from around 100 GHz to the THz range (see [10] and references therein). They can be implemented with sideband separation capabilities and have a large IF bandwidth. Their use raises some practical problems. First, it needs cryogenic operation given that it is a superconductor junction. Second, it needs the use of electromagnets to suppress the Josephson effect.

2. **HEB Mixers:** HEB technology consists generally of a superconductor or semiconductor at a very low temperature, in which the electrons are weakly coupled to the structure. Then, any interaction with electromagnetic radiation generates hot electrons that increase its temperature. HEBs have two different applications as a receiver. The first and most popular one is as a detector and, the second, as a mixer by adding a LO signal that interacts with the electrons generating a non-linear response. Originally, mixer operation could achieve a very limited IF range in the MHz range. However, the interest in this type of mixer was renewed 30 years ago with the realization that NbN superconductors exhibit a hot-electron effect and that, if constructed properly, can achieve up to 4 GHz of IF bandwidth. Currently, this type of mixer has very low noise, operation frequency above 600 GHz and the IF range that can achieve is in the vicinity of 10 GHz [11] and [12]. As with the SIS mixer, cryogenics is needed for its operation [10].

3. **Schottky Mixers:** This type of mixer uses a solid-state semiconductor-metal junction called Schottky barrier diodes. They have good performance at millimeter and sub-millimeter frequencies but have more noise than SIS and HEB mixers [13]. The increase in noise is produced by three factors, thermal noise produced by the diode series resistance, shot noise produced by current flow in the junction, and flicker noise produced by imperfections in the crystalline structure of the semiconductor [6] [14]. To overcome this limitation, they are usually combined with the use of a RF LNA stage before the mixer, to reduce the overall noise of the receiver. Schottky mixers have the advantage that can operate at room temperature and, moreover, their noise can be reduced if they are cooled down to cryogenic temperatures. It should be pointed out that if the mixer is used with a RF LNA with low noise and high gain, the mixer should not be necessarily operated at cryogenic temperature to achieve a good downconverter performance. An extra advantage is the existence of commercially available processes for construction, giving more versatility to the design when compared to HEB and SIS mixers. This type of receiver is preferred at lower frequencies and is generally used in space communications [15]. These devices have also the advantage that can be manufactured using a Monolithic Microwave Integrated Circuit (MMIC) technology, which allows miniaturization of the designs and integration of the diodes with other microwave components.

4. **HEMT mixers:** The non-linearity in the saturation point of an amplifier can be used to generate heterodyne mixing. In recent years, several mixers of this type have been developed [16], [17] and [18]. These devices can be manufactured in a very small size because the mixer and the LNA can be implemented on the same MMIC. This is not possible with Schottky diodes because their manufacture requires two different processes that can not be implemented on the same integrated circuit. Unfortunately, the transistor-based mixers have more noise temperature and less operational bandwidth than its diode counterpart. This characteristic makes them less attractive to radio astronomy but more useful for communications and radar applications.

During the last decade, LNA HEMT technology has been increasing its operating frequency over 100 GHz [10]. This alternative, in combination with other possibilities that can be available in the future, like the superconductor parametric amplifier [19], gives technologies that presents more noise an opportunity to compete with less noisy technologies at higher frequencies.

1.3 Description of the general problem

In recent years, radio astronomical heterodyne receivers have increased their sensitivity due to the improvement in semiconductor and superconductor technologies. However, there is a theoretical value in which sensitivity cannot be reduced further, this barrier is called the standard quantum limit and current generation receivers are fast approaching this number and can not be substantially improved. However, alternative approaches can be used instead to reduce the observation time needed to resolve an astronomical source. Two different approaches, that involve the use of parallel outputs to achieve observational time reduction, will be discussed in the following subsections.

1.3.1 Focal Plane Array

In focal plane arrays (FPAs), an array of receivers (pixels) is positioned in the focal plane of a telescope or antenna. To illustrate this we present the general configuration of a FPA in Fig 1.4, which allows a reduction in the observation time by a factor equal to the number of pixels of the array, by parallel processing of its outputs. Particular attention has to be given to the optics of each individual receiver, as they should not interact with each other in the far-field, making the distance between receivers a design factor. As explained in [10], the minimum distances between elements for a coherent system must be greater than twice the focal ratio of the telescope times the wavelength. This separation produces an angular distance of more than two times the full width at half the maximum (FWHM) beamwidth of the individual optic of the receiver in the far-field. However, to achieve this minimum size, FPA receivers must be designed to be compact by nature, especially at their cross-section.

1.3.2 Multiband heterodyne receivers

A multiband heterodyne receiver is a novel approach for reducing observation time. We present in Fig. 1.5 a general diagram of this type of receiver. It separates the incoming RF bandwidth into several smaller sub-bands with the use of a frequency multiplexer. Each band has an individual heterodyne receiver that will be processed independently and will allow to obtain several sections of the RF spectrum instantaneously. The incorporation of the multiplexer element will decrease the sensitivity of the receiver and special attention must be given to its losses. This type of architecture was proposed for radio-astronomy in [20].

Multiband heterodyne receivers present a solution for the multiple-line-spectroscopy problem that have the observations of high variability object such as quasars [21], where instantaneous multiple spectrum lines are needed. Despite the possibility of solving this problem and reducing the observation time, not much work has been invested in developing this type of architecture in the area, with only one functional astronomic receiver of this type currently in operation [22]. One of the main reasons for this situation is the limitation of IF processing capabilities, but in recent years, with the development of faster digital processing platforms, this limitation can be overcome.

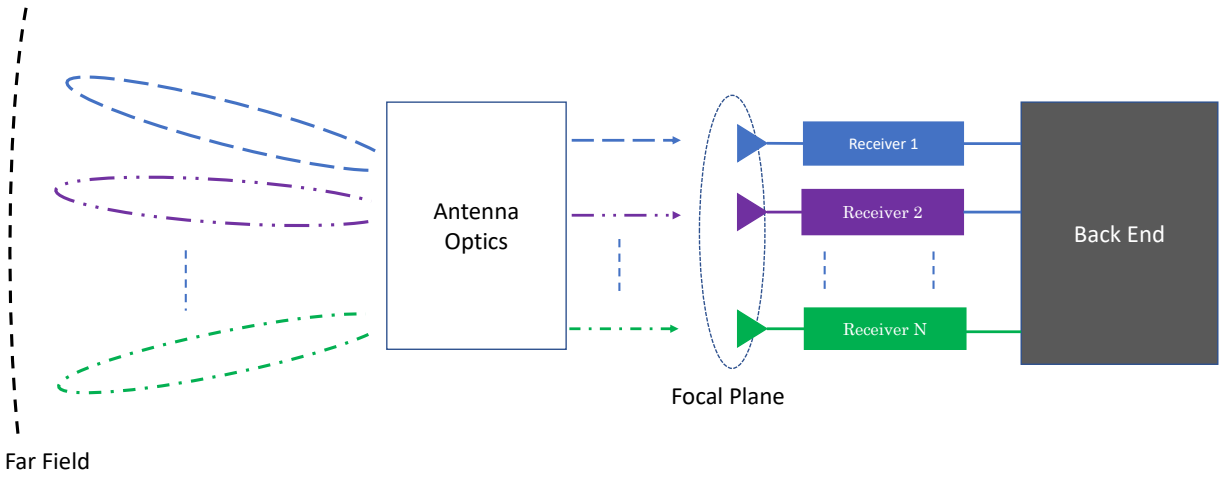

Figure 1.4: Focal Plane Array diagram. Each receiver covers a different direction in the far-field (in different color) and they are preceded in parallel by the back-end.

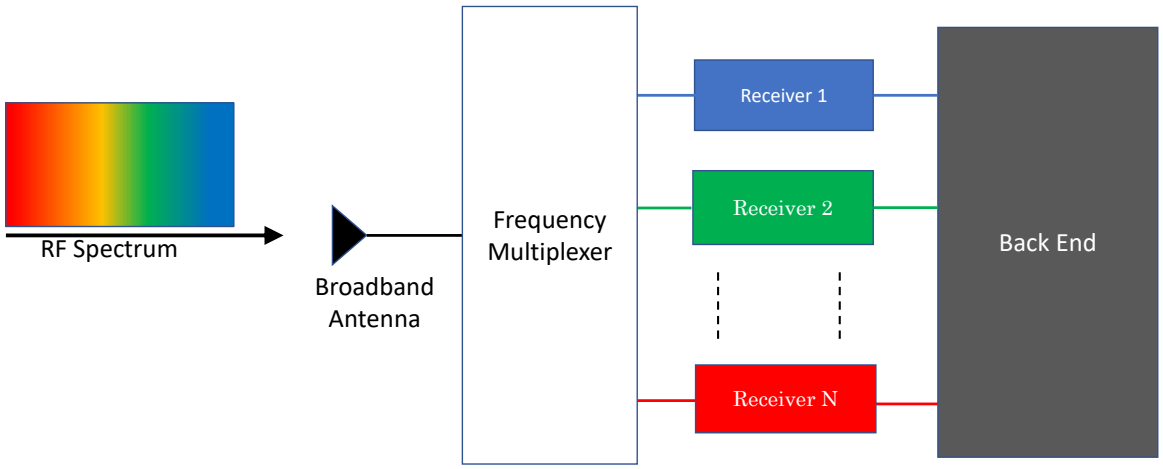

Figure 1.5: Multiband Heterodyne receiver diagram. Each receiver covers a different sub-band (in different color) of the incoming RF spectrum and they are preceded in parallel by the back-end.

1.3.3 General requirements

Before proposing a specific solution for the general problem, several key requirements are needed to be determined to make a practical implementation. The first requirement is the frequency range of operation. The selection for this thesis is made considering the equipment currently available in the MWL, the interest of the scientific community, and concrete instrumentation projects. These three considerations have a common denominator, the extended W band (67-116 GHz). The MWL is currently capable of fully characterizing this frequency range (except for the last 4 GHz). The interest of the scientific community in large bandwidth systems has been increasing in the last few years. An example is the ALMA Band 2+ proposal [23]. Concrete examples of the instrumentation projects that motivated this research were the possible upgrade of the TianMa Shanghai radio telescope to the W band using FPA, and the upgrade of the Southern Millimeter Wave Telescope (SMWT) receiver to incorporate dual-polarization optics in an extended frequency range.

The second requirement is to determine the specific type of technology that is going to be used. Given the capabilities and resources of the MWL, the use of superconductor mixers is not a viable option for this thesis. The operational frequency range also limits the option of HEMT mixers, so we have selected Schottky-based receivers. Schottky receivers work well in the extended W band and there are commercial processes available for the design of MMICs. Moreover, the capability of operation at room temperature makes them a more versatile solution for different applications. There are several examples of FPA applications using Schottky mixers, such as [24][25][26]. Reference [26] is of particular interest because of its frequency range and the use of a commercially available process for the downconverter mixer.

The third requirement is to determine the mixer configuration to be used. There are several types such as single-ended, balanced, double-balanced, or sub-harmonic. Each configuration has its own characteristics and each is a viable option for implementation. The selection therefore was made from a practical standpoint. The MWL begun research of sub-harmonic mixers inspired by the receiver presented in [26] and generated a functional MMIC mixer design [27] and can be used for thesis. This configuration has also the advantage that needs a LO signal equals to half the frequency or the RF. Fortunately, commercially available mid-power amplifiers exist for the LO frequency range required for the extended W band [28], so it is easier to drive multiple pixels for FPA applications, and requirements of LO power consumption can be lessened. For the reasons mentioned above, a sub-harmonic mixer design was selected.

The fourth requirement is the inclusion of side-band separation. With image rejection, the architecture will need a RF quadrature hybrid to obtain I/Q simultaneous IF outputs. These outputs will be connected to an IF quadrature hybrid to complete the sideband separation configuration. This last hybrid can be implemented analogically or digitally [29].

The fifth requirement is to determine the IF bandwidth. Large IF bandwidth is necessary for multi-line spectroscopy. For this work, we have selected an IF bandwidth of 10 MHz to 12.25 GHz. Lower frequencies will be limited by the bandwidth of the bias circuits needed for the IF amplifiers. The upper-frequency limit was determined by two factors. The first one is that the current ALMA receiver utilizes an upper IF frequency limit of 12 GHz. The second factor is that with 12.25 GHz we can cover the entire extended W band with four IF outputs. This aspect is crucial for the design of a multiband heterodyne receiver.

The last requirement is to determine the size of the module. For a multiband heterodyne receiver the size has no actual significance, however, it is of significant importance for FPA applications. Given that the pixel separation depends on the optics on the complete receiver array, there is not an actual size limitation imposed. However, to easily test the module, the use of standard waveguide flanges and coaxial connectors are needed. Therefore, the size of the module must be the minimum required to use standard interfaces. However, these modules could be further reduced in size if custom interfaces are present.

No specific general noise requirements will be given, as this development will use commercial technologies and thus will severely limit the achievable noise value. To overcome this factor, an external LNA such as [30] can be used before the downconverter.

Back-end requirements are also not specified, as we do not have a specific science case. However, for the multiband heterodyne receiver architecture, the AD/C bandwidth must be sufficient to process the entire IF bandwidth instantaneously with a specific number of parallel outputs.

With these requirements set, we can now propose a solution to the general problem. This solution will be formulated as the objective of the PhD thesis in section 1.5.

1.4 Hypothesis

Several hypotheses permit us to address this work. The most important ones are enumerated below.

1. The proposed FPA downconverter design will meet all its specifications with the use of a custom MMIC mixer using a commercial foundry, a commercially available LNA, and the manufacturing resources available at the MWL.

2. A frequency diplexer that covers the entire extended W band can be manufactured using the high precision machining available in the MWL.

3. The proposed multiband downconverter will cover the entire RF spectrum utilizing an analog diplexer combined with digital sideband separation.

1.5 Objectives

1.5.1 General Objective

Design and implementation of heterodyne downconverter architectures for the next generation receivers for radio astronomy, capable of reducing the observation time with parallel IF outputs. The proposed downconverters will be compatible with digital side-band separation to extend the instantaneous IF bandwidth coverage. The downconverter architectures will be tested using commercially available MMIC technology.

1.5.2 Specific objectives

1. Design, fabricate, and characterize a compact module with for FPA application for the extended W band. The module must have a balanced amplification stage, return loss better than 10 dB, and analog SRR better than 10 dB. The cross-section area of this module should be no larger than a standard WR-10 flange.

2. Design, fabricate, and characterize a frequency diplexer suitable for multiband downconverter applications for the extended W band.

3. Design a multiband downconverter module for the extended W band. The module must cover instantaneously the entire RF bandwidth with four IF outputs and two LO signals.

1.6 Contributions

This work resulted in the following contributions:

1. Development of a compact heterodyne downconverter suitable for FPA, with a novel balanced amplification stage that has excellent return loss and allows optimization of the SRR.

2. Development of a metamaterial structure to suppress oscillations in tightly packed microwave components.

3. Development of a novel broadband quadrature hybrid, with state-of-the-art performance, that can be used in radio astronomic applications. This design was successfully validated for the extended W band and we are currently waiting for experimental results made by Chalmers University of the design at a higher frequency band.

4. Development of a multiband downconverter for the extended W band with instantaneous RF bandwidth converge, based on analog multiplexing and digital sideband separation.

5. Continuation in the research line of development of microwave devices at high frequency in the Millimeter Wave Laboratory at Universidad de Chile.

6. Formation of human capital through the supervision of one engineering thesis. The focus of this thesis was the design of microwave components that are associated with the research of the multiband downconverter architecture.

1.7 Outline of this thesis

- Chapter 2 of this thesis presents a publication [31] related to contribution N° 1.

- Chapter 3 presents a publication [32] related to contribution N° 2.

- Chapter 4 presents the work made by Universidad de Chile related to contribution N° 3. The work is presented in the form of a paper draft and will serve as the base for a combined publication with Chalmers University that is expected by the end of 2022 [33].

- Chapter 5 presents the work related to contribution N° 4. The first half of the chapter presents the development of a frequency diplexer. The second half presents simulations of a proof of concept of the proposed downconverter architecture. This work has generated a presentation at the ALMA Front End Development (Virtual) Conference 2021 [34] and will be also presented at the 32nd International Symposium on Space Terahertz Technology later in 2022. This work presented in this chapter can be considered as current (first half) and future work (second half).

- Chapter 6 contains the general conclusions of this thesis, as well as the proposal of the future work needed for the development of the proposed architectures.

Chapter 2

A Compact Sideband Separating Downconverter With Excellent Return Loss and Good Conversion Gain for the W Band

David Monasterio, Claudio Jarufe, Diego Gallardo, Nicolás Reyes, F. Patricio Mena and Leonardo Bronfman

Abstract: We have developed a sideband separating receiver module for the W band (75 - 110 GHz) that has been designed with a scalable and compact architecture allowing easy integration into larger systems, like focal plane arrays. The receiver includes a high-frequency amplification stage giving it a good conversion gain and, most importantly, due to its original architecture, excellent return losses. The latter permits, if needed, efficient incorporation of further amplification prior to mixing. The module is based on a 90° hybrid followed by an amplification stage and broadband mixers. As amplification stage we rely on commercial low-noise amplifier chips that use the 70-nm metamorphic-high-electron-mobility process from OMMIC. The downconverter is a subharmonic mixer designed as a monolithic microwave integrated circuit and fabricated using the standard gallium-arsenide Schottky diode process from United Monolithic Semiconductor. The size of the module is 50 mm × 25 mm × 20 mm and shows good performance with an input return loss above 12 dB in the entire band, an average conversion gain of 5 dB, and sideband rejection ratio above 10 dB in the majority of the band. The primary motivation of this work has been radio-astronomy, but other areas like imaging, telecommunications or remote sensing can benefit from such compactness and integrability into multibeam systems.

2.1 Introduction

Interest in constructing focal plane arrays (FPAs) has been growing over the last years. The potential of simultaneous detection using a large number of receiver elements make them very interesting for applications such as radio-astronomy, millimeter wave imaging systems, satellite communications and earth remote sensing [15, 35, 36, 24]. To achieve high-density multibeam

systems, receivers need to be compact. In fact, their construction has been changing from using discrete components to more modular designs with higher level of integration [37]. As part of this effort, several compact modules that incorporate one or more low noise amplifiers in front of a down-converting stage have been developed. In [26] a W band low noise receiver that could be used as a sideband separating (2SB) receiver is presented, although no measurements of image rejection are provided. The module is intended for cryogenic operation. When cooled down, the noise is 33 K in average and its gain is above 15 dB. A double sideband receiver module from 140 to 180 GHz is presented in [25]. In cryogenic operation, measured noise temperature and gain are above 50 K and 10 dB, respectively. In both devices it is not possible to separate the high-frequency amplification from the down-converting stages. This characteristic can become a drawback for some applications. For example, radio astronomical applications require the low noise amplifier (LNA) to operate at low temperatures. Therefore, in FPAs with a high number of pixels, due to cooling restrictions and to provide easier replacement of components, it would be more advantageous to have the down-converting stage separated from the LNA while maintaining a compact design. A 2SB Schottky receiver is presented in [4] that works from 320 to 370 GHz integrating two subharmonic mixers followed by low frequency LNAs. It shows a image rejection better than 15 dB at 340 GHz and a noise figure above 10 dB. The main limitations of this receiver are that the loads for the isolated ports are not included in the block and its reduced fractional bandwidth. Furthermore, no measurement of the input return loss for the RF path is presented.

In this article, we present the design and construction of a low-noise downconverter module with good gain and excellent input return loss. Although it has been designed for use with a spectrometer that implements the IF hybrid digitally, it can work in a 2SB configuration by adding an external low-frequency hybrid. The module was designed with a scalable and compact architecture that allows easy integration into larger systems. This work is focused in the band from 75 to 110 GHz motivated by several astronomical projects, including the Atacama Large Millimeter Array (ALMA), and the possible upgrade of the TianMa Shanghai Radiotelescope to the W band using FPAs. However, multiple areas outside astronomy can benefit from such compactness and feasibility of integration. The module presents noise below 10 dB, input return loss above 12 dB, and gain above 5 dB over most of the design bandwidth. When a low-frequency hybrid is added, a sideband separation ratio above 7 dB can be obtained, although it could be improved up to 40 dB by using a digital IF hybrid [29].

2.2 Module Design and Construction

The module is based on a RF hybrid followed by a high-frequency amplification stage and broadband mixers. Fig. **2.1** presents a schematic of the downconverter. The input stage is a quadrature hybrid implemented in WR10 waveguide with the isolated port terminated in an integrated waveguide load. Each signal is amplified by a commercial LNA and then down-converted using subharmonic mixers. The latter were designed in-house and built in MMIC commercial technology using gallium arsenide (GaAs) Schottky diodes [38]. The I (in-phase) and Q (quadrature) output IF signals have a broadband range up to 15 GHz. The local oscillator (LO) signal required by the mixer is delivered by a Wilkinson divider followed by a lowpass filter that acts as controlled termination for RF signals leaking into the LO path. As demonstrated below, this architecture allows obtaining better input return losses compare to the reflections of LNAs, as long as they are not to different.

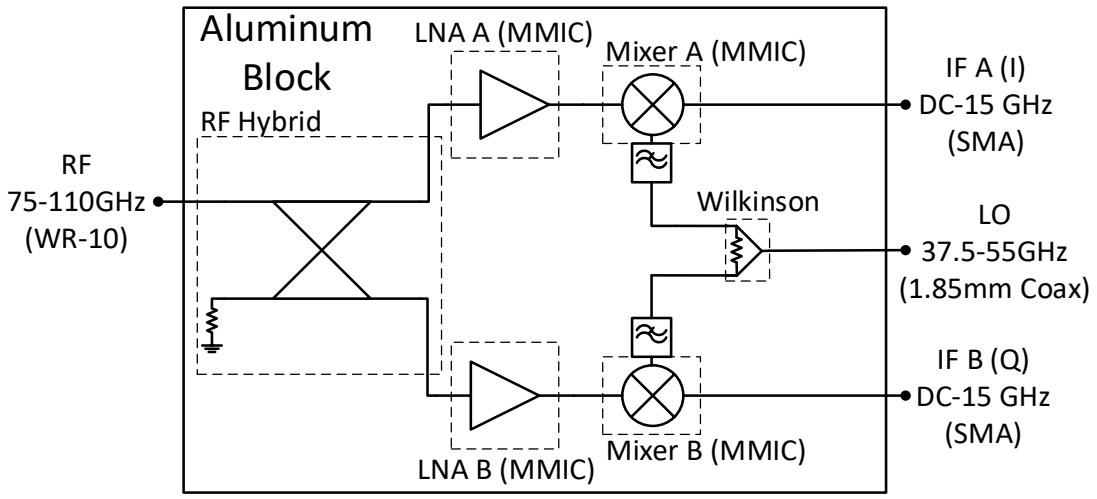

Figure 2.1: Architecture of the broadband downconverter. The input quadrature coupler allows the module to be used as sideband separation mixer. The first amplification stage is a 20 dB MMIC from OMMIC. The second stage is the downconverter itself which is implemented as a subharmonic mixer. The LO is distributed using a Wilkinson coupler followed by a LO filter.

To simplify the analysis, and referring to Fig. 2.2a, it is assumed that the hybrid has no reflections, and that the backward transmissions of the LNAs are low enough so that they become the main source of reflections. Under these assumptions, the amplitude of the reflected wave at the RF port can be written as

$$|V_{RF}^{Reff}|^2 = A^2 + B^2 - 2AB\cos(\Delta_A - \Delta_B), \tag{2.1}$$

where $A = \gamma_A\ V_0\ \rho_A^2$, $B = \gamma_B\ V_0\ \rho_B^2$, $\Delta_A = 2\varphi_A + \theta_A$ and $\Delta_B = 2\varphi_B + \theta_B$. $\gamma_{A,B}$ and $\theta_{A,B}$ are the magnitude and phase of the reflection coefficients of LNAs A or B, $\rho_{A,B}$ and $\varphi_{A,B}$ are the magnitude and phase (relative to an ideal hybrid) of the transmission coefficients of the RF hybrid to LNAs A or B, and V_0 is the amplitude of the input RF signal. Note that quantities A and B represent the amplitudes of the reflected waves from LNAs A and B considering only the transmission of the hybrid.

In a perfectly balanced configuration both LNAs would be identical, implying A=B and $\Delta_A = \Delta_B$, and, therefore, $|V_{RF}^{Reff}|^2 = 0$. In other words, no power is reflected to the input port. The situation when there is no perfect balance is shown in Fig. 2.2b. This figure presents the ratio (in dB) of the reflected wave $|V_R F^{Reff}|^2$ to $|A|^2$ in terms of amplitude and phase imbalances. Thus, the plot represents the improvement of S_{11} of the entire system with respect to the reflection caused by taking into account only the amplifier A. The graph is mirrored about the Y-axis when plotting the improvement with respect to amplifier B. Therefore, for small imbalances, improved S_{11} will be obtained in comparison to both amplifiers, A and B. However, with higher levels of imbalances, S_{11} will improve only compared to one of the amplifiers, either A or B. The module

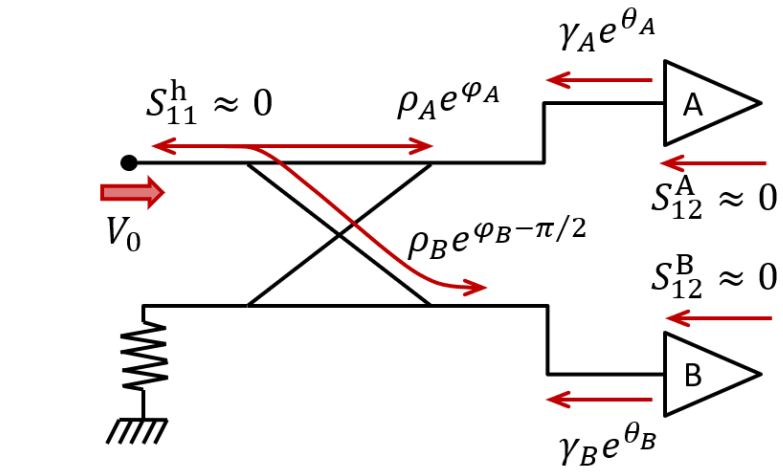

(a)

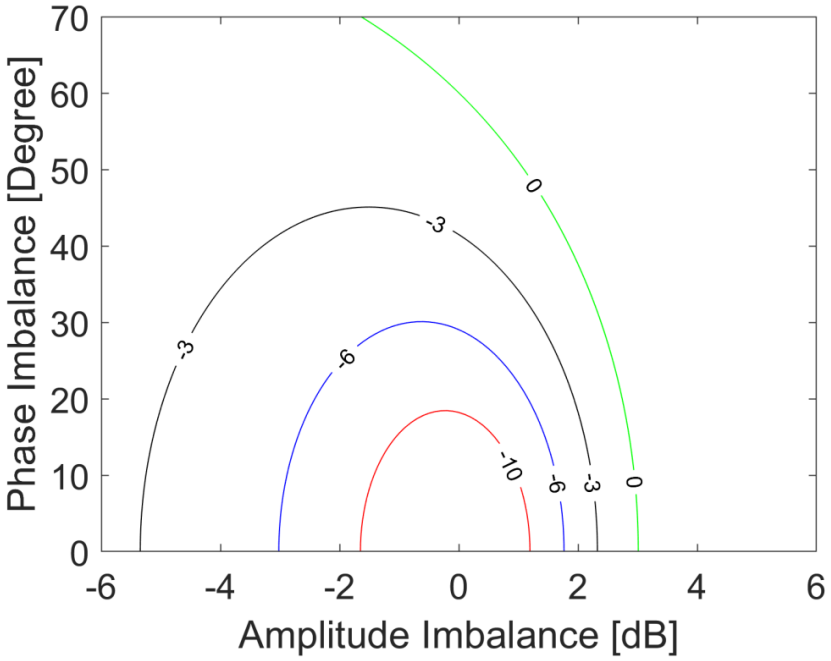

(b)

Figure 2.2: (a) Flow graph for the return loss of the module. Reflections of the hybrid, S_{11}^h, and backwards transmissions of the amplifiers, $S_{12}^{A,B}$, are neglected. Because of the latter, reflections from the rest of the system are of no importance. (b) Improvement, in dB, of the reflected wave $|A|^2$ when adding the 90° RF hybrid at the input for unbalanced systems. From the center, the curves are at -10, -6, -3 and 0 dB.

does not include an IF hybrid as it was designed for use with modern digital spectrometers that implement it digitally [29]. However, an external low frequency hybrid can be added to separate the upper and lower sidebands. The usual mathematical analysis, e.g. see [39], does not include the effect of the LNAs, but their effect can be easily taken into account by adding their gain and phase imbalances. They will add up to the imbalances of the other components of the system.

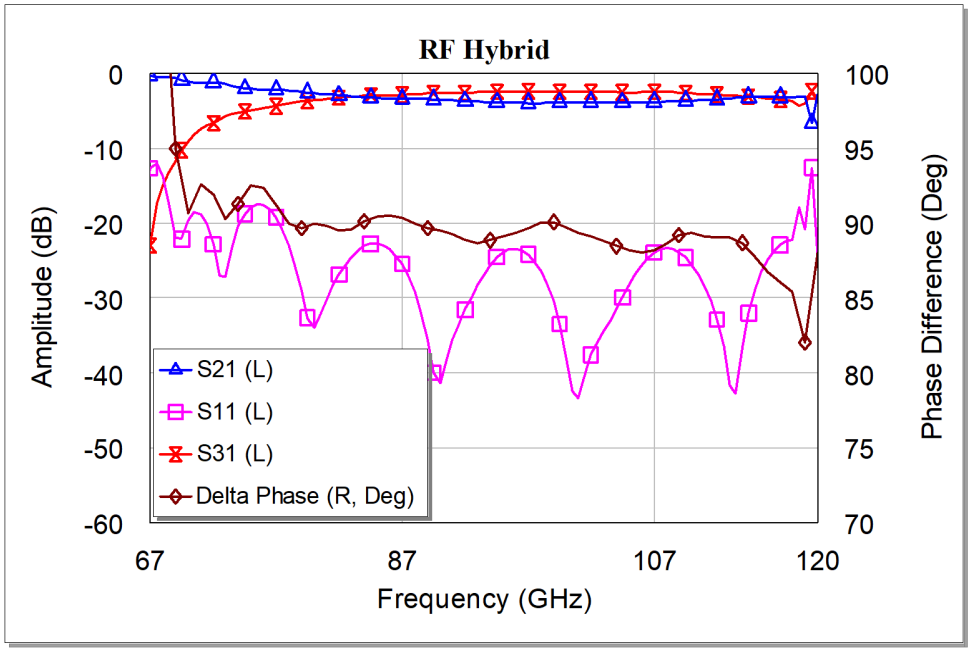

Figure 2.3: Scattering parameters of the multi-branch waveguide 90º hybrid simulated in HFSS.

However, since the gain of the amplifiers can be tuned by changing the bias of the LNAs, so can the sideband separation.

2.2.1 Waveguide coupler and load

The multi-branch waveguide 90º hybrid was designed in ANSYS HFSS with the goal of achieving minimum amplitude and phase imbalance performance over all the extended W band (67-116 GHz). However, restrictions on the minimum width of the branches were imposed in order to match our current capabilities of fabrication. The simulation results are presented in Fig. 2.3. They indicate that the bandwidth performance is limited by the restrictions imposed on the design. Therefore, the upper side of the band was preferred because of its scientific importance in radio astronomy. The load necessary to terminate the hybrid was integrated to the design and implemented using MF-124 from ECCOSORB®.

2.2.2 Low noise amplifiers

The commercial LNA CGY2190 from OMMIC [40] was used to improve the sensitivity of the module. This MMIC is a four-stage amplifier based on a 70-nm metamorphic-high-electron-mobility-transistor (mHEMT). The conduction channel has a high percentage of indium content, achieving a low noise operation and high cut-off frequencies. The power consumption of the chip is about 30 mW, which is not a problem for room temperature operation. The MMIC was packaged in a test block to measure noise and gain at room temperature. A picture of the mounted MMIC on the test block is presented in Fig. 2.4a. Measurements, presented in Fig. 2.4b, show an average gain and noise of 18.5 dB and 626 K, respectively, on the W band. The amplifier covers the band of interest with a roll off at the band edges. The measurement shows higher noise and lower gain than the values provided by the manufacturer [40] but this is expected because of the effects of the packaging.

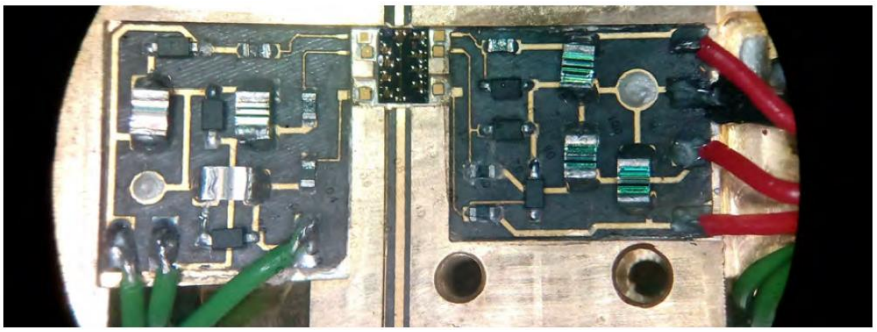

(a)

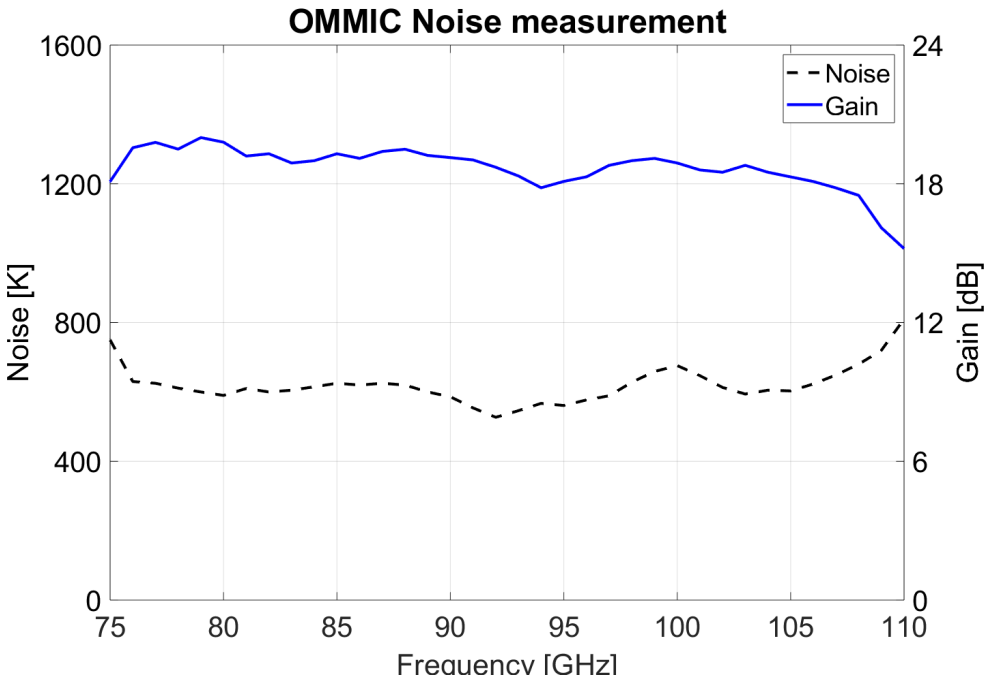

(b)

Figure 2.4: LNA CGY2190 from OMMIC. (a) Picture of the amplifier packaged with a microstrip line as input and output in a test block. (b) Measured gain (solid blue) and noise (dashed black) at room temperature.

2.2.3 Mixers

The central element in a heterodyne receiver is the mixer. Considering the number of mixers needed in a FPA it is very important that the mixers require low LO power. To simplify LO routing and reduce the number of bias lines we decided to use unbiased subharmonic mixers. The mixer chips were designed using the GaAs process from United Monolithic Semiconductor (BES) [38] which has shown a good performance in the W band [41].

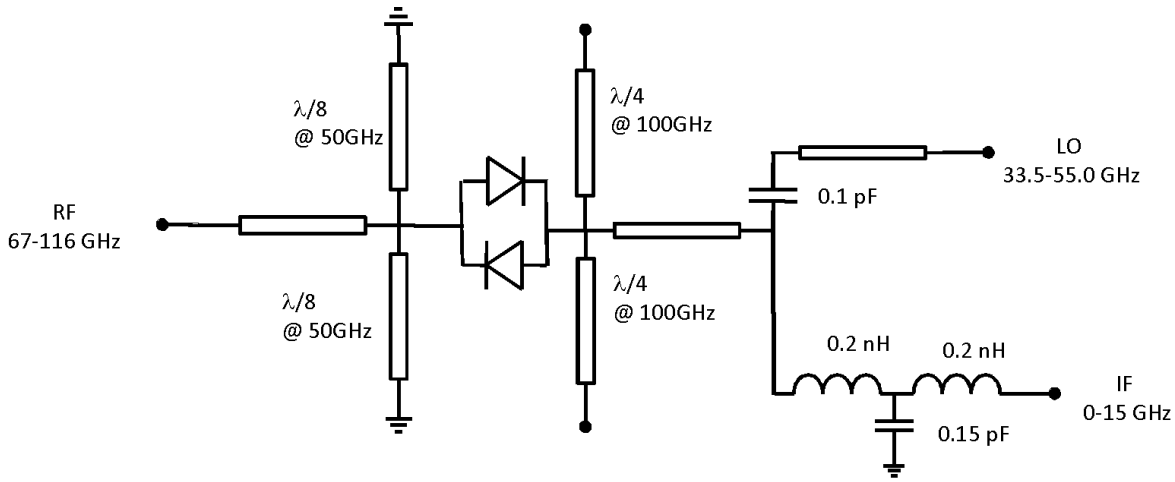

Figure 2.5: Schematic of the subharmonic mixer.

An antiparallel diode configuration connected in series between the RF port and the LO and IF ports [42] was used in the design. Because they use only odd intermodulation products, the LO frequency is half of that of the RF signal. The mixer was designed in AWR Microwave Office [43] to have an ultra-wide band RF frequency between 67 and 116 GHz, a LO frequency between 33.5 and 55 GHz, and an IF frequency between DC and 15 GHz. Fig. 2.5 presents a schematic diagram of the mixer implementation. A $\lambda_{RF}/4$ dual open stub is used to terminate the RF input in a virtual short, but allowing the LO and IF signals to propagate. On the RF side, the IF and LO signals are terminated in a $\lambda_{LO}/8$ short stub. This configuration allows the RF frequency to propagate into the diodes, but not the LO and IF frequencies into the RF port. Ideally the LO termination should be a $\lambda_{LO}/4$ open stub, but to reduce the size of the chip we decided to use a $\lambda_{LO}/8$ short stub, that acts as a high-pass filter at the RF frequency. The LO and RF terminations were placed as close to the diodes as possible. In order to achieve a good isolation between the IF and LO ports, a high-pass filter (series capacitor) was used in the LO input and a low pass filter (L-C-L in tee configuration) was used in the IF output.

The mixer was fabricated at UMS and assembled in a test fixture as seen in Fig. 2.6a. Measurements, presented in Fig. 2.6b, show conversion losses up to 18 dB when operated with a LO power between 4 and 6 dBm. An increase of the conversion loss at 80 GHz that did not appear in the original design was identified. Using simulation tools, we identified this effect as caused by RF power that is not properly terminated at the RF termination. This problem is originated by the RF termination being tuned at 100 GHz and being not optimal at the lower end of the band. The performance of the mixer can be improved by using a different implementation of the RF short in the MMIC. The bandwidth can increase using a double radial stub instead of double linear one [44].

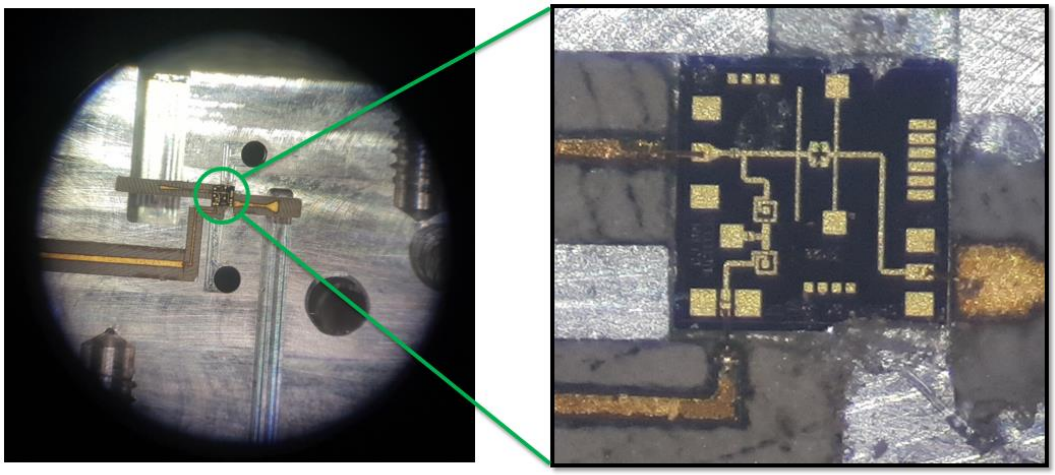

(a)

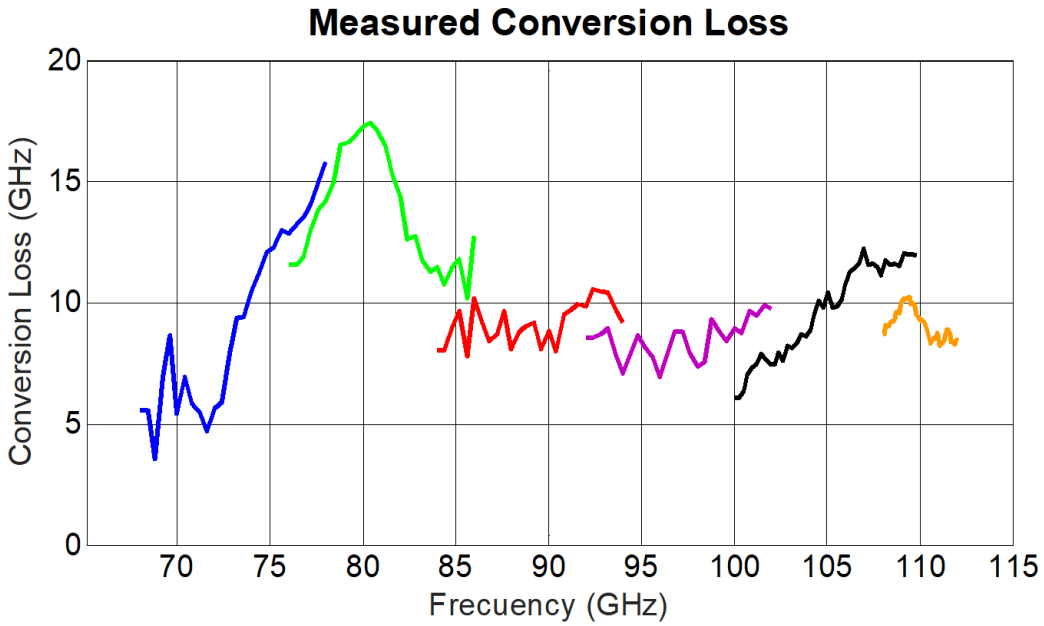

(b)

Figure 2.6: MMIC mixer. (a) Photograph of the MMIC packaged in a test block. (b) Measured conversion losses for a LO frequency of 34, 38, 42, 46, 50, and 54 GHz with an average power of 5 dBm.

2.2.4 Wilkinson power divider and LO filter

A microwave power divider was implemented to split the LO signal to the two mixers. The power divider selected to accomplish this task was a microstrip Wilkinson power divider. This type of divider has good isolation between its output ports, a necessary feature to avoid standing waves between the two mixers caused by the high reflections of the LO port.

The Wilkinson divider was implemented in Rogers© Duroid 6202, with a thickness of 127 um.

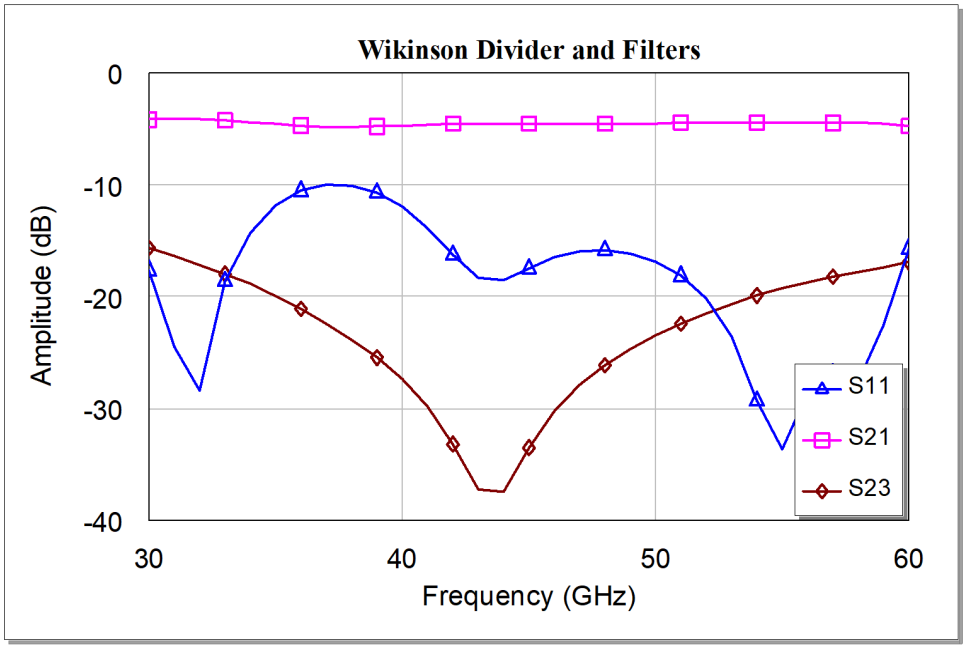

Figure 2.7: Scattering parameters of the Wilkinson divider and filters simulated in HFSS.

A 50 GHz 100 Ω resistor from Vishay Intertechnology in a 0201-package format CH02016 was used to implement the necessary resistor. The input and output ports are matched to 50 Ω. At the output port, low pass radial stub filters were placed in order to control reflections from the leaked RF power to the LO port.

The complete Wilkinson divider, including the filters, was simulated using HFSS. Simulation results, presented in Fig. 2.7, show an isolation of 15 dB and an input return loss better than 10 dB in the complete band. However, the selected resistor decreases its |Z|/R ratio above 50 GHz [45] which, in turn, could cause problems above this frequency. They could manifest in low isolation and matching of the two output ports of the Wilkinson. Since it is known that the LO port of the mixer has a high reflection coefficient, a standing wave can be generated with either the divider (due to the poor match) or the other mixer (due to poor isolation). This standing wave will generate regions in the bandwidth where the LO power needed to drive the mixers is increased.

2.2.5 Simulations of the entire downconverter module

The complete module was simulated using the nonlinear harmonic-balance legacy simulator of AWR Microwave Office. The simulated scattering parameters of several components (particularly the RF hybrid and Wilkinson divider) were imported from HFSS. The amplifier was simulated using the scattering parameters provided by the manufacturer. Since the module requires an external IF coupler to work as a sideband separating mixer, for simulation purposes, an ideal IF hybrid was added to the model. Fig. 2.8 shows the simulated conversion gain of the module in a sideband-separating configuration in both the upper sideband (USB) and lower sideband (LSB). Additionally, Fig. 2.9 shows the return loss for the entire bandwidth and Fig. 2.10 the sideband rejection ratio (SRR).

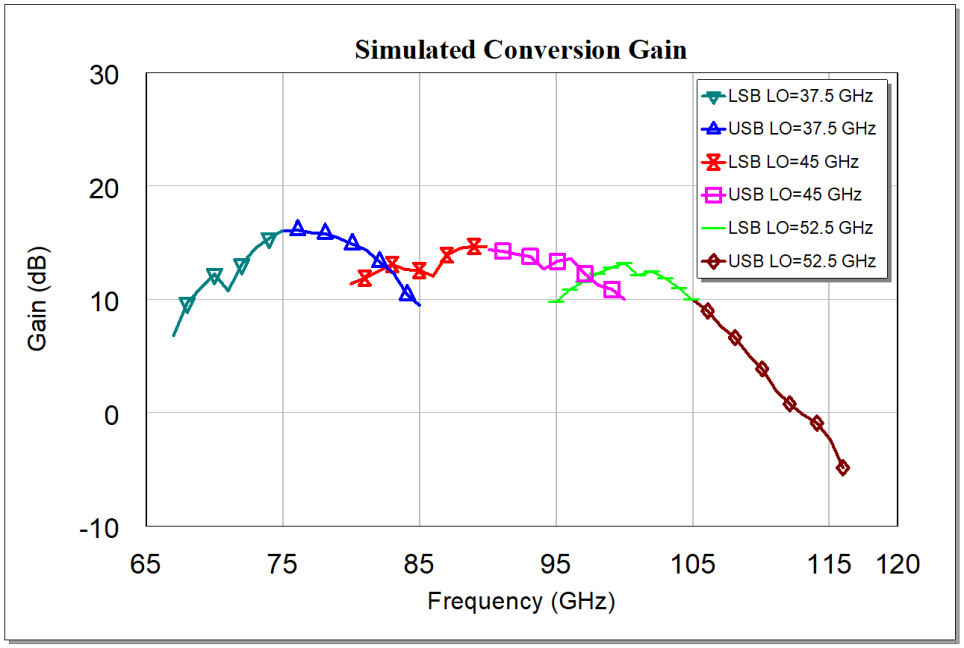

Figure 2.8: Simulated conversion gain of the entire module in AWR with an average LO power of 9 dBm.

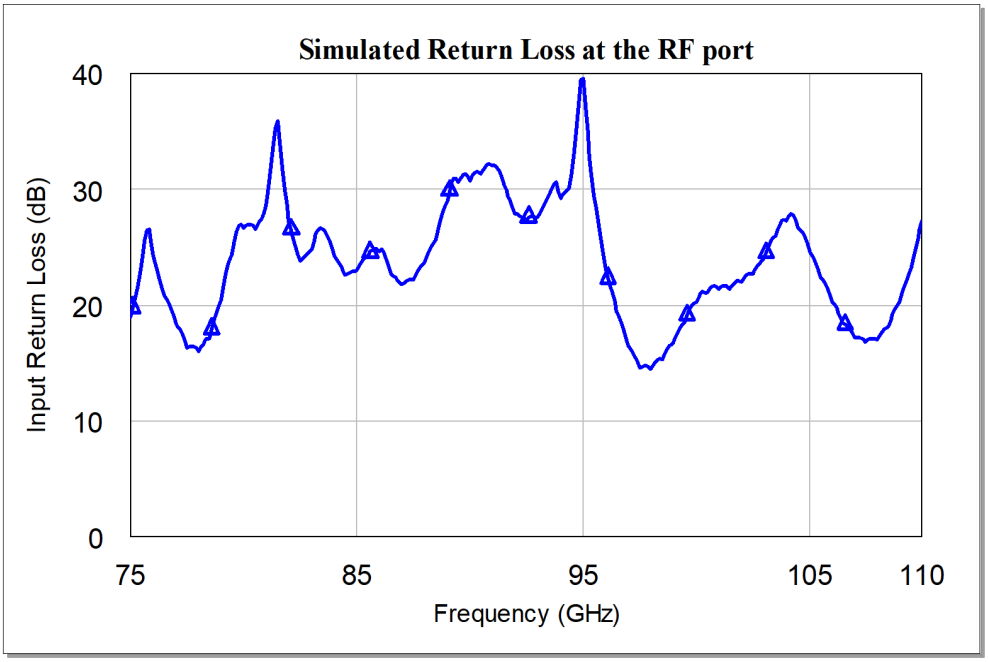

Figure 2.9: Simulated return loss of the module in AWR.

The simulations show very good performance over the entire frequency range, with a decrease in conversion gain at the end of the band. This phenomenon is due to the reduced gain of the LNA at the high end of the band and to the existence of a long-period standing wave between the amplifier and the mixer. The return loss is above 15 dB in the entire band and it is not significantly affected by the LO signal injected into the mixer.

Table 2.1: Estimated average noise and gain of the module..

Component	Gain [dB]	Noise Figure [dB]	Accumulated Noise [dB]
RF Hybrid	−3.0	1.8	1.8
LNA	18.5	4.9	7.5
Mixer	−10.0	10.0	7.7
Module	5.5	7.7	-

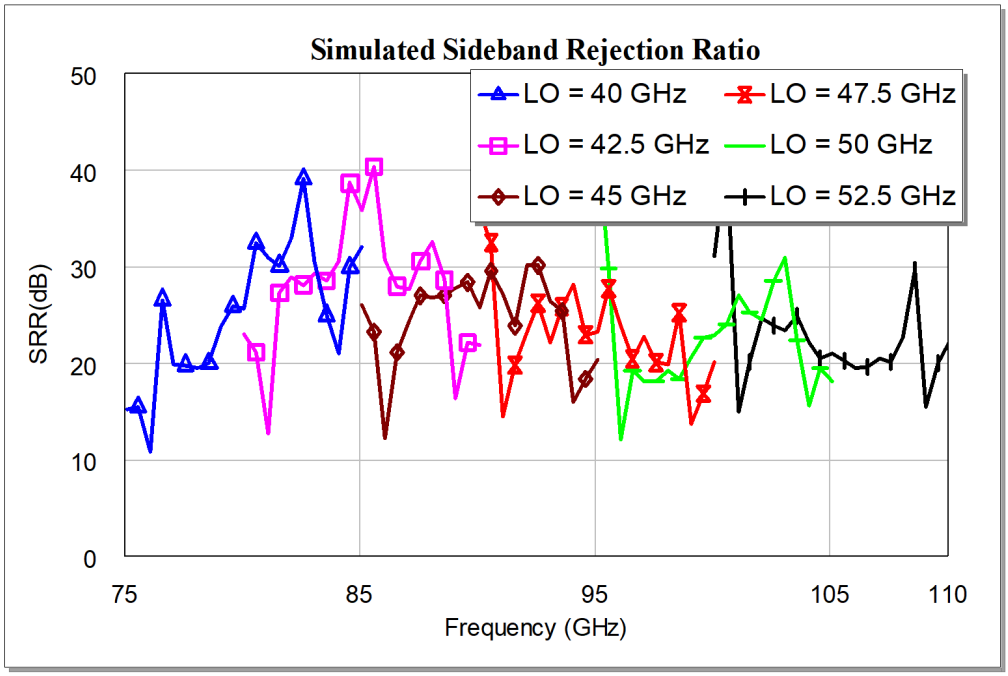

Figure 2.10: Simulated sideband rejection ratio in AWR.

Table I shows an estimated average value, for the W band, of the noise figure for the different stages of the module. The last row of the table shows an estimated value for the noise of the entire module for the I/Q branches. This estimation was made using the Friis formula for noise [6]. This value will decrease significantly if a cryogenic amplifier of high gain is placed before module.

2.2.6 Construction and assembly of the module

The housing, which includes all waveguide structures, was fabricated on Aluminum 6061 using a high-precision CNC milling machine. The tool available for the construction of the slots of the hybrid, which is the most sensitive part of the structure, has a diameter of 0.2 mm and a height of 1.3 mm. The height-to-diameter ratio is extremely high, thus giving an important constraint in the design of the hybrid and its bandwidth.

The size of the final block is 50 mm × 25 mm × 20 mm. Its height is set by the input RF connector, a rectangular waveguide (WR10). The LO is fed using a 1.85 mm connector and the IF signals are transmitted using SMA connectors. For biasing the amplifier, the module uses a 15-pin connector. In the backside of the block, a bias circuit provides over-voltage protection using Zener diodes. This circuit is connected to the interior of the block with DC feedthroughs from Emerson Thunderline Z.

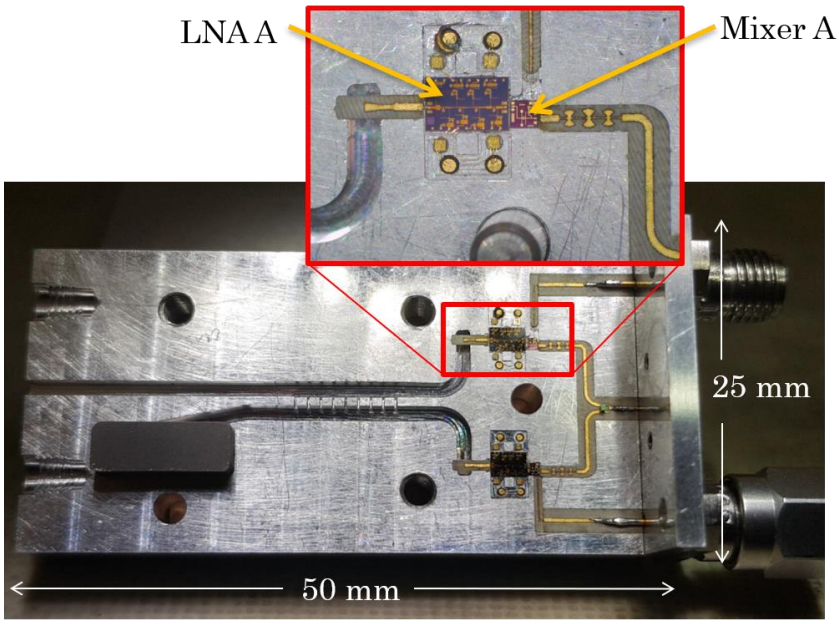

Figure 2.11: Picture of the interior of the assembled module. The inset shows details of the MMICs containing the LNA and mixer, respectively.

Fig. 2.11 shows a photograph of the constructed module. As it can be seen in the picture, the cavity of the LNA is significantly larger than other components in the module. Considering the size of the LNA MMIC, it is possible that waveguide modes could propagate in the frequency of operation. This effect could cause instabilities in the amplifier. Several methods exist to reduce this phenomenon. For this design, the microwave absorber MF-124 from ECCOSORB® was placed in the upper side of the cavity.

2.3 Module Measurements

Several types of measurements were made in order to fully characterize the module.

2.3.1 Conversion gain and sideband rejection

Fig. 2.12 presents the measured conversion gains for the I and Q branches. The decrease in performance around 80 GHz is originated mainly by the performance of the MMIC mixer (see Fig. 2.6b and discussions). Regarding the LO power necessary to drive the entire mixer, if we compare it with the power to drive a single mixer, we would expect an increment of 3 dB (we are now driving two mixers instead of one). However, we detected instead an increase in the LO power of 5.5 dBm up to 100 GHz and 7 dBm at higher frequencies. This increment is due to the 1.85 mm connector used to supply the LO and the performance of the microstrip Wilkinson divider, limited by the use of a chip resistor.

The conversion gains of the USB and LSB were measured using an external IF hybrid (Fig. 2.13). Although the mixers can work with IF frequencies up to 15 GHz, due to the operating frequency range of the IF hybrid, the measurement was done from 0.8 to 4.2 GHz. An increase

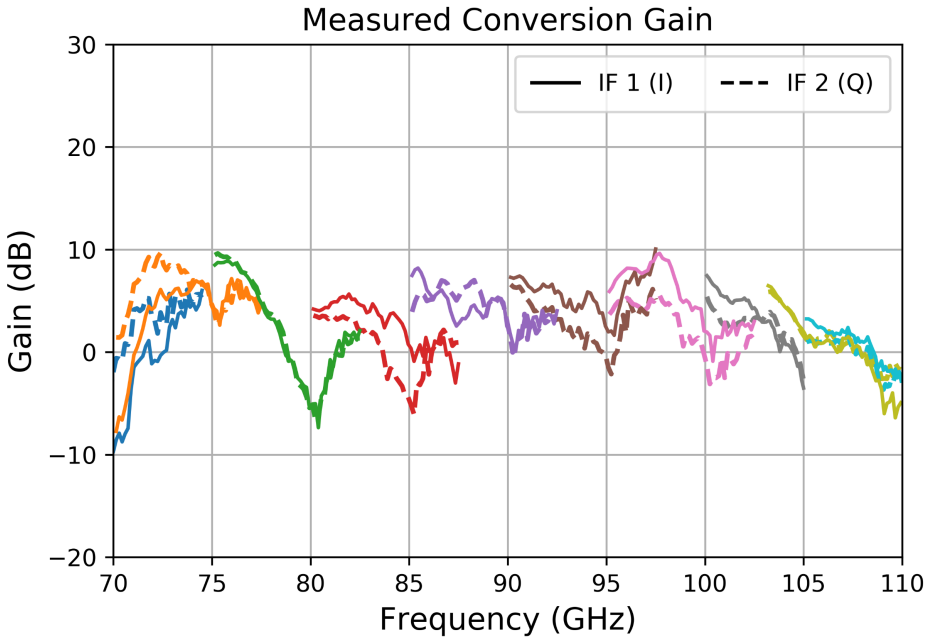

Figure 2.12: Measured conversion gain for the I/Q branches for LO frequencies of 33.5, 35, 37.5, 40, 42.5, 45, 47.5, 50 and 52.5 GHz, with an average LO power of 12 dBm.

in gain is achieved due to the coherent addition of the USB and LSB signals, increasing the performance of the downconverter. This effect can be clearly seen by comparing Fig. 2.12 and 2.13. These results also show the presence of a standing wave in the RF path, as the increase is uneven and some points above 105 GHz have better gain that the expected simulated value (Fig. 2.8). This standing wave could be produced by an interaction between the amplifiers and mixers.

The operating points of the amplifiers were chosen in order to maximize the SRR, effectively cancelling small amplitude imbalances in the system. A SRR above 10 dB was achieved in over 75% of the band, as shown in Fig. 2.14. An illustrative example of this improvement is shown in Fig. 2.15.

The measurements of the SRR show that there are three regions where it decreases. One is below 75 GHz (not shown here), due to mechanical constraints in the RF hybrid. The second region of decrease is between 85 and 88 GHz (see Fig. 2.14). To understand this problem, further analysis was performed using AWR and HFSS. On the one hand, AWR simulations show that a RF resonance between the amplifier and the mixer can cause such behavior. On the other hand, HFSS simulations of the entire cavity where the MMICs are placed show that indeed such resonances appear. Under this circumstance an interaction between the cavity and the MMICs bondwire can cause this phenomenon. Fig. 2.16 shows an AWR simulation of the SRR of the entire module considering the presence of the resonance. The Figure shows a major downgrade in only a narrow part of the band. It is important to emphasize that this phenomenon is produced by the cavity holding the MMICs and not by the proposed architecture. Possible solutions for this problem are to use a different LNA or implement a gap waveguide structure [46]. The last region of degradation of SRR is between 102 and 104 GHz, this decrease can be explained due to the high input return loss of the amplifier. This phenomenon has been also reported in [47]. Fortunately, there are techniques to increase SRR, such as digital sideband separation [29]. This module was built to be

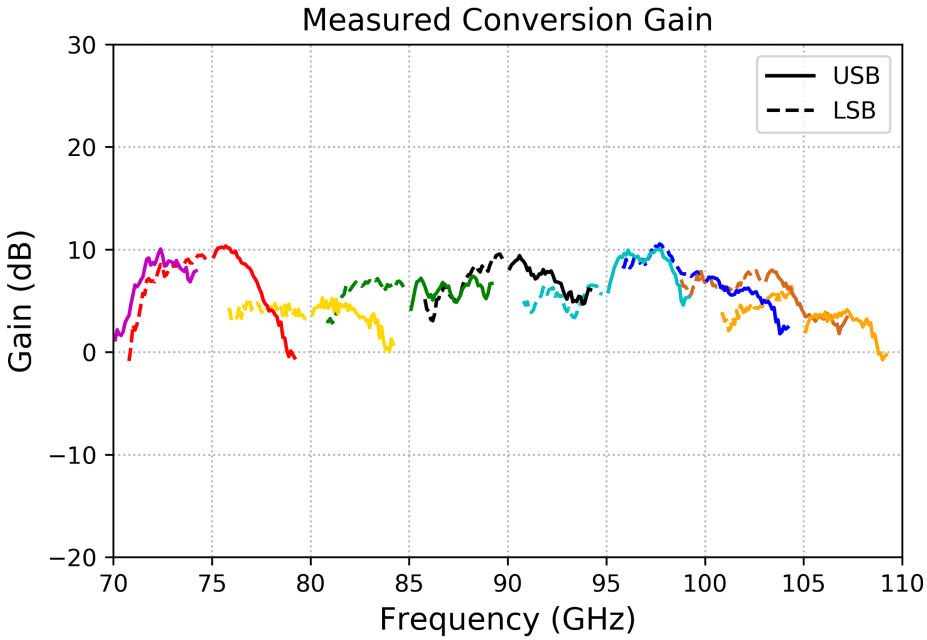

Figure 2.13: Measured conversion gain with sideband separation, for LO frequencies of 35, 37.5, 40, 42.5, 45, 47.5, 50 and 52.5 GHz, with an average power of 12.3 dBm.

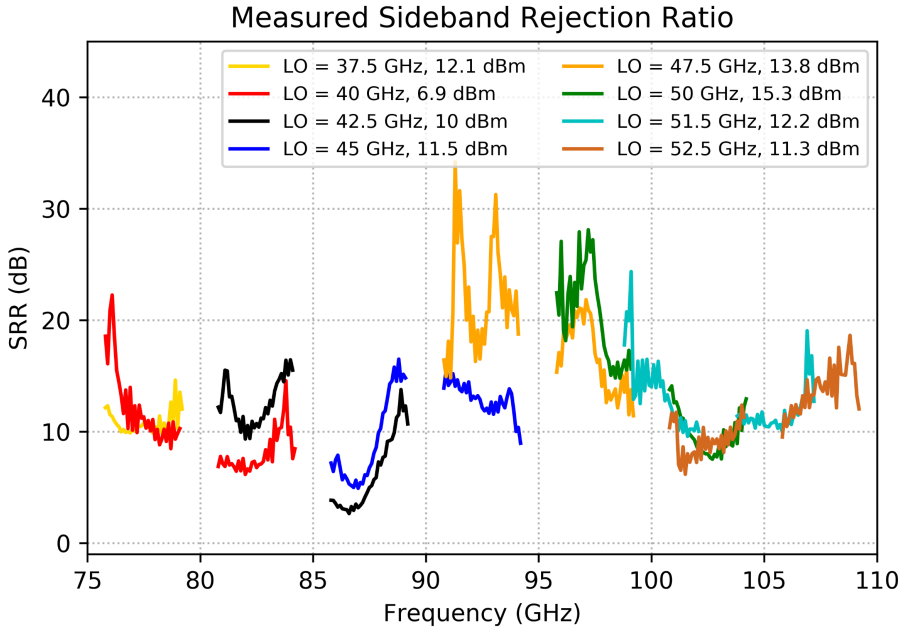

Figure 2.14: Measured SRR with an average power of 12.3 dBm..

fully compatible with that kind of technique.

2.3.2 Return loss

The input return loss of the module was measured using the test setup presented in Fig. 2.17. The results are presented in Fig. 2.18 which shows a return loss above 12 dB in the complete

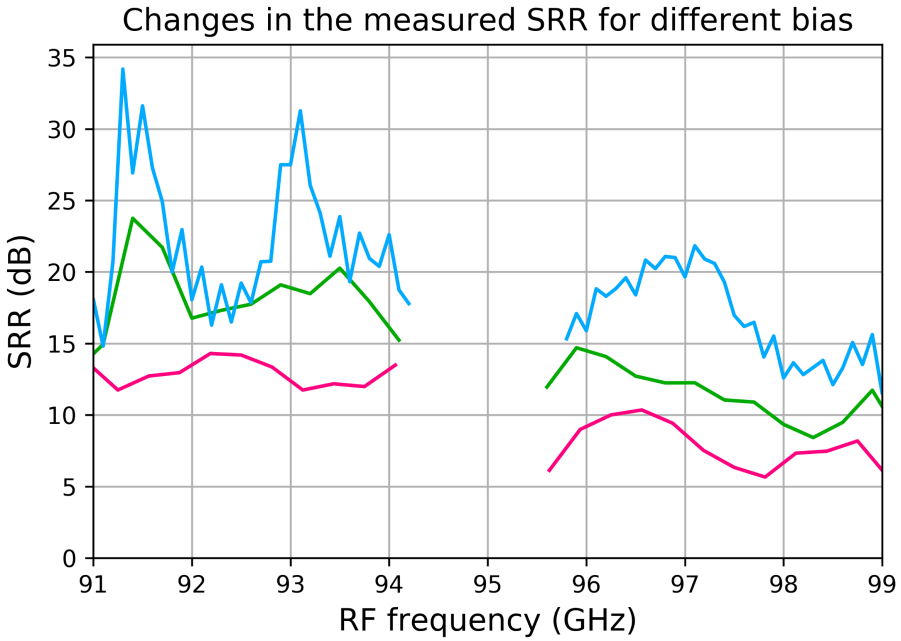

Figure 2.15: Examples of SSR improvement with changes in the bias of the amplifiers, for a LO frequency of 47.5 GHz. Magenta: Significantly different bias settings between the amplifiers (50% of power consumption difference). Green: equal bias settings in the amplifiers. Cyan: Optimized bias setting for both amplifiers (10% of power consumption difference).

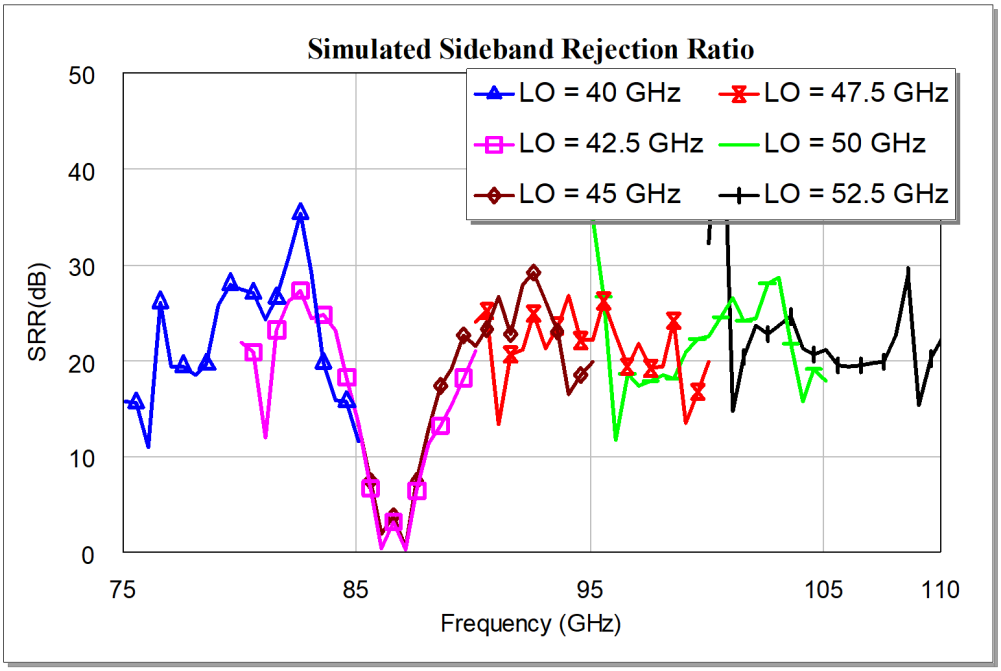

Figure 2.16: AWR simulations of the SRR considering the presence of a 96-GHz resonance between the amplifier and the mixer. The degradation around 87 GHz coincides with the experimental results presented in Fig. 2.14.

band. Similar results were also obtained when using different bias settings for the amplifiers. With the architecture used in this module, the amplifier bias point does not affect the return loss of

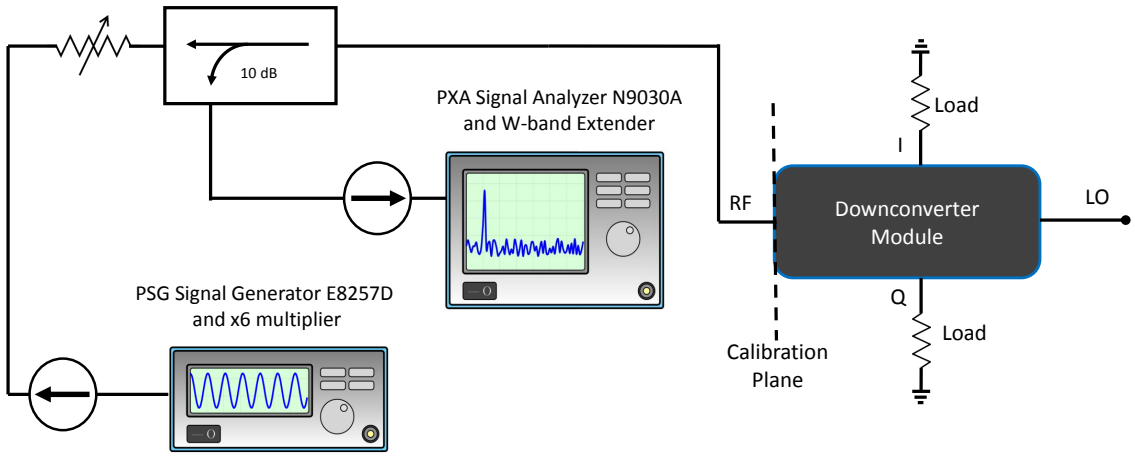

Figure 2.17: Test setup used to measure the return loss at the RF port. A calibration plane was used at the input port to subtract losses introduced by the setup.

the module, even using very different bias. Moreover, it should be noted that, because of the very low S_{12} of the LNAs [40], the LO power and frequency do not have an effect in the input return loss of the module. These properties are extremely important in heterodyne receivers based on a LNA as first element. In these types of systems, an isolator is usually placed between the LNA and the down-converting mixer in order to avoid standing waves that originate from the bad output reflection, characteristic of almost all LNAs, and the bad input reflection of most mixers. If possible, isolators are avoided since they are bulky and have limited bandwidth. The results presented here allow this module to be placed after a LNA without the need of an isolator.

2.3.3 Noise figure

Noise measurements for the I and Q branches were made using the Y factor method. A load at room temperature and one submerged into liquid nitrogen were used as hot and cold loads, respectively. The measurements were made at a room temperature of 297 K with an external IF amplifier (30 dB of gain and noise figure of 3 dB) and a detector with an integrated IF spectrum of 250 MHz. The contribution of the IF amplifier to the total noise figure was calculated to be 0.2 dB and, thus, neglected. The results, presented in Fig. 2.19, show a noise figure below 10 dB from 75 to 107 GHz, i.e., in 91% of the desired band. This noise figure at room temperature is sufficient for the module to work as downconverter for applications as atmospheric sciences or mm-wave imaging systems. If low noise is required it could also be used to provide second-stage amplification.

If extremely low noise is required, as in radio-astronomy applications, the module could be used after a state-of-the-art cryogenic amplifier [48, 49]. Under those circumstances, the high input return losses and the 5 dB gain would allow the use of, e.g., a 30 dB cold-amplification chain with negligible impact on the noise figure of the entire system.

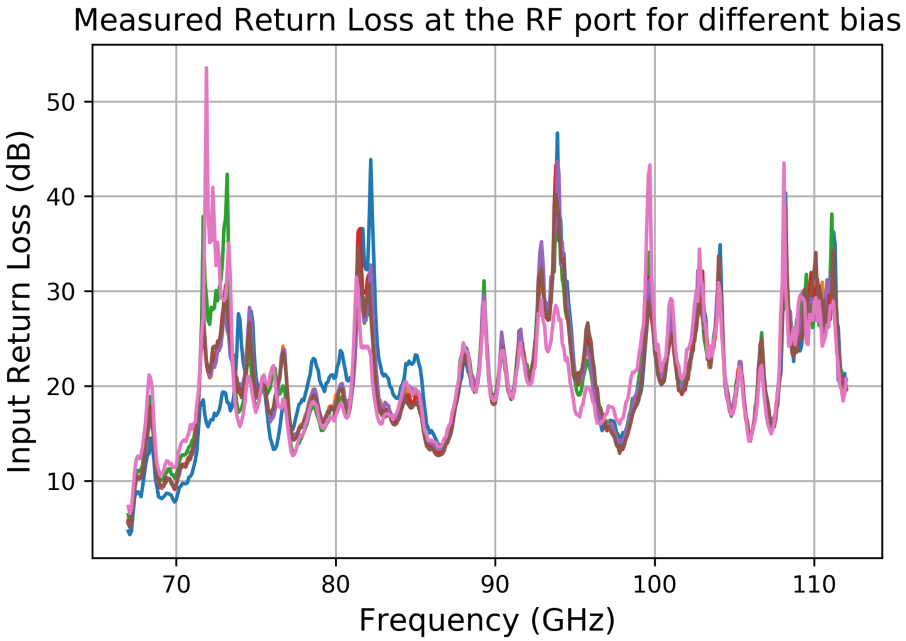

Figure 2.18: Measured input return loss of the module for seven different bias settings for a LO of 40 GHz. Some of the bias settings were significantly different to study its effect in the return loss, one example of this is $V_{\mathrm{d}} = 1.2V$ and $I_{\mathrm{d}} = 12mA$ for amplifier A, and $V_{\mathrm{d}} = 2V$ and $I_{\mathrm{d}} = 20mA$ for amplifier B.

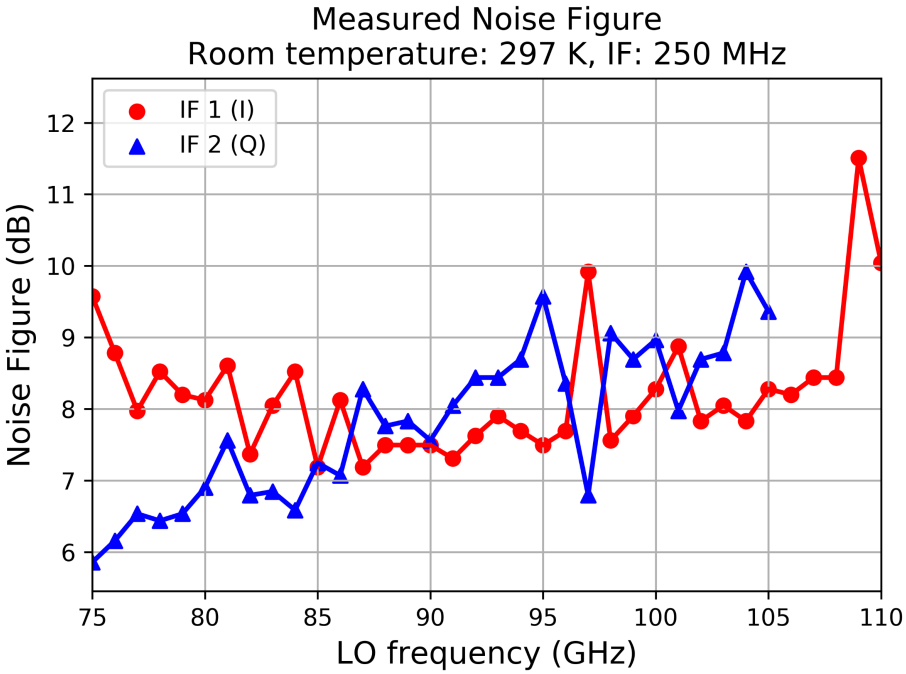

Figure 2.19: Measured noise figure of the module for the I and Q branches. These measurements were made using the Y Factor method with an integrated spectrum of 250 MHz at room temperature.

2.4 Conclusion

A fully functional 2SB downconverter module, working in the W band, has been designed, built and tested. It has a compact architecture that allows obtaining good gain (in average 5 dB) without compromising its return loss (better than 12 dB). This feature allows adding efficiently, if needed, further high-frequency amplification. The module, with its balanced amplification stage, also allows SRR optimization, effectible compensating for any imbalance due to the construction imperfections. The downconverter was built using commercially available technology, reducing the cost of individual receivers for FPA applications.

Although the module was designed for operation with a digital IF hybrid, it has been tested with an external analogue hybrid that allowed achieving image rejection of around 10 dB in the majority of the band with some degradation around 87 GHz. Further simulations have demonstrated that this degradation originates from a resonance present in the large cavity needed to place the amplifier and not because of the selected architecture.

Despite the full functionality of the receiver, several upgrades have been identified for future improvements. The most relevant are optimizing the RF hybrid to increase its operational bandwidth [50], a better Wilkinson divider [51] implemented in MMIC format in order to improve the LO range and power performance, and the use of gap waveguides for attenuating resonances in large cavities [19]. Moreover, even its size could be decreased by approximately 30% in the plane perpendicular to the input with a custom waveguide flange and a micro coaxial connector such as the SMPM connector.

The characteristics of the module presented in this work (compactness, excellent return loss and good gain) make it an excellent choice for integration with multi-pixel receivers. Areas like astronomy, imaging, telecommunications or remote sensing can benefit from this development.

Chapter 3

A Mode-Suppressing Metasurface for Large-Width MMICs Suitable for Tightly-Packaged Millimeter and Submillimeter Heterodyne Receivers

David Monasterio, Nelson Castro, José Pizarro, Francisco Pizarro, and F. Patricio Mena

Abstract: When packaging large-width microwave integrated circuits, care has to be taken to avoid structures that could sustain unwanted oscillations. Unfortunately, this situation may not be attainable since large holding cavities are prone to support parasitic waveguide modes that could produce a feedback loop which, in turn, is especially dangerous in high-gain components with poor match with subsequent elements. This letter presents an scalable metasurface, implemented as a gap-waveguide perfect magnetic conductor, suitable to overcome this problem in millimeter- and submillimeter-band receivers. The proposed solution was integrated into a compact W-band (75–110 GHz) receiver where a large chip-width amplifier was placed near a mixer, thus generating oscillations at high-gain levels compromising its operation at some frequencies. The metasurface was incorporated at the top of the amplifier's cavity where it did not only suppressed completely the oscillation, but also increased isolation between components. As a result, the receiver became fully operational as attested by measurements of its noise temperature at the compromised frequencies.

3.1 Introduction

The size of monolithic microwave integrated circuits (MMICs) is one of its critical aspects, especially when the dimensions of the chip become comparable with its operational wavelength. In fact, a problem arises when packaging such circuits since the cavity containing the chip could support resonating waveguide modes. These resonances could not only generate transmission problems but are especially dangerous when the circuits present gain. Under this circumstance, they

could indeed generate a feedback loop between the output and input of the device, destabilizing a component that could be unconditionally stable otherwise and, at high-gain levels, could provoke an oscillation. This problem becomes more important in the millimeter range and beyond since active MMICs include bias networks that are usually large in size and not easily reducible as the frequency increases [52, 53].

Two solutions have been described to suppress oscillations in packaged MMICs at high frequencies. One is the use of microwave dielectric absorbers to attenuate the resonance [54]. The second approach is the use of a gap-waveguide perfect magnetic conductor (PMC) metasurface. Although PMC structures have been used in other packaging applications at frequencies as high as the D band [55], for oscillation suppression has only been successfully tested in frequencies below 50 GHz [46, 56]. Moreover, these studies were performed on individual amplifiers and not in a functional receiver where interaction with other elements, such as mixers, play an important role.

Recently, we presented a compact W-band heterodyne receiver that uses a commercial low-noise amplifier (LNA) and a custom-made mixer in MMIC form [31]. The LNA, featuring an extensive bias network, has a large chip-width for its operating frequency and its proximity with the mixer resulted in a poor matching producing an oscillation. Although the oscillation was eliminated with the use of a dielectric absorber, it rendered the receiver's performance compromised near to the oscillating frequency due to interactions between the RF input and MMIC cavity. In this letter we demonstrate that a gap-waveguide PMC is a more effective solution since it not only suppresses the oscillation but increases isolation between components.

The excellent performance of the metasurface was further attested by measuring the receiver's noise temperature at the compromised frequencies. Importantly, the design of the metasurface considered mechanical constraints making it scalable to higher frequencies.

3.2 Metasurface Design and Integration into the W-Band Heterodyne Module

The compact heterodyne module presented in [31] uses a commercial MMIC LNA [40] of width $a = 2$ mm. Considering that the cut-off frequency of the fundamental unloaded waveguide mode TE_{10} is given by $\frac{c}{2a}$, where c is the speed of light, we find that in the present case it has a value of 74.95 GHz. Since the MMIC occupies only a small fraction of the cavity, this result implies that waveguide modes could propagate in the W band.

We carried out a simplified electromagnetic analysis of the complete structure that contains the LNA and mixer. The MMICs were replaced with dummy microstrip lines of the same dielectric material forming a continuous line that goes from the input of the LNA to the output of the mixer. The simulation was performed using the full-wave electromagnetic software ANSYS HFSS. Simulation results (Fig. 3.1) shows a deep resonance present at 95.3 GHz. Additional resonance points were also found at the end of the band but with less impact in the overall transmission, $|S_{21}|$.

To suppress the undesired cavity modes, a metasurface working as a PMC was designed [46]. It consists of a bed-of-nails (BoN) periodic structure which generates a stopband depending on its physical dimensions [57, 58, 59]. The insertion of the PMC boundary condition inside the cavity

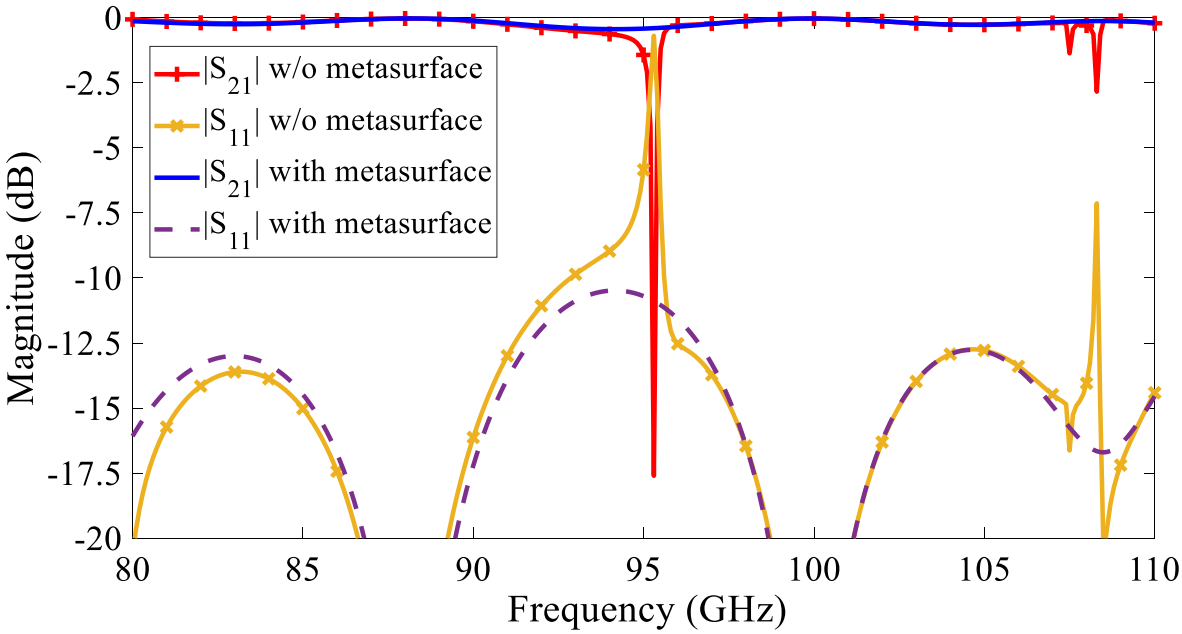

Figure 3.1: Simulated $|S_{21}|$ and $|S_{11}|$ parameters of a transmission line inside the LNA and mixer cavities. Simulations were performed with and without the PMC metasurface.

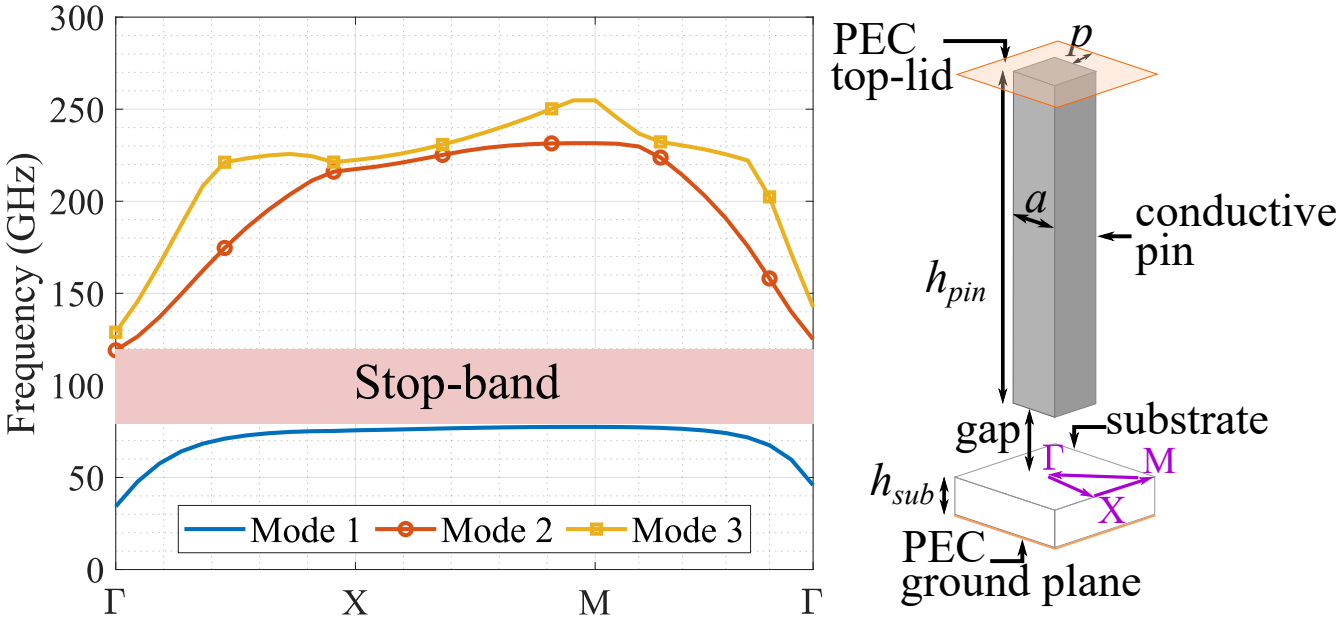

Figure 3.2: Dispersion diagram of the proposed structure. Design parameters of the unit cell are $p = 0.105$ mm, $h_{pin} = 0.9$ mm, $gap = 0.2$ mm and $a = 0.15$ mm.

permits the propagation only where the boundary condition allows it (e.g. between two conductors of the microstrip line) and, by consequence, suppressing all other modes inside the cavity [60, 61].

The designed metasurface must have a stopband within the frequency band we want to suppress the cavity modes. For this, we assess the dispersion diagram obtained on the unit-cell analysis in the irreducible Brillouin zone. Fig. 3.2 shows the proposed unit-cell and the resulting dispersion diagram for the first three modes. The unit-cell consists of a substrate, separated by an air gap

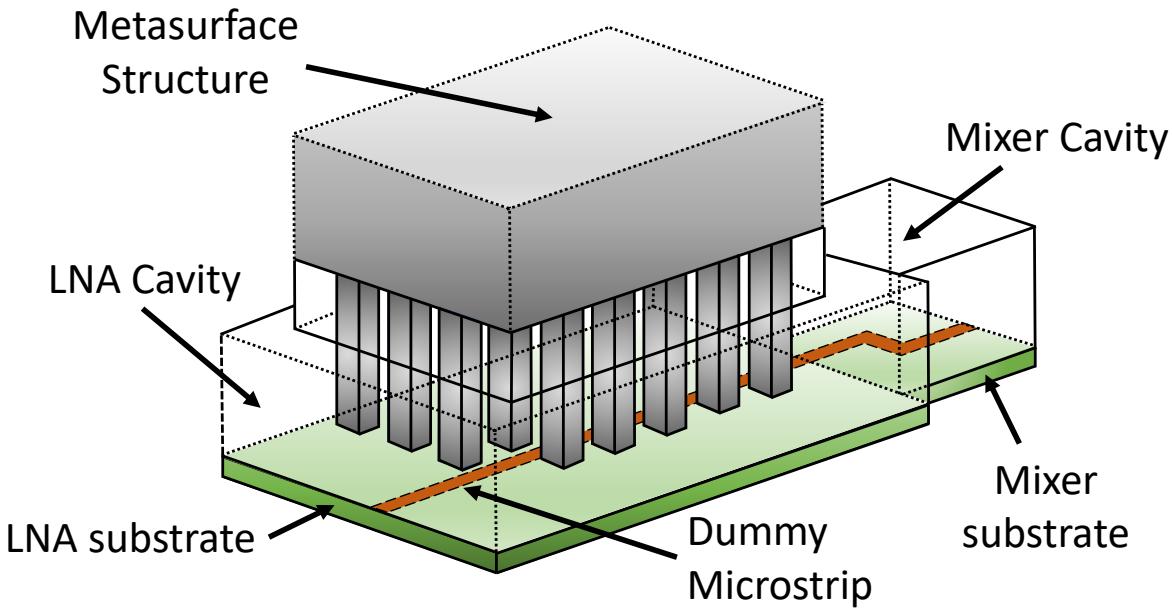

Figure 3.3: Representation of the cavities enclosing the amplifier and mixer. The lid containing the artificial magnetic wall is placed above the amplifier. The microstrip line includes a bend, only within the mixer cavity, to coincide with the input and output of the amplifier and mixer MMICs, respectively.

from the conductive pins, of relative permittivity $\varepsilon_r = 12.9$ and height $h_{sub} = 0.1$ mm. We can see that the stopband generated by the metasurface goes from 77.04 to 113.54 GHz.

This stopband is, moreover, robust against fabrication errors. Considering a variation of $\pm 5\,\mu$m for the lateral dimensions of the pins (i.e. a maximum difference of 10 µm w.r.t. the original dimensions), and increasing the gap to 0.3 mm, the stopband now goes from 77 to 105 GHz, which still suppress the deep resonance present on the structure without the BoN.

Another important aspect of the design was that we set the ratio between the length of the pin and its separation from neighboring pins to be less than 4.5, making its construction feasible with the available machining tools. Using this aspect ratio it is possible to implement the design, with appropriate scaling, at even higher frequencies since it is well below ratios used in the construction of other reported high-frequency structures [62].

To check the performance of the metasurface, we incorporated it into the electromagnetic simulation of the cavity. Fig. 3.1 shows how the resonant peaks of the original simulation were completely suppressed. Finally, the BoN was implemented in a structure that replaced the lid of the existing cavity as illustrated in Fig. 3.3. It was constructed using a Kern high-precision milling machine with a custom milling tool of 0.2 mm in diameter and is presented in the top inset of Fig. 3.4.

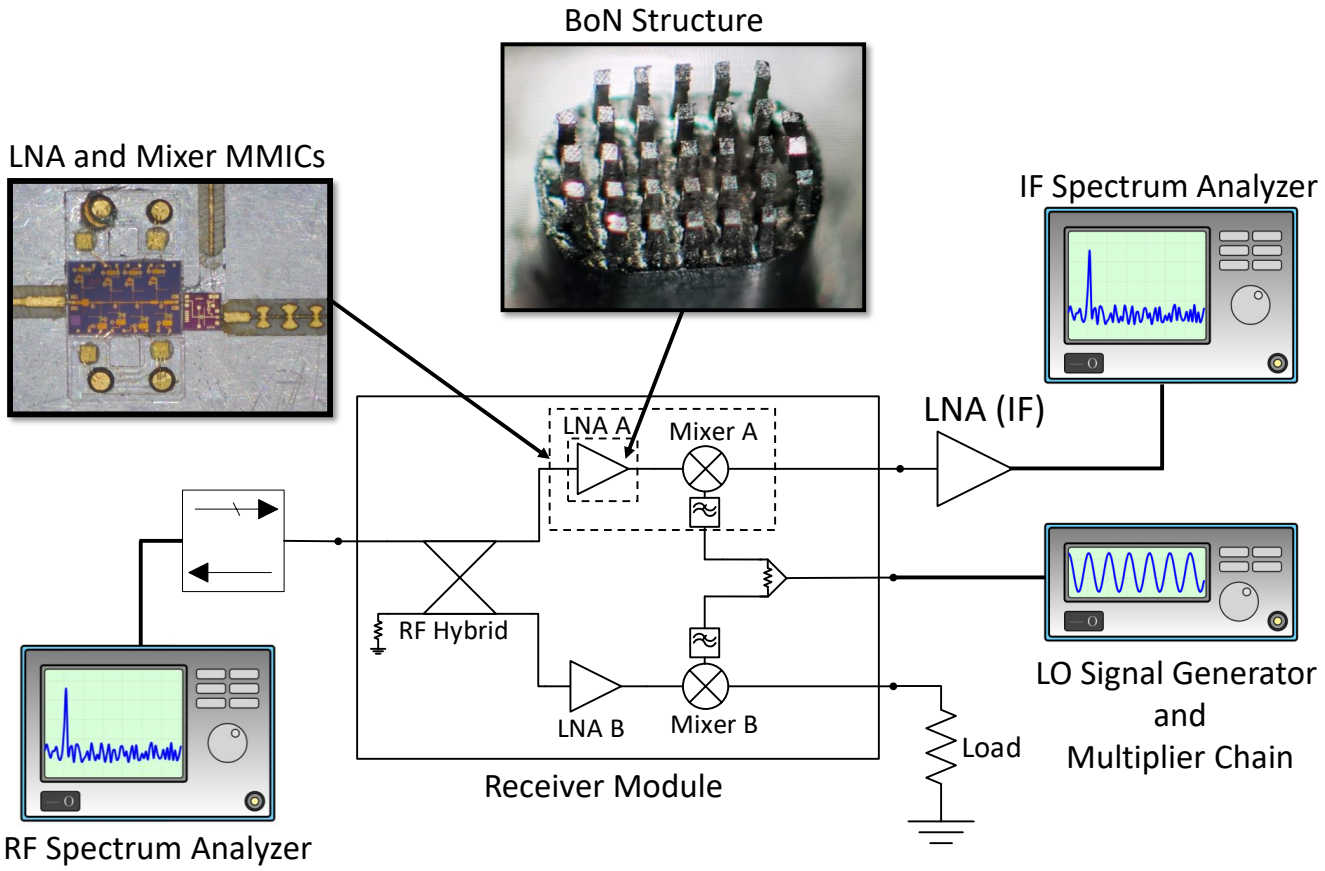

Figure 3.4: Diagram of the setup used to measure the instability of the receiver at the RF and IF ports, simultaneously. Two spectrum analyzers were used, an Agilent PXA Signal Analyzer N9030A with a W-band waveguide harmonic mixer and an Agilent CXA Signal Analyzer N9000A. The insets show the fabricated BoN structure and the LNA and mixer MMICs, respectively.

3.2.1 Power Spectrum Measurements

The measurement setup, shown in Fig. 3.4, allows us to detect any possible oscillation at both ends of the receiver simultaneously. IF amplification was added so that the noise of the spectrum analyzer would not contribute significantly to the measured receiver noise. To simplify the measurements, only one of the two branches of the sideband-separating receiver was tested, working without the use of a 90° IF coupler, thus operating in double-sideband mode. Moreover, they were performed by only biasing the amplifier of the tested branch. Three situations for the LNA cavity were studied, with the original lid, without the lid (open cavity behaving as an ideal absorber), and with the BoN structure. The results are presented using an arbitrary LO frequency of 100 GHz that allows us to analyze the oscillation frequency in both the RF and IF ports. All measurements where made with the same bias and mixer drive settings, unless indicated otherwise.

With original lid

Fig. 3.5a, blue line, shows the oscillation at the RF input using a bias setting of drain voltage $V_\mathrm{d} = 1.4$ V and total drain current $I_\mathrm{d} = 28$ mA for the LNA. , probably caused by an interaction between the cavity and a bondwire that may partially excite a higher mode, has a consistent

frequency of 97.22 GHz. It is ∼2 GHz above the simulation and has a measured power of −36 dBm. In contrast, the resonances that were present in the simulations at the end of the band did not manifest in any apparent oscillations. The RF measurement also shows LO signal leakage of the mixers at 100 GHz. Importantly, the gain setting threshold at which the receiver module becomes unstable depends on the LO drive power. This behavior indicates that the instability is dependant not only on the waveguide cavity but also on the mismatch between the amplifier and the mixer. This phenomenon may also explain the discrepancy between the resonance frequency in the measurements and the simulation, since instead of an almost perfect matching microstrip line, reactive elements such as bond-wire and load impedance are present. Another possible causes for this resonant shift might be the construction and mounting imperfections or the simple natural behaviour of these types of oscillations. The IF output (Fig 3.5b, blue line) presents large harmonic contamination due to saturation produced by the IF amplification of the receiver. Note that, due to saturation of the analog-digital converters of the spectrum analyzer, an internal instrument attenuation was added to properly detect the spectra.

With open cavity

When the lid was removed, the oscillation was eliminated in both the RF and IF spectra (Fig. 3.5a and b, orange lines) due to radiation escaping from the cavity. However, LO leakage to the RF port was suppressed by only 3 dB. We also tested higher LNA bias settings presenting a similar behaviour. It is important to notice that the complete suppression of the instability is not guaranteed for higher gains if a non-ideal absorber is used [46].

Metasurface

Measurements using the BoN structure (Fig. 3.5, red lines) show a complete suppression of the oscillation. Contrary to the situation with the open cavity, the LO leakage power at the RF input is significantly lower and shadowed by the noise floor. This phenomenon can be explained in the following way. Without the metasurface the LO power transfers though the cavity to the RF input, as modes are not suppressed in all directions, ignoring the reverse isolation (S_{12}) of the amplifier, which is usually very high (35 dB). To prove this hypothesis we repeated the experiment with better dynamic range for the instrument and at different bias points. Fig. 3.5c shows two different bias settings, the first is an unbiased state ($V_\mathrm{d} = 0$ V and $I_\mathrm{d} = 0$ mA), and the second is the bias setting used for the previous measurements. The result shows that LO leakage decreases as the bias increases. This phenomenon corresponds to the expected behavior for the reverse isolation of a HEMT amplifier [63] and was validated using a SPICE simulation of a generic HEMT-based LNA. When we repeated the same experiments using the module with the open cavity, the LO leakage was similar in the biased and unbiased states of the LNA. The measured isolation with metasurface is more that 10 dB higher than the case when is not used. This result demonstrates that the metasurface has better performance than the open lid, as waveguide modes are suppressed in all directions.

3.2.2 Noise Temperature Measurements

Additionally, we measured the receiver's noise temperature in the vicinity of the oscillation frequency using the Y-factor method. The measurement was made using the same configuration of Fig. 3.4, but with a horn antenna connected at the RF port instead of the spectrum analyzer

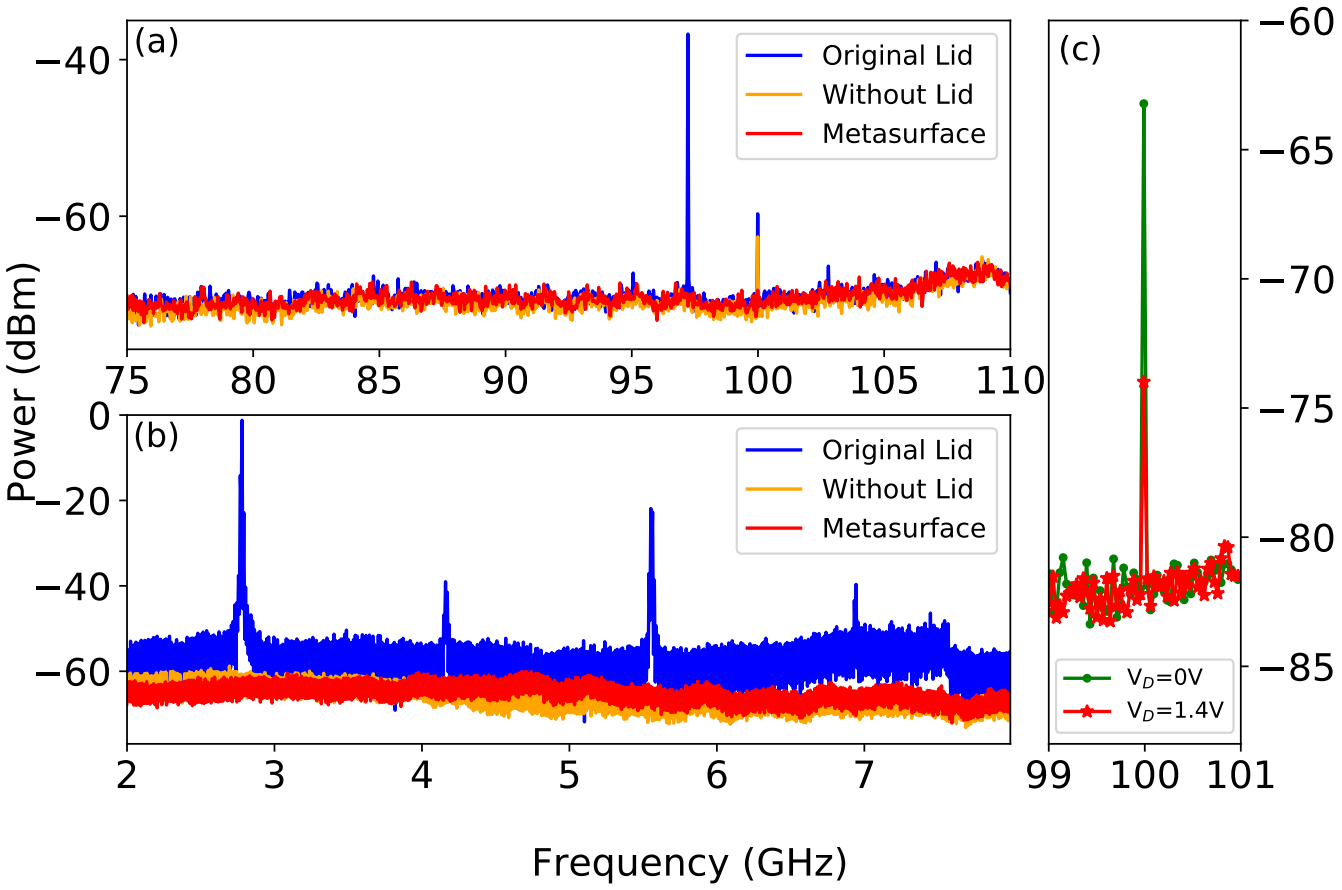

Figure 3.5: Power spectrum measurements. (a) RF port of the module. (b) IF port of the module. (c) LO Leakage measurement at the RF input using the metasurface and with two LNA bias settings.

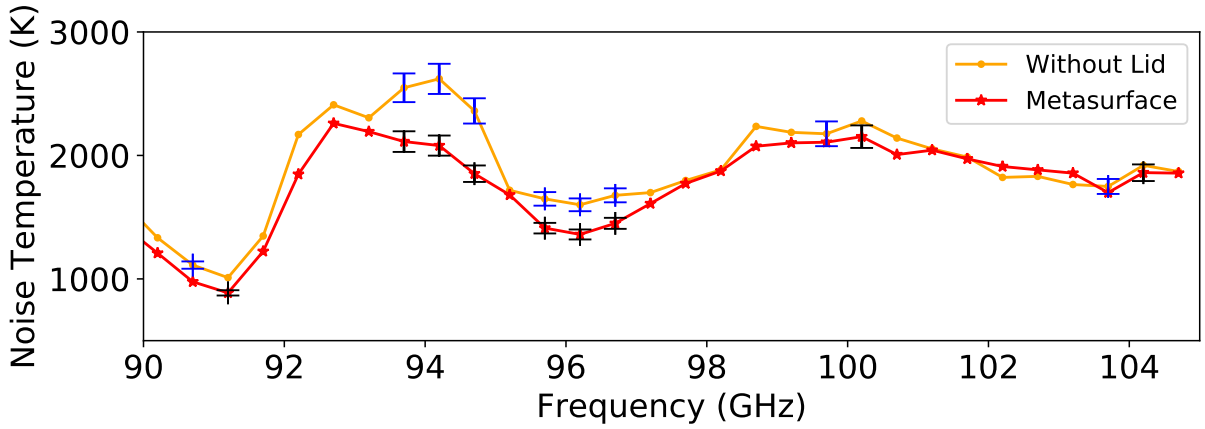

Figure 3.6: Measured noise temperature with the top lid removed and the BoN structure. These measurements were made with a fixed IF frequency of 200 MHz and an integrated spectrum of 100 MHz. Error bars at 1σ are shown in relevant points [64].

and isolator. The receiver with the original cavity was not tested since the saturation of the IF chain did not allow performing measurements under the same conditions which would produce non-comparable results.

Fig. 3.6 shows the measured noise temperature using the metasurface and open cavity. Two aspects are apparent from using the metasurface, absence of oscillations and a slight improvement of the noise temperature from 93.5 to 97.5 GHz. The latter is a consequence of a drop in gain at those frequencies when the cavity is open resulting from, either, a radiating bond-wire or LO leakage affecting the mixer drive point. In any case, both situations are overcome by the metasurface.

3.3 Conclusion

We have demonstrated the use of a perfect-magnetic-conductor metasurface, implemented as a BoN structure, to suppresses cavity modes in millimeter-band receivers. The structure was successfully tested in a W-band receiver, not only suppressing a well-defined oscillation but also preventing the leakage of undesired tones through the waveguide cavity. Importantly, the latter advantage is not provided by having the top lid removed (case similar to an ideal microwave absorber), making the metasurface more robust to feedback loops with high gain or when high isolation between components is required. Its excellent properties were also confirmed with noise measurements. They show that the receiver has good performance in the vicinity of the originally compromised frequency. Finally, the design of the metasurface also considered mechanical constraints for the conductive pins making it scalable for use in the submillimeter range, and proved to be robust in terms of fabrication tolerances.

Chapter 4

A 90° Waveguide Hybrid for Ultra-Broadband Operation with Low Amplitude & Phase Imbalances

David Monasterio and F. Patricio Mena

Abstract: In this work we present a novel waveguide quadrature hybrid with excellent amplitude and phase imbalances over a fractional bandwidth above 50%. The proposed hybrid is a variation of the standard waveguide branch-line coupler with modified dimensions of its branch lines. This modification results in a smaller height-to-width ratio of the branch, effectively easing its construction when compared to a standard hybrid for the same bandwidth. This concept was implemented in an extended W band (67–116 GHz), utilizing a standard WR-10 waveguide at its interfaces. Simulations and measurements show excellent performance in the entire bandwidth, with measured amplitude and phase imbalances below 0.8 dB, and between $-0.5°$ and $+2°$, respectively. Moreover, the operational bandwidth is only limited by the cutoff frequencies of the interfacing waveguides.

4.1 Introduction

The need of quadrature hybrids with more fractional bandwidth and better overall performance has increased over the last few years, especially in the context of radio astronomy where achieving receivers with larger operational bandwidths and more sensitivity has become one of the main objectives for future development [5]. In fact, quadrature hybrids have a very wide range of applications in radio astronomical receivers [65]. Two examples are sideband separating mixers [66, 67, 68, 69, 70, 71, 72, 31] and waveguide frequency diplexers [20]. Importantly, the performance of the hybrid affects severely the sideband rejection ratio of the former and the insertion and return losses of the later.

As frequency increases into the millimeter and sub-millimeter range, waveguides usually become the preferred type of transmission line since they present low losses. It is for this reason that

quadrature hybrids implemented in waveguide are preferred over other options like microstrip and coplanar-waveguides. The most used design is the standard branch-line waveguide quadrature hybrid that can easily be manufactured using standard milling machines [73]. In recent years, efforts have been made to study variations of its topology to achieve improvement of some of its figures of merit [74, 75, 50]. However, increasing its operational bandwidth is difficult since it is necessary to add more branch lines and reduce their widths, resulting in a more difficult construction. Indeed, under these conditions, the ratio between height and diameter of the tool needed for machining the branch lines will increase.

Here we present a modified branch-line waveguide quadrature hybrid that besides achieving an excellent performance over a large fractional bandwidth, exceeding 50%, eases construction constraints. This breakthrough has been accomplished by implementing the branch lines with a larger height than the main lines, which results in wider branch lines, reducing the height-to-diameter ratio of the tool needed to milling them. We have applied this new concept to the extended W band (67–116 GHz), since it is of increasing scientific interest [76], and several telescopes, such as the Atacama Large Millimeter Array (ALMA), are upgrading their receivers to cover it [66]. Simulations and measurements show state-of-the-art performance.

4.2 Justification of the Design

A branch-line waveguide hybrid can be modeled using the even-odd mode analysis in the ABCD-matrix formalism [73]. Let the subscripts B and m describe the branch lines and the line connecting them, respectively. Then, in their more general form, the normalized matrices for the even and odd mode of the branches and the connecting lines are, in turn,

$$\begin{pmatrix} 1 & j\frac{Z_B}{Z_m}T_B \\ 0 & 1 \end{pmatrix}, \begin{pmatrix} 1 & j\frac{Z_B}{Z_m}\frac{1}{T_B} \\ 0 & 1 \end{pmatrix}, \text{ and } \begin{pmatrix} C_m & jS_m \\ jS_m & C_m \end{pmatrix}.$$

In these expressions $T_B = \tan\frac{\theta_B}{2}$, $S_m = \sin\theta_m$, $C_m = \cos\theta_m$, and $\theta = \frac{2\pi l}{\lambda}$. Moreover, Z, l, and λ are the impedance, length and guided wavelength, respectively. To complete the model, an appropriate expression for the impedance is needed. Such a expression can be defined using the power-to-voltage relation [77] which, for the fundamental mode, is given by

$$Z_0 \equiv \frac{|v_0|^2}{p_0^*}\Big|_{\mathrm{TE}_{10}} = 4\frac{b}{a}\frac{\eta}{\sqrt{1-\left(\frac{c}{2af}\right)^2}}, \tag{4.1}$$

where v_0 is the voltage obtained by integrating the electric field in the middle of the guide, p_0 is the integral of the Poynting vector, a and b are the waveguide dimensions, c is the speed of light, f is the frequency, and η is the characteristic impedance of free space. This quantity is a scaled version of the wave impedance and has a closer relationship with the classic definition of characteristic impedance.

We have used this formalism to compare four types of branch-line hybrids in the extended W band. (*i*) The traditional hybrid with connecting lines using an aspect ratio $a_m/b_m = 2$. (*ii*) A traditional hybrid but with a larger value of a_m and high aspect ratio, creating an overmoded

Table 4.1: Parameters used to model the four types of hybrids.[†]

Parameter	**Type *i***	**Type *ii***	**Type *iii***	**Type *iv***
a_m (mm)	2.54	3.5	2.54	2.54
a_m/b_m	2	3.2	2	2
a_B (mm)	2.54	3.5	3.8	3.8
a_B/b_B[‡]	15	24	12.7	12.7
l_B/λ_B	0.25	0.25	0.25	0.16

[†]All models with $Z_B/Zm = 7.5$ and $l_m/\lambda_m = 0.25$.
[‡]b_B was calculated from the value of Z_B/Zm.

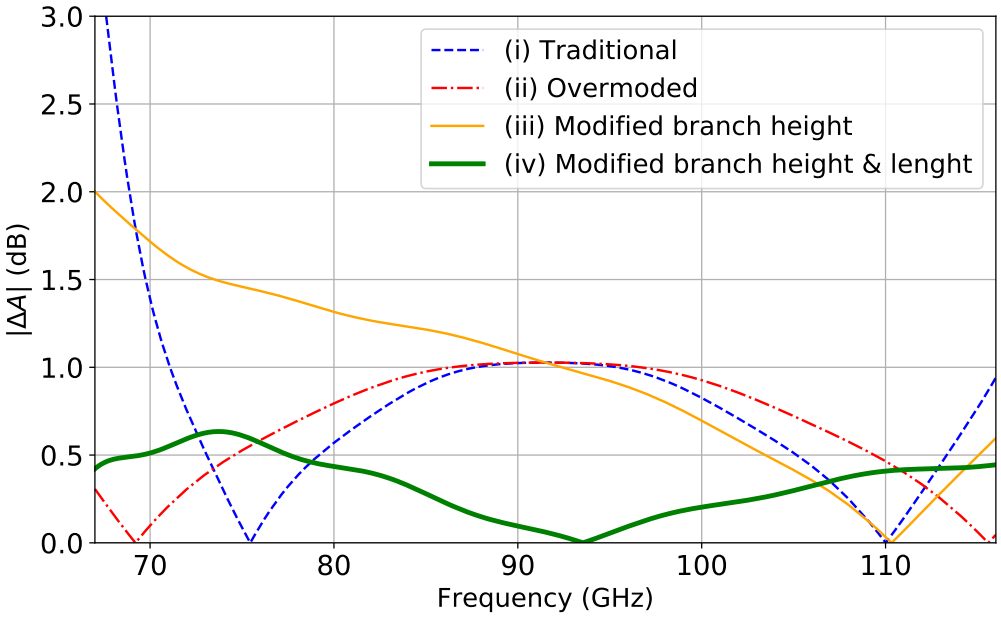

Figure 4.1: Calculated amplitude imbalance of four different types of hybrids with 10 identical branches.

waveguide for the connecting lines [62]. (*iii*) A hybrid with the branches having an increased height. (*iv*) As the previous case but with the branch length shorter than $\lambda_B/4$ at the central frequency. The parameters used in the model are given in Table 4.1 and the results summarized in Fig. 4.1. It is clear that type iv has an important advantage. It does not only cover the entire frequency band with an excellent amplitude imbalance, ΔA, but it also has a lower ratio a_B/b_B which results in an easier fabrication. Indeed, the mill needed to machine the branches would be more robust.

4.3 Proposed Design and Simulations

The modified waveguide branch-line coupler proposed in this work is presented in Fig. 4.2a. To compensate for the effect of fringing fields and other discontinuity phenomena at the junction of the branch with the connecting lines, matching sections were added at the end of the branches. Initially, the design considered a different height for the matching sections but, after optimization and to

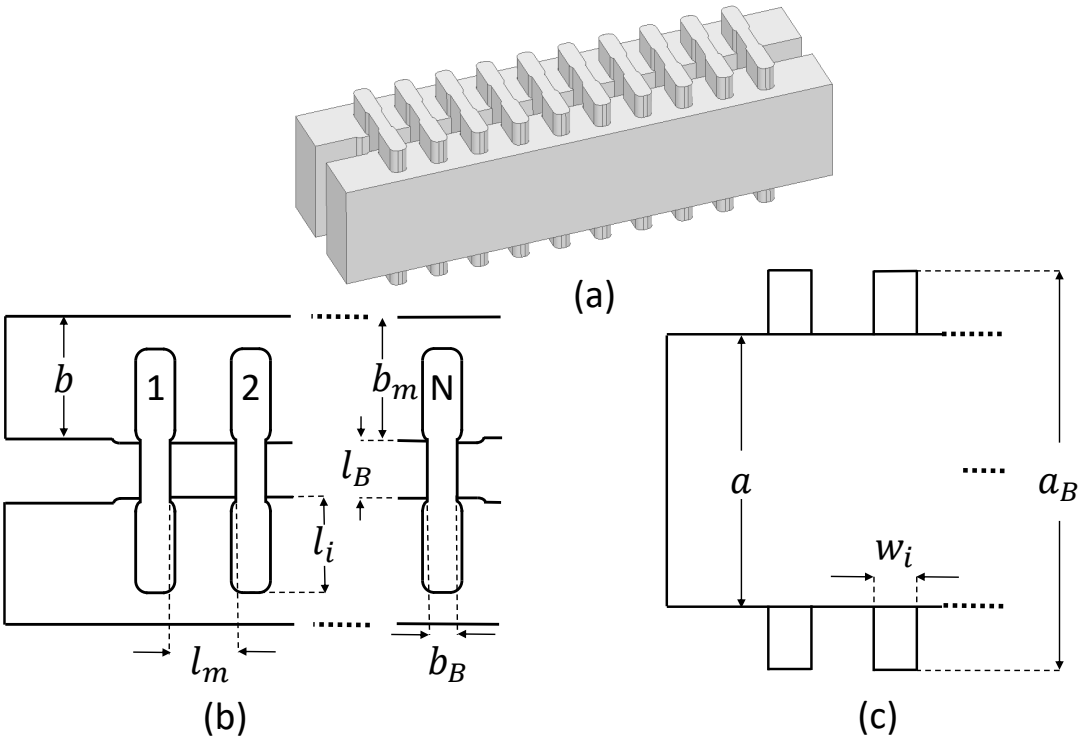

Figure 4.2: Drawing of the proposed hybrid design indicating critical dimensions. (a) Complete CAD model. (b) E-plane view. (b) H-plane view.

Table 4.2: Geometric parameters of the proposed hybrid.

Par.	**Value (mm)**	**Par.**	**Value (mm)**	**Par.**	**Value (mm)**
a	2.54	l_m	0.70	l_B	0.56
b	1.27	a_B	3.74	w_i	0.40
b_m	1.33	b_B	0.30	l_i	0.60

ease the manufacturing process, the same height of the branch slots was selected. Moreover, to increase compatibility with other devices, a standard WR-10 waveguide was selected for interfacing.

The critical dimensions of the design are presented in Figs. 4.2b and 4.2c, and Table 4.2. All the corners were filleted with a radius of 0.15 mm. One of the main characteristics of this design, as discussed in section 4.2, is that the milling tool needed to manufacture the branches has a low height-to-diameter ratio. For this particular design, a tool with a ratio > 6.23 is needed, which is well below overmoded hybrids with similar bandwidth [62].

The proposed hybrid was simulated in ANSYS HFSS. Simulations show that return loss and isolation are over 20 dB (Fig. 4.4 as S-parameters), amplitude imbalance is below 0.5 dB, and phase imbalance, $\Delta\phi$, is within $\pm 1^\circ$ (Fig. 4.5).

In this design, the increased height of the branches and matching sections could produce excitation of high-order modes, leading to resonances. During optimization this fact was considered and the presented solution does not excite high-order modes in any substantial form, as evident in the simulation results. To further validate this result, a sweep with a narrow step (10 MHz) was

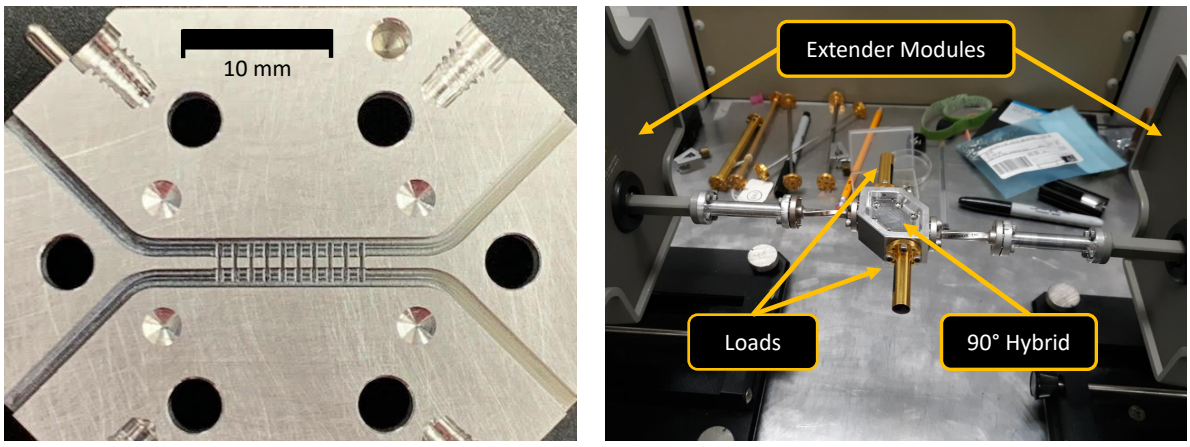

Figure 4.3: (a) Open mechanized E-plane split-block quadrature hybrid. (b) Measurement setup.

conducted, only revealing some mild discontinuities barely discernible in the plots.

4.4 Implementation, Measurements and Discussion

The hybrid was manufactured using the split-block technique in an aluminum block, as shown in Fig 4.3a. Measurements were made using a 2-port Hewlett Packard 8510C Vector Network Analyzer with W85104A W-band extender modules (Fig. 4.3b) and the two remaining ports terminated in matching loads. As the hybrid is completely symmetrical and reciprocal, an arbitrary port was selected as input. A set of 2-port measurements were conducted to obtain measurements of return loss, trough, coupling and isolation. After each measurement the network analyzer was re-calibrated using the TRL calibration standard over the entire bandwidth allowed by the equipment (69.4 to 116 GHz).

Fig. 4.4 shows the measured reflection (S_{11}) and isolation (S_{41}) of the hybrid. They are in close agreement with the simulation, also presented in the figure, showing values below -20 dB in the entire band.

Amplitude and phase imbalances were initially calculated using the ratio between the measured S_{21} and S_{31} parameters. However, the phase difference between the two ports showed errors associated with the movement of the frequency extenders between calibration and measurements, as reported previously [75]. To overcome this error, a one-port measurement, utilizing short terminations, was used to determine the electrical length of the hybrid. This type of measurement is similar to the one used in the unknown-thru calibration [78].

Fig. 4.5a shows the measured results of the amplitude imbalance. They are below 0.8 dB

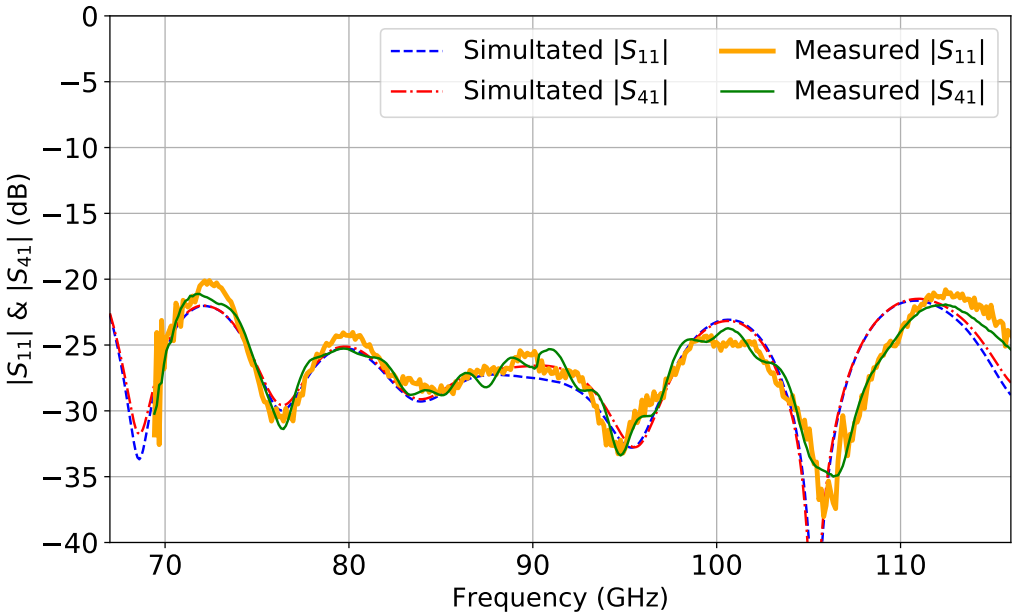

Figure 4.4: Simulated and measured reflection and isolation.

in the entire band but are slightly larger that the simulated values. This difference can arise from the high sensibility of the coupling of the hybrid to the design parameters. Hence, a small inaccuracy in the machining could produce a deviation in the measured magnitude. To verify this hypothesis, a systematic error of $+5\,\mu$m was introduced to the parameter b_B, $+10\,\mu$m to a_B, $-5\,\mu$m to l_B and a independent random value between $\pm 5\,\mu$m to the widths of each matching section, w_i (these values were obtained by measuring the dimensions of the most relevant parameters of the constructed prototype). The simulation results including these errors (also shown in Fig. 4.5a) do indeed present an amplitude imbalance closer to the measurements. Another aspect to note in the experimental results is the presence of a small resonance, near 90 GHz, produced by the excitation of a high-order mode, as discussed in section 4.3, due to construction imperfections. However, its effect is negligible in the overall performance of the hybrid.

Fig. 4.5b shows the measured phase imbalance obtained from the 1-port method, presenting values between $-0.5°$ and $+2°$ in the entire band. Contrary to what happened with the amplitude imbalance, the inclusion of systematic errors in the simulation did not produce a significant variation in the phase imbalance. This suggest that a full explanation of the differences between simulation and experiment would require introducing small asymmetries in all parameters of the model.

Table 4.3 compares this work with other waveguide branch-line quadrature hybrids. It demonstrates the excellent performance of the current hybrid in all figures of merit, including a relaxation in the constraints for the mill needed to machine the branches. Moreover, one important aspect to mention is that its bandwidth is limited by the operational bandwidth of the interface waveguide that is used. Indeed, above 116 GHz the second waveguide mode propagates through the waveguide. This is a fundamental limitation that can be overcome with the use of a non-standard waveguide [62] to fully utilize the bandwidth between the first two fundamental modes of the input waveguide. Consequently, the design presented here could be further optimized for achieving larger

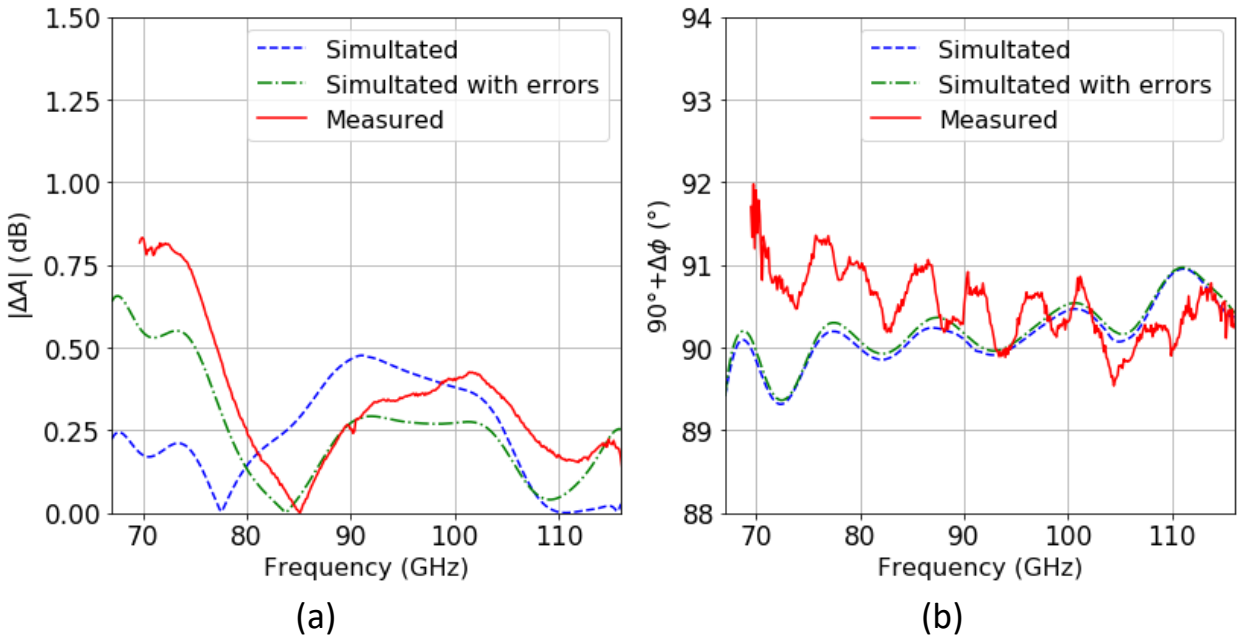

Figure 4.5: (a) Simulated and measured amplitude imbalance. (b) Simulated and measured phase imbalance, centered in 90°.

Table 4.3: Comparison between proposed design and other works.

Paper	$\frac{a_B}{2b_B}$ ⋆	**BW (%)**	**RL (dB)**	**ΔA (dB)**	**$\Delta\phi$ (°)**
This work	6.233	53.5	> 20	< 0.81	< 2.5
[75]	4.635	30.4	> 15	< 0.15	< 8.0
[50]	2.265	37.8	> 15	< 1.20	< 6.6
[62]†,‡	13.333	58.0	> 22	< 0.50	N.A.

⋆Minimum aspect ratio of the tool needed to machine the branches.
†Only simulated results.
‡Non-standard waveguide interface (WR-2.3).

bandwidths with the added advantage of an easier fabrication.

4.5 Conclusion

In this work a modified waveguide branch-line quadrature hybrid with state-of-the-art performance was introduced and successfully implemented in an extended W band. The novelty of this design is the increase of height of the branches which results in easing construction when the split-block technique is used. However, special precaution is needed in the design and construction to avoid the internal propagation of high-order waveguide modes that could produce resonances. Finally, this design could be further optimized by two means. First, by modifying each branch and match section independently, and, secondly, by utilizing non-standard waveguides to increase its fractional bandwidth.

Chapter 5

Development of a multiband heterodyne downconverter for the extended W band

5.1 Introduction

The multiband heterodyne receiver proposed in [20] can be an alternative solution for the necessity of ultra-bandwidth systems in radio-astronomy. This kind of receiver can obtain the complete RF spectrum divided into several parallel IF outputs. This type of architecture can prove competitive with the classic approach used for multi-line observations, which involves complex optic systems including mirrors and dichroic [79]. The multiband receiver architecture was successfully implemented in the 1.85 m mm-submm telescope, obtaining simultaneous observation of the CO lines J = 2-1 and J = 3-2 at 230 and 345 GHz respectively [22]. This receiver works with a frequency multiplexer that separates the RF bandwidth into four sub-bands that are downconverted with the use of an independent SIS mixer to produce SSB observations. This can be accomplished by positioning the LO frequency of each mixer at one end of its respective sub-band. A general diagram of a multiband downconverter indicating all the relevant frequencies is presented in Fig. 5.1.

For this work, we propose the use of multi-band receivers in conjunction with digital sideband separation (2SB). This configuration has the potential to cover the entire RF spectrum instantaneously [34]. The complete instantaneous RF coverage can only be implemented using a digital IF hybrid, that in contrast to the analog ones, is limited in its lower frequencies only by bias circuits of the receiver components and the noise of the LO signal. Then, by placing the LO frequency of the center each sub-band, almost total RF coverage can be achieved. It is worth noticing that since LO frequencies are fixed, the LO noise can be reduced with the used of a fixed oscillator, thus increasing the coverage of the IF frequencies at the lower end. This type of configuration also reduces the complexity of the multiplexer design by a factor of two, for example, if a multiplexer with 4 outputs is needed with the configuration proposed in [20], with this configuration only a multiplexer with two outputs (diplexer) is needed. A general diagram of a multiband downconverter with digital 2SB is presented in Fig. 5.2 for the extended W band.

Since this architecture divides the analog RF spectrum into two bands with half of the band-

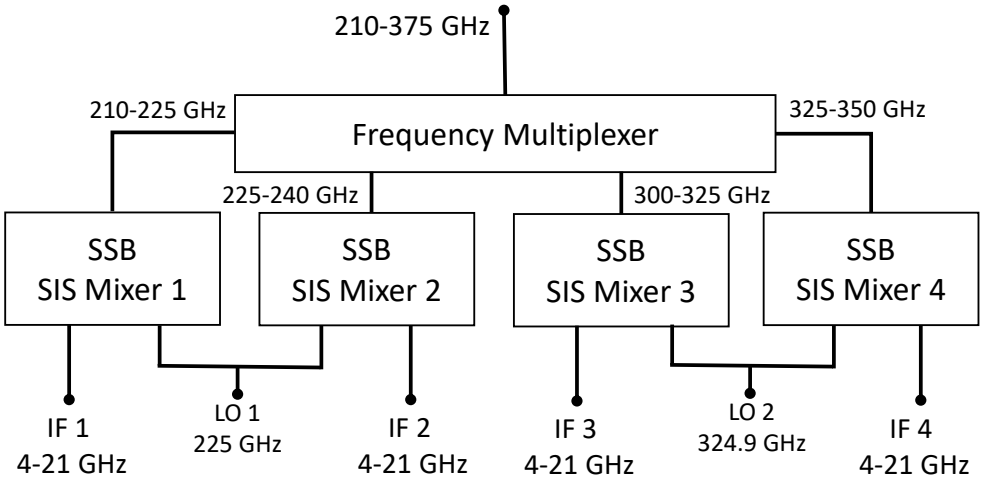

Figure 5.1: General diagram of the multiband receiver proposed in [22]. To minimize the number of LO tones, two sub-bands shares one LO tone, with one band operating in the lower sideband and the other in the upper sideband.

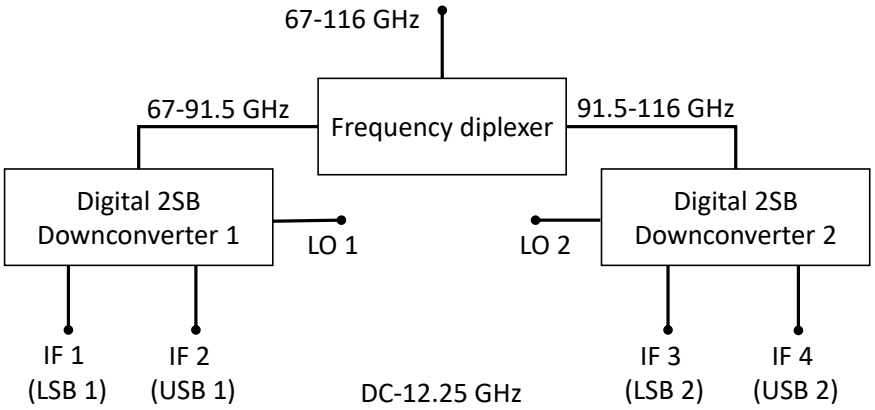

Figure 5.2: Concept of a multiband heterodyne receiver with digital 2SB receivers for the extended W band. The input RF signal is separated into two frequency bands with a diplexer, a device that is capable of selectively routing the signal depending on its frequency. The low RF frequencies (67-91.5 GHz) is transmitted to digital 2SB downconverter 1 and the high RF frequencies (91.5-116 GHz) to downconverter 2. Each downconverter then separates the signals even more to Upper sideband (USB) and Lower Sideband (LSB) with the use of a image rejection mixer configuration.

width, it offers two additional advantages besides instant access to the entire RF spectrum. The first is the reduction of operational bandwidth needed for the electronics of each sub-band. The second is that in consequence of this bandwidth reduction, further optimization can be archive in the performance of the receiver, reducing its overall noise temperature.

Despite the possibility of solving various problems in radio astronomy, not much work has been done in developing this type of architecture yet. The main reason for this is the limitation of IF processing capabilities. However, in recent years, with the development of faster digital processing platforms, this limitation can be overcome. One example of such a platform is the Xilinx AMC590 56 GSPS 8-bit ADC, UltraScale by VadaTech Inc integrated board [80].

In this work, we present the initial development of a multiband heterodyne downconverter with digital 2SB for the extended W band. The following section will present the development, implementation, and measurements of the frequency diplexer, the most important component of the design presented in Fig. 5.2. This work, however, is not yet finished and it only represents the first step to constructing this type of receiver. Furthermore, we also include a section with the complete design and simulation of a proof of concept multiband downconverter.

5.2 RF Frequency Diplexer

Traditionally, frequency diplexers have been implemented as filter banks, which correspond to pass-band filters implemented in parallel [81]. However, a novel design was proposed in [20] based on quadrature hybrids and filters. This design has the advantage of providing minimal return and insertion losses over the entire bandwidth, and excellent isolation between the lower and upper bands. In Fig. 5.3 we present a diagram showing the working principle of the hybrid-based diplexer. If the high-pass and low-pass filters are permuted, the working principle remains the same, but the outputs are interchanged. In the following subsections, we will show the design and simulation of each individual component. The simulations were made using the full electromagnetic simulation ANSYS HFSS. We will also present the manufacture and measurements of the first prototype of the complete diplexer.

5.2.1 Hybrid 1

The bandwidth of the diplexer is primarily limited by the input RF hybrid, thus making it the most critical component of the design. We have done significant work in developing a quadrature hybrid that covers the entire input bandwidth (extended W band) with low amplitude and phase imbalance. The diplexer uses the same design presented in chapter 4, only with a slight modification on the parameter L_B, (from 0.56 to 0.58mm due to further optimization considering the diplexer geometry).

5.2.2 Hybrid 2

The second hybrid only needs to cover the upper-frequency band (91.5-116 GHz). We selected a standard waveguide branch-line hybrid coupler configuration for the design as it requires low fractional bandwidth. In Fig. 5.4 we present the design parameters and simulation results. The hybrid shows good behaviour in the entire upper frequency band, with reflection (S_{11}) bellow -23 dB and amplitude imbalance ($|S_{21} - S_{31}|$) bellow 0.5 dB.

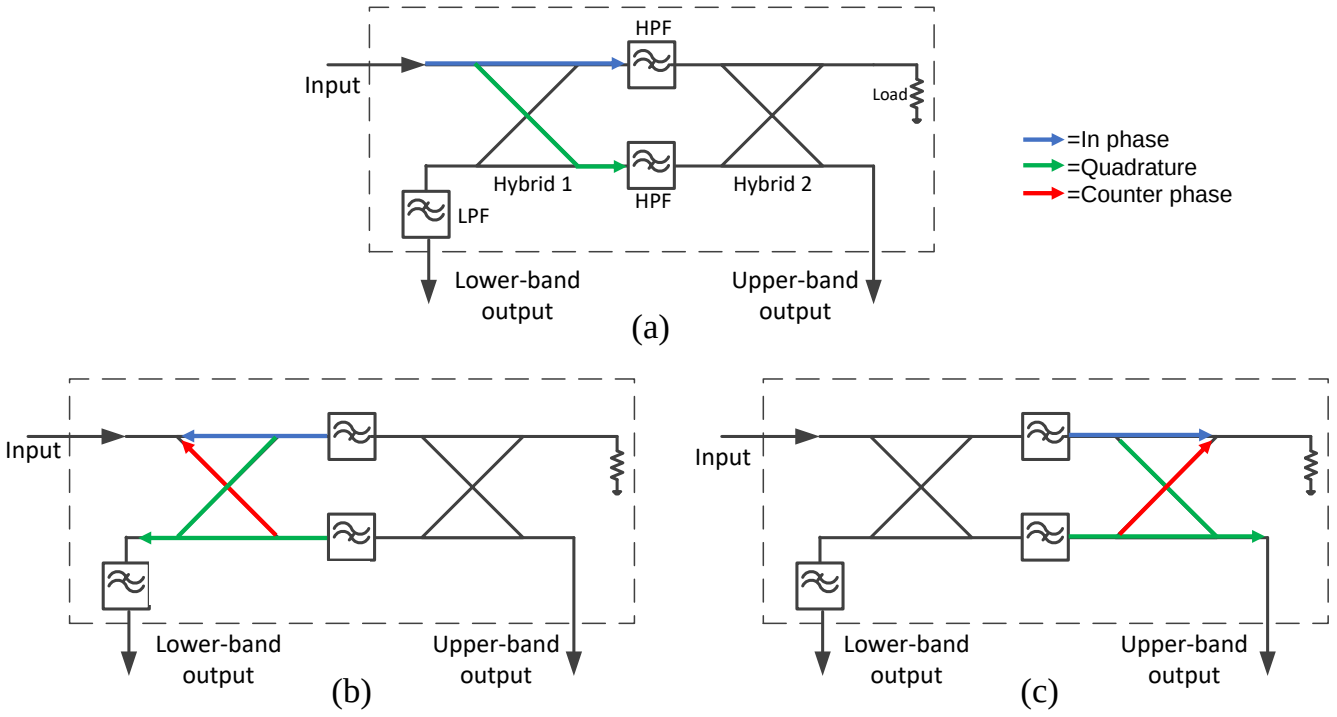

Figure 5.3: Power flow diagrams explaining the fundamental working principle of the hybrid-based diplexer. (a) The input signal is divided by the first quadrature hybrid into two signals 90^{o} apart (b) If the frequency is below the cut-off frequency of the two identical high-pass filters, the signal is reflected back, canceling at the input port and combining at the lower band output. A low-pass filter is also placed at the output to increase rejection. (c) If the frequency is above the cut-off frequency of the two identical high-pass filters, the signal pass through the second quadrature hybrid and combines at the upper-band output. Any residual power, due to non-ideal components, is transmitted to the load.

5.2.3 Filters

For the bandpass filters, we selected a design similar to the one presented in [62]. However, we paid special consideration to mechanical constraints because we needed to build it using tools available at the Millimeter Wave Laboratory (MWL) at Universidad de Chile. We present in Fig. 5.4 the general morphology, design parameters, and HFSS simulation results for the high pass filter. The cutoff frequency of the filter is 91.5 GHz with reflection (S_{11}) below -20 dB in almost the entire band. in contrast to [62], we could not achieve -20 dB for all the bandwidth, because of the mechanical constraints imposed in the design. To further test that a more optimal solution was not possible given the constraints, we used a swarm particle optimization algorithm, with over 5000 iterations, not arriving at the target goal. Even so, the proposed design should not produce any considerable degradation in the performance of the diplexer.

We decided to place an additional low-pass filter at the lower band output to increase the rejection of the upper band. This additional filter was also included in the diplexer design proposed in [62]. We selected to use a small-size-gap corrugated low-pass filter. In Fig. 5.6 we present the general morphology and simulation results. To not affect the S_{11} parameter of the diplexer at the interception of the upper and lower bands, we selected a cut-off frequency of 96 GHz, well above the

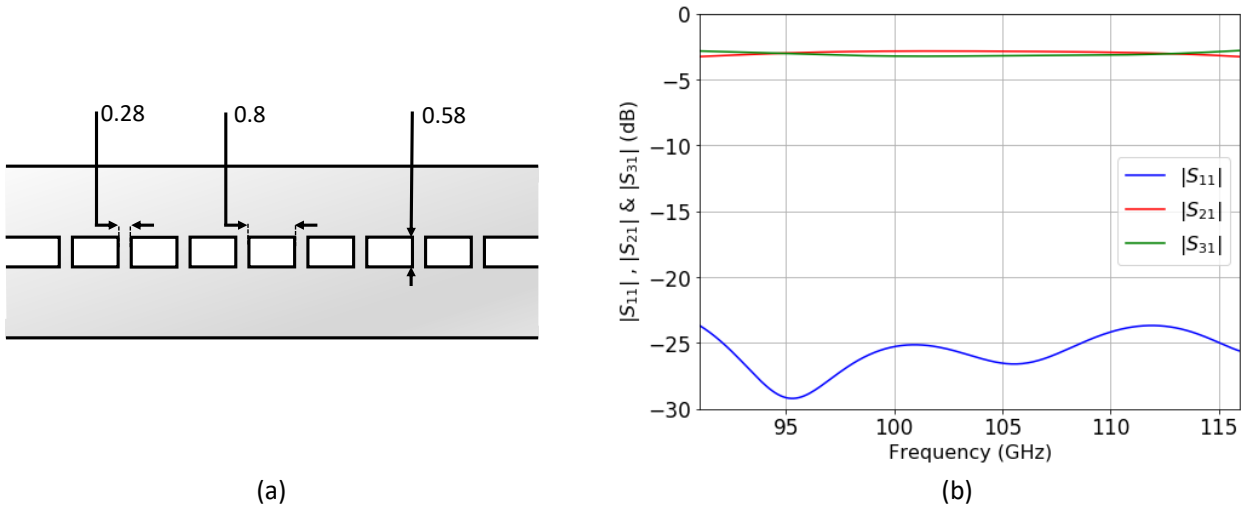

Figure 5.4: (a) Drawing of the proposed hybrid 2, indicating critical dimensions (in mm). The input/outputs are standard WR-10 waveguides, and each of the 8 branch lines has the same dimensions. (b) Simulated S-parameters.

center of the band. Also, some resonant peaks were found over 91 GHz. These peaks, however, do not show any impact on the overall performance of the diplexer. For a future design, the resonance peaks could be eliminated with further optimization of the filter, trying to change its topology to a fully corrugated low pass filter, while maintaining the imposed mechanical constrains.

5.2.4 Diplexer Simulation

We integrated all the simulated components into the frequency diplexer (see Fig. 5.7a) and tuned the distance between each element to achieve an optimal result. The simulation (in Fig. 5.7b) was made utilizing a finite aluminum conductivity boundary condition ($3.8 \cdot 10^7$ siemens/m with no surface roughness) and an ideal RF Load. The main reason for not including a real load was that the computation resources needed to complete the simulation increased significantly. The S_{21} and S_{31} parameters show the transmissions of the lower band and upper band respectively, with an interception point exactly at 91.5 GHz. The cut-off slope for each band matches the behavior of the bandpass filter. The increased rejection in the upper-frequency band above 96 GHz is produced by the inclusion of the low pass filter at the port 2 output. The S_{11} parameter presents good behavior with a reflection below -20 dB in the majority of the band and a maximum value of -16.58 dB at 90.4 GHz.

One critical aspect of the diplexer design is its noise contribution to the receiver. If the diplexer is to be considered as the first element of the receiver chain, its equivalent noise temperature must be minimal to not contribute significantly to the overall receiver noise temperature. This aspect is particularly important as no previous amplification stage is present. Fig.5.8 shows the expected equivalent noise temperature of the diplexer at 296 K (ambient temperature) and at a cryogenic temperature of 4 K (usual temperature to operate SIS mixers). This calculation is made in Cadence AWR, using the passive components noise simulator (not considering a conductivity change beween 296 and 4 K). The results show that the expected noise contribution of the diplexer

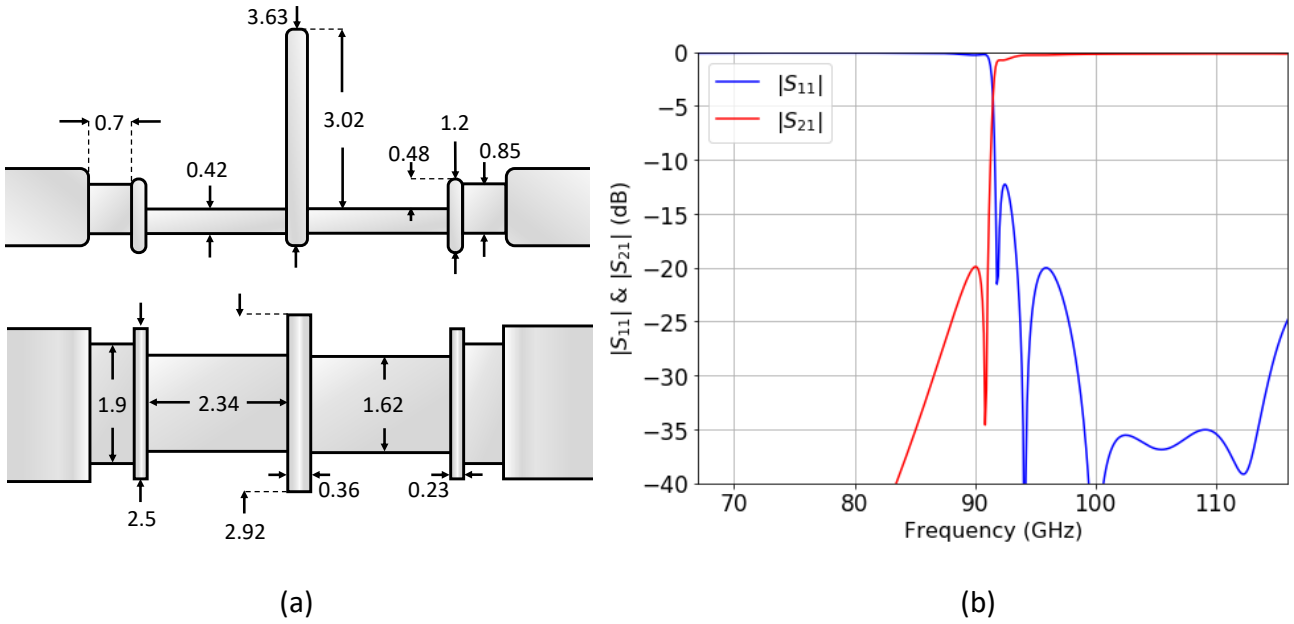

Figure 5.5: (a) E-plane (top) and H-plane (botttom) views of the proposed high-pass filter design indicating critical dimensions (in mm). The input/output are standard WR-10 waveguides. (b) Simulated S-parameters.

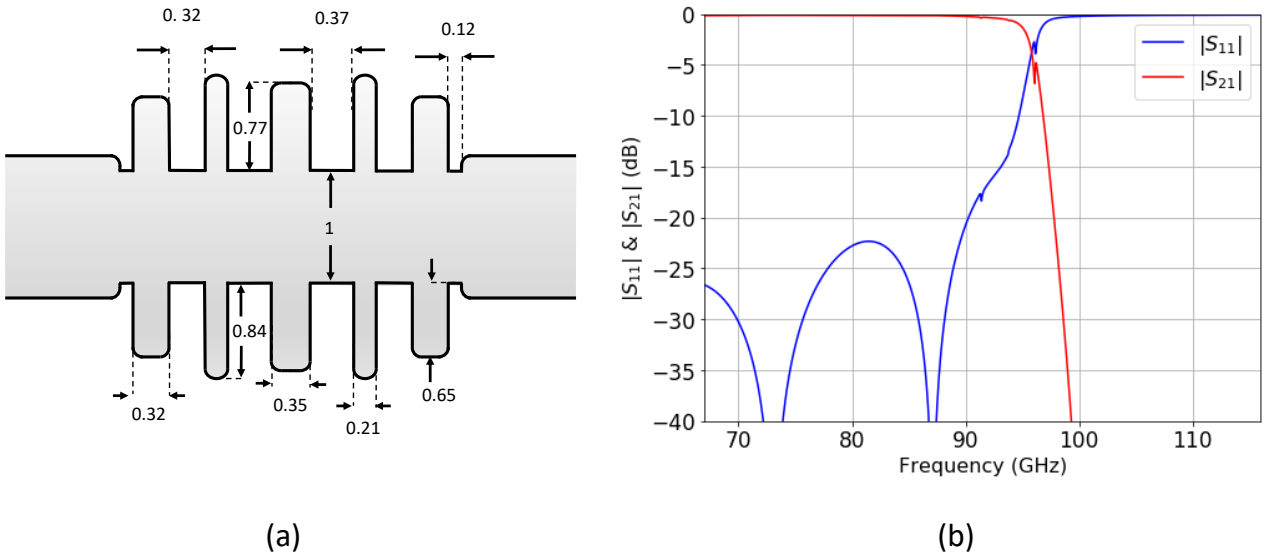

Figure 5.6: (a) Drawing of E-plane of the proposed filter design indicating critical dimensions (in mm). The input/output are standard WR-10 waveguides. (b)S parameter simulation made in HFSS.

is almost constant, at 20 and 0.2 K, respectively, except at the center of the band, where the noise increases as the S_{21} and S_{31} parameter decreases. These results suggest that in order to decrease the noise contribution of the diplexer it must be placed inside the cryostat. One important aspect

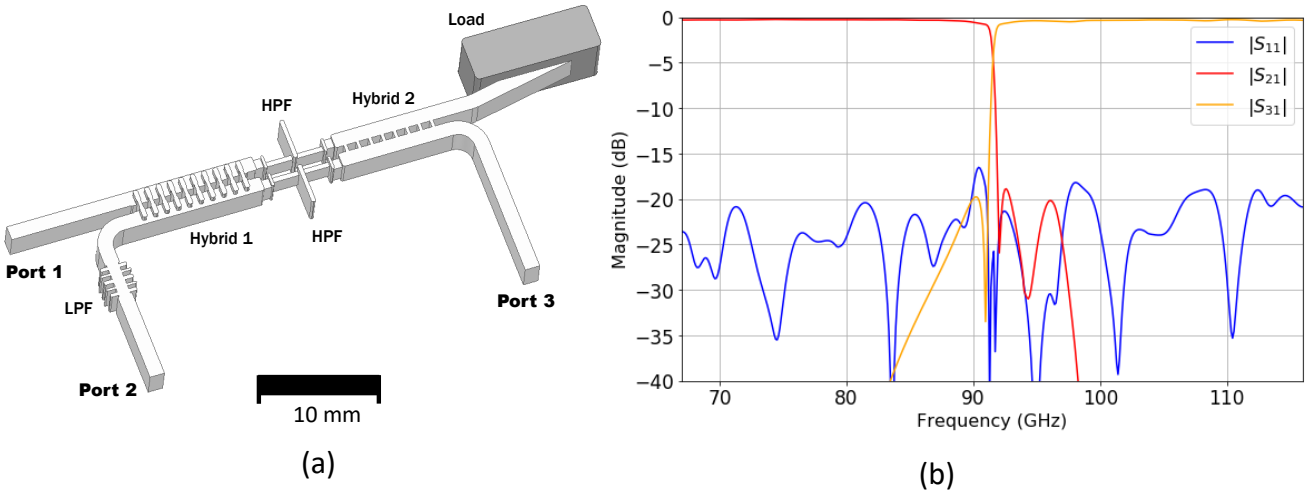

Figure 5.7: (a) HFSS model of the complete diplexer. (b)Simulated S-parameters.

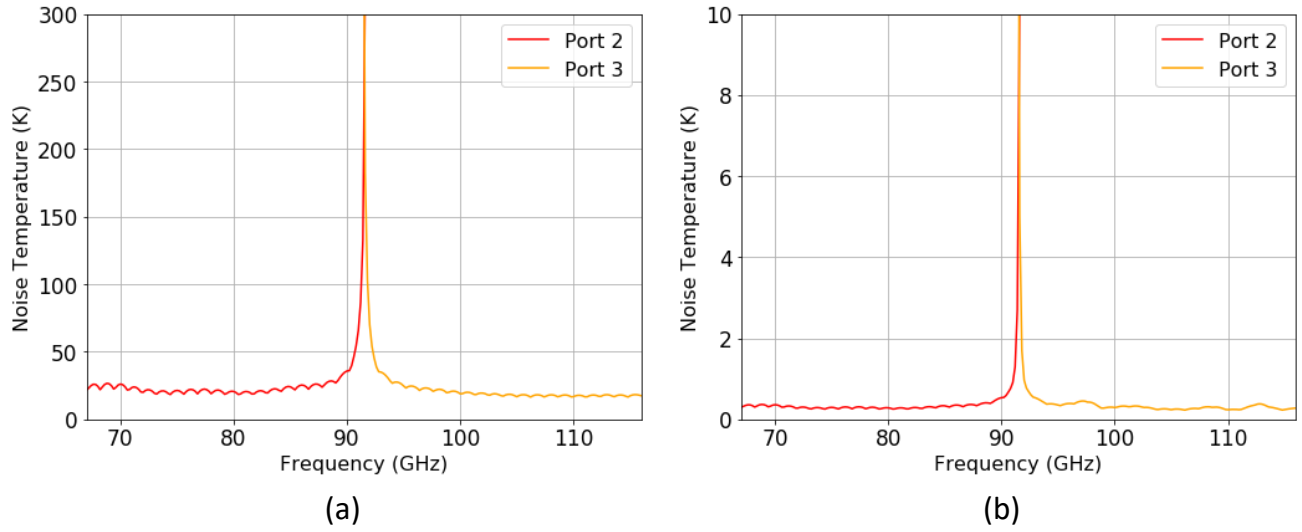

Figure 5.8: Simulated equivalent noise temperature of the diplexer made in Cadence AWR Microwave office. (a) At 296 K and (b) At 4 K.

to consider is the gain drop of at least 3 dB at the interception point between the two bands, which will produce an increment of noise temperature by at least a factor of two in all subsequent elements of the receiver chain. The bandwidth compromised by the gain drop is small (∼1% of the band) and by coherently combining weighted signals from both receiver chains at the band edge, the overall noise temperature of the receiver could not be significantly affected. To accomplish this recombination, the IF bandwidth of each sub-band receiver needs to be increased, to cover the overlapped bandwidth between outputs. The use of a waveguide diplexer also possesses a significant advantage in comparison with the use of a dichroic filter (a more standard solution to separate frequency bands [82]), as the dichroic will take significantly more space inside a cryostat.

Figure 5.9: Picture of the constructed split-block diplexer.

5.2.5 Diplexer Characterization

The designed diplexer was manufactured using the split-block technique in an aluminum block using a Kern high-precision milling machine, we present the constructed diplexer in Fig 5.9. The load required in the diplexer was implemented using MF-124 from ECCOSORB®.

Since the MWL does not have a vector network analyzer for the W band, we only made scalar measurements utilizing an Agilent PSG Signal Generator E8257D with an OML W-band Extension Module and an Agilent PXA Signal Analyzer N9030A with a W-band waveguide harmonic mixer, as the RF source and detector respectively. We present in Fig. 5.10 the test setups used to measure transmission ($|S_{21}|$ and $|S_{31}|$) and reflection ($|S_{11}|$). Isolators were used at the end of each instrument for protection. A variable attenuator was placed to control the power of the RF tone and avoid saturation of the spectrum analyzer. A calibration plane was used to eliminate loss contributions of the setup, making the measurement relative. As the frequency extender of the spectrum analyzer only operates up to 112 GHz, measurements above that frequency were not possible.

In Fig. 5.11a we present the scalar S Parameter measurements of the constructed diplexer. In the $|S_{21}|$ and $|S_{31}|$ parameters we can see two well-defined transmission bands for the lower and upper-frequency outputs. The interception point between the two frequency bands is at 91.05 GHz, less than 500 MHz apart from its expected value (91.5 GHz). However, the shape of the cut-off slope of the $|S_{21}|$ parameter differs from the simulation. We can explain this difference due to various manufacturing errors in the filter and upper-frequency hybrid sections of the constructed block. Some pictures showing these errors are presented in Fig. 5.11b. These manufacture errors also

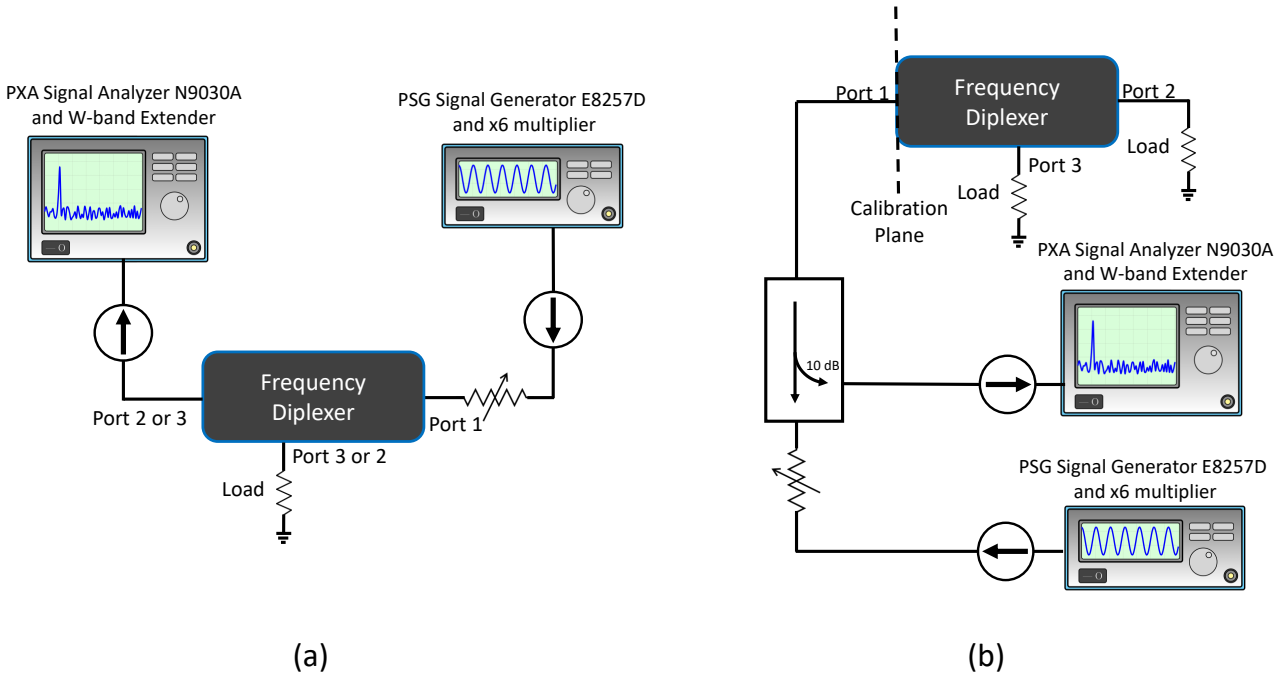

Figure 5.10: Proposed setup configurations to measure scalar parameters. (a) Transmissions are measured directly by connecting the source and the detector. (b) Reflection is measured utilizing a directional coupler to sample the reflected signal.

explain the behavior of the $|S_{11}|$ parameter, the lower-frequency band presents an overall higher value (bellow -10.8 dB) in comparison with the lower-frequency band (bellow -14.7 dB). This difference is produced by asymmetries between the two band-pass filters, producing an ineffective cancellation of the reflected wave at the input port.

Other aspect to notice, from Fig. 5.11a, is that the diplexer losses possess an average value of 2,1 dB for the lower-frequency band, and 1.5 dB for the upper-frequency band. This difference between the two bands can be explained by the different values of reflections at each sub-band. A simulation considering the actual input waveguide dimension of the split block and a corrected aluminum conductivity based on the one reported in [83] was made, obtaining a typical value of 0.7 dB of loss at the pass-band. This value would increment the noise temperature of the diplexer to 50 K at room temperature. At cryogenic temperatures, the reported conductivity value is similar to one used in Fig. 5.8b. Even accounting for all these factors, the measured losses exceed the expected simulation values. The reason for this behaviour is not clear, although this increment in losses could originate from manufacturing errors or problems with the measurement setup. It is worth noticing that a similar behavior was also found in other constructed diplexers such as [62] and [22] so it can not be discarded that it could be an inherent problem with this type of diplexer design.

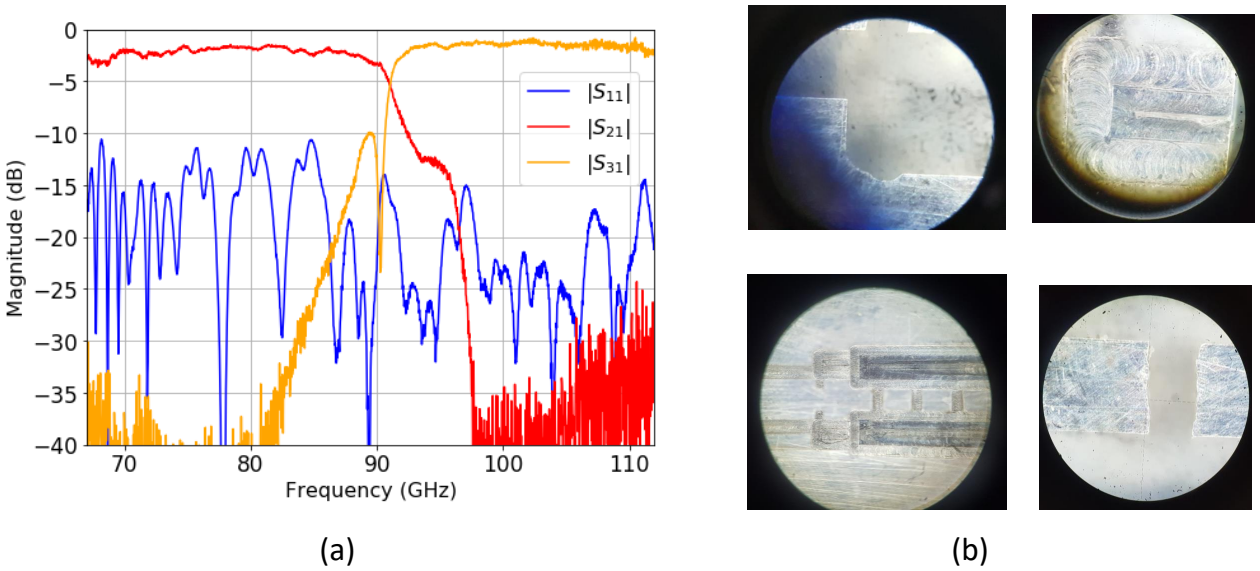

Figure 5.11: (a) Scalar S parameter measurements results of the constructed diplexer. (b) Pictures obtained during metrology measurements show examples of significant construction errors.

5.3 Looking into the future: Proposal of a proof-of-concept wideband downconverter

In this section we propose the design of a prototype receiver based in the general diagram shown in Fig.5.2, using the diplexer presented in the previous section. The design includes a complete simulation of the proposed prototype using a hypothetical 24.5 GSPS ADCs and a digital processing platform. Before presenting the design and simulations, several key elements and aspects will be discussed in the following subsections.

5.3.1 I/Q mixers

As stated in the introduction, the downconverter elements can be optimized in performance for each sub-band. However, this advantage will not be discussed in this chapter. There are different downconverter architectures that can be implemented in this design, one option is to use the one proposed in Chapter 2. Nevertheless, for the first prototype, we propose a more simple approach with only a mixing element and no gain. We selected an original I/Q MMIC sub-harmonic mixer (Fig. 5.12) based on the mixer design that was already presented in Chapter 2. The I/Q IF output of the mixers then are passed to a digital back-end, where a hybrid and side-band separation can be implemented digitally [29]. We present a complete harmonic balanced simulation of this design in conjunction with all the other critical components in section 5.3.5.

5.3.2 LO distribution

The LO distribution for the mixer elements is an important aspect to be considered. The most simple approach is the use of two different ports to feed each mixer independently. This alternative. however, increases the overall size of the module for the proposed prototype, since two standard

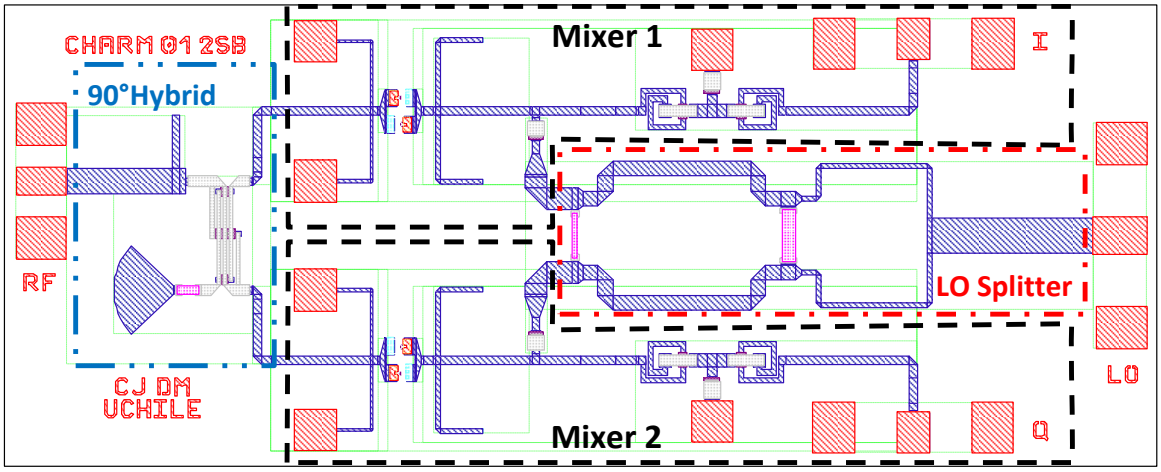

Figure 5.12: Final layout of I/Q mixer CHARM012SB. In this design, two mixers were put on the same MMIC, connected to the input by a planar Lange coupler, a type of quadrature hybrid. The LO signal is feed by a single input and split to both mixer by a broadband multi-stage Wilkinson divider[51].

WR-19 waveguide flanges are needed. Coaxial connectors could also be used, but given the losses of coaxial cables at those frequencies, their use is not recommended. If we want to use only one input port, the most intuitive way to distribute the LO is the use of a power splitter. This alternative presents two problems. First, a loss of 3 dB in LO power. And second, the two LO signals arrive at each mixer, generating undesired inter-modulation products, affecting the performance of the downconverter. Another alternative is the use of another diplexer for the LO signal. This solution does not have power loss and only one LO tone is supplied to the appropriate mixer. However, as waveguide components are known to be bulky, especially in lower frequencies (and even more considering a sub-harmonic mixer solution), the LO diplexer needs to be positioned adequately. For the first prototype we will use the simplest approach of having two independent ports, as we don't have a restriction for the total size of the receiver.

5.3.3 Additional Components

Additional components to make a completely functional design were also designed. These components include waveguide to microstrip transitions for the LO and RF ports and the microstrip IF paths. We proposed the use of a traditional rectangular waveguide to microstrip transitions based in [84], that has already been used successfully for the desired fractional bandwidth [27]. For the IF paths, a layer change in the mechanical block has to be implemented, as the geometric distribution of the block impedes the arbitrary positioning of the IF outputs at any arbitrary lateral face of the block. To implement these paths we will use a coaxial transition medium for the layer change, this method has proven successful in other works such as [85]. As the coaxial medium, we plan to use a Southwest Microwave coaxial hermetic glass seal model 290-07G.

5.3.4 Proposed design

In Fig. 5.13 we present the general design of the proof-of-concept multiband heterodyne downconverter for the extended W band. Its main components are the diplexer presented in section 5.2

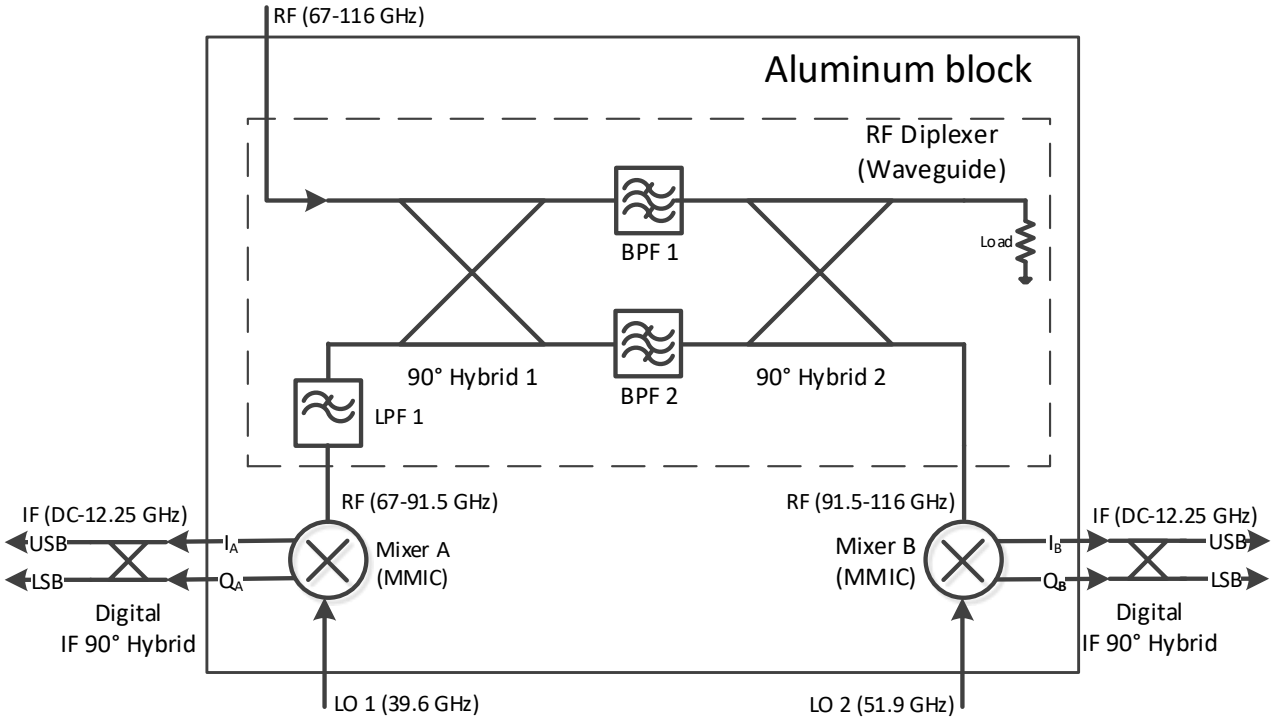

Figure 5.13: Diagram for the first prototype of a diplexer-based downconverter module.

and the I/Q MMIC presented in section 5.3.1.

The proposed design uses a modular assembly similar to one proposed in [27]. In this way it is possible to test each component of this architecture (diplexer and mixers) separately in a progressive way. The downside of this approach is that the overall size of the prototype increases, but it also minimizes possible problems in its implementation. Moreover, the proposed design considers enough space between the lower and outer band mixers to implement the other type of LO distribution discussed in section 5.3.2. The proposed mixer block design, considering all its elements, is presented in Fig. 5.14.

5.3.5 Simulations

The proposed multiband downconverter simulations were made using Cadence AWR. A full EM simulation of the diplexer using HFSS, including the waveguide to microstrip transitions, was imported into AWR using touchstone sNp files. The MMICs were originally designed using AWR, so they were simulated directly. The bondwires were simplified as series inductors and the IF microstrip paths were also imported from HFSS. With all the components combined, a non-linear multi-tone harmonic balance simulation was made for the entire downconverter. Simulation results for the four IF ports (intermodulation tone corresponding to $f(RF) - 2 \cdot f(LO)$) projected over RF are presented in Fig. 5.15, utilizing an ideal IF hybrid to achieve sideband separation. The simulation was normalized over the minimum conversion loss value (9.92 dB), for better visualization of the rejection between the lower and upper sidebands. Results show complete RF bandwidth coverage over the four IFs. A resonance is noticeable at 76 GHz, despite the fact that is not present in the diplexer or the waveguide to microstrip transitions. Therefore, it appears to be caused by

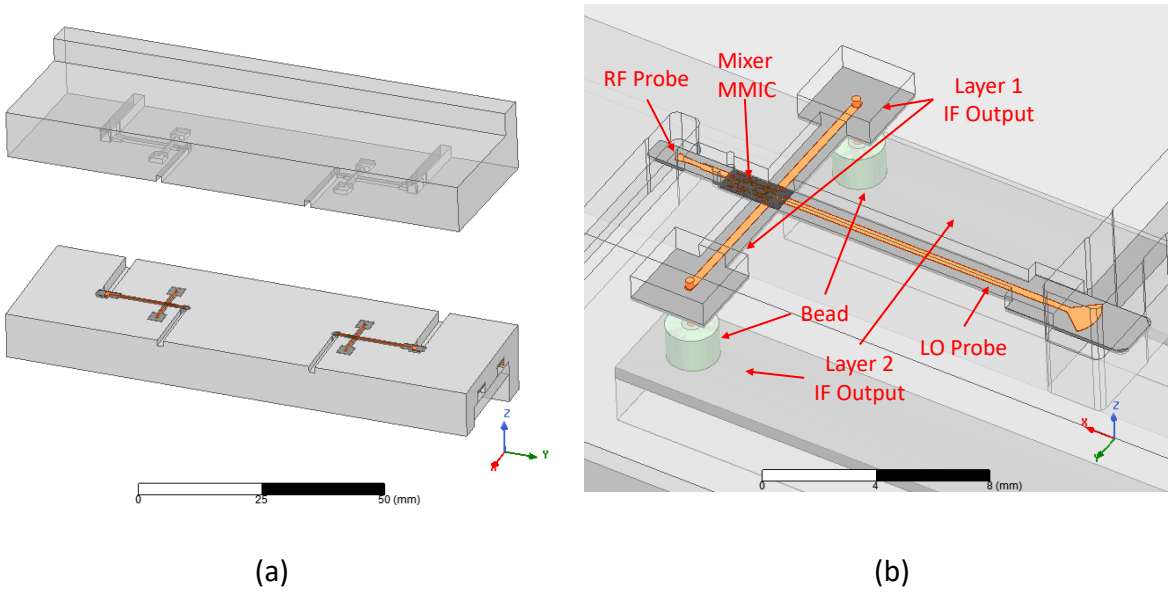

Figure 5.14: (a) CAD image of the proposed mixer block. (b) Image of one of the mixers with all its components including the MMIC, RF and LO probes, and IF paths with a layer change.

the mixers, therefore, will require special attention in its future implementation. The cut-off of the upper and lower bands follows the same behavior of the diplexer simulation and is projected in all the IF ports. Sideband separation with the ideal hybrid shows poor performance in some sectors of the band. However, the overall performance has a sideband rejection ratio between 10 and 20 dB, which can be increased with digital calibration.

Utilizing the harmonic information components of the AWR simulation, the four I/Q IF outputs were reconstructed as input time data for a simulation made in Python. The signal is then sampled at 24.5 GSPS and the digital sideband separation method explained in [29] was used to create a digital hybrid composed of four complex constants by frequency channel (IF resolution bandwidth). Fig. 5.16 shows the simulated SRR with ideal (performing as a perfect hybrid) and calibrated constants. The ideal constants give results similar to the original AWR simulation utilizing an ideal hybrid. In contrast, the use of calibrated constants give a SRR over 48 dB. To further test the robustness of the calibration, an additional AWR non-lineal simulation was made with a slightly different LO setting (0.1 dBm), thus changing the operation point of the mixers. Originally, simulation results showed a noticeable decrease in performance at the beginning of the band, however, after increasing the lower band LO power ($\sim$2 dB), this degradation was eliminated showing a consistent SRR across the entire band. This result shows how significant is the selection of the LO power setting and how it affects the performance of the receiver.

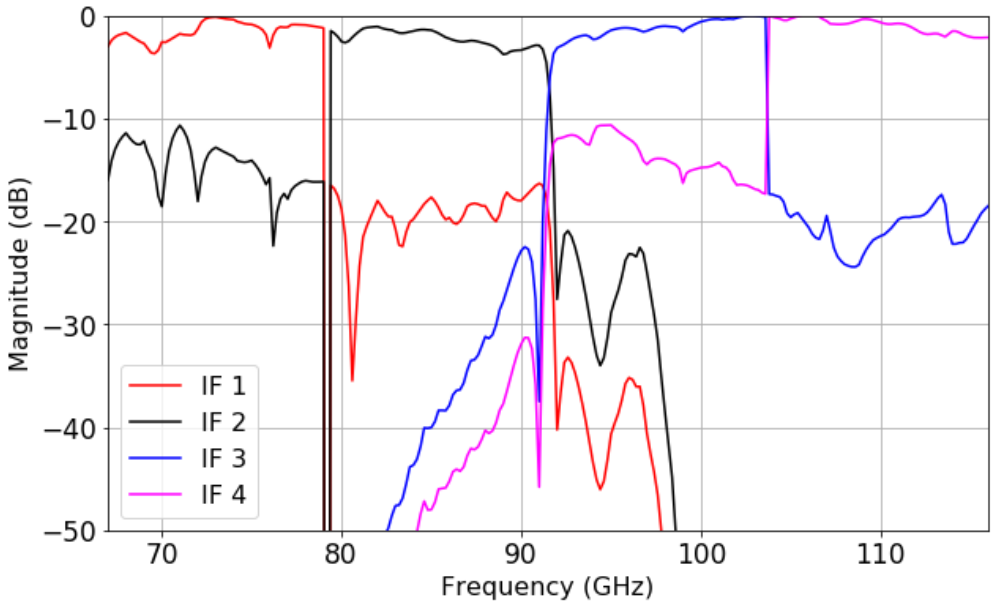

Figure 5.15: AWR non-linear simulations of the normalized IF power of the proposed downconverter prototype with an ideal IF hybrid at its output.

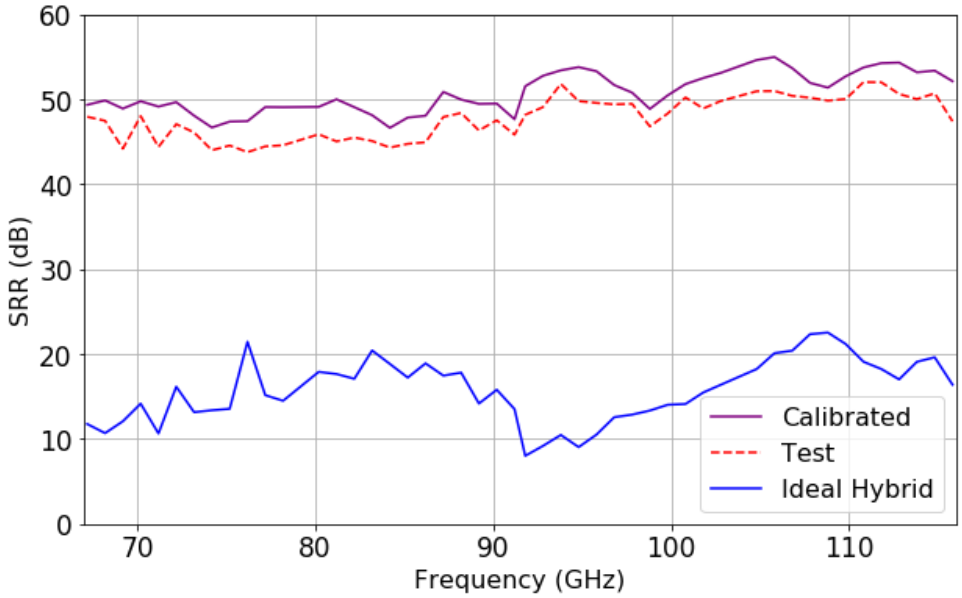

Figure 5.16: Simulation of SRR utilizing the digital sideband separation method proposed in [29]. A test dataset was used to test the robustness of the calibration.

5.4 Conclusion

In the first part of this chapter we have presented the complete design, simulation, and characterization of a frequency diplexer for the extended W band. Design and simulation showed good behavior. However, due to manufacturing errors, the measurements of the constructed diplexer

did not show the same performance. To further verify the design, a new diplexer needs to be built, this new version will not include a significant change in the design, instead, some minor practical alterations will be made such as greater milling radius at some of the diplexer internal edges to decrease the milling time.

In the second part of this chapter, we presented simulations of a hypothetical receiver that has the potential of covering the complete extended W band, with 49 GHz of instantaneous bandwidth in four IF outputs. This type of receiver has never been attempted before and as technology progresses, the work presented here should be continued in order to develop new state-of-the-art receivers for the next-generation telescopes.

Chapter 6

Conclusions

6.1 General Conclusions

We have developed a W-Band (75-110 GHz) compact downconverter suitable for FPA applications. This downconverter has a balanced architecture that produces excellent return loss at the input port. This compact downconverter is presented in chapter 2 as the first publication produced in this PhD thesis [31]. Despite its good performance, several problems were detected, the most relevant was a downgrade in performance near the center of the band produced by an instability in the LNA MMIC cavity. Moreover, the RF bandwidth was limited only to the W band, mainly due to the bandwidth of the input RF quadrature hybrid.

To solve the problem of the instability produced by the cavity of the LNA MMIC a mode-suppressing metasurface consisting of a bed-of-nails (BoN) periodic structure acting as a perfect magnetic conductor was designed. This metasurface is presented in chapter 3 as the second publication produced in this PhD thesis [32]. Experimental results show excellent performance completely suppressing the instability that was present in the constructed downconverter.

To increase the RF bandwidth of the downconverter, a novel modified branch-line waveguide quadrature hybrid design was developed for an extended W band. This new design is presented in chapter 4 as a paper draft. This draft will be the base for a new publication in collaboration with Chalmers University [33]. Simulation and experimental results show state of the art performance with amplitude imbalance below 0.8 dB and a phase imbalance between $-0.5°$ and $+2°$. This design is also of significant importance for the diplexer that is going to be used for the multiband heterodyne downconverter that is proposed in this PhD thesis.

We also proposed a proof of concept multiband heterodyne receiver that utilizes digital side-band separation to obtain the complete RF bandwidth into four IF channels of 12.25 GHz. We designed and manufactured a frequency diplexer covering a RF bandwidth from 67 to 116 GHz using the mentioned quadrature hybrid as its main component. This development is presented in the first half of chapter 5. Simulation results show excellent performance, however, the constructed diplexer presented significant manufacturing errors that diminished its performance. The manufacturing problems were produced by a programming error in the CNC milling machine, due to the high complexity of the design and the quality of the tools. The diplexer needs to be manufactured again

to completely validate the proposed design.

We also made simulations of a complete multiband heterodyne downconverter without an amplification stage. This hypothetical downconverter is presented in the second half of chapter 5. Simulation results show that with the appropriate back-end is possible to cover the complete RF bandwidth instantaneously, potentially reducing the observation time and allowing multi-line observations.

6.2 Future Work

For future work, we propose to upgrade the design of the compact downconverter for FPA applications with the metasurface and new quadrature hybrid to extend its operational bandwidth. We also proposed to continue the work in multiband heterodyne receiver architecture by first building a new improved revision of the diplexer. Then, we proposed to build the downconverter prototype and test it utilizing a second down-conversion stage with smaller IF bandwidth and a mobile LO and implement digital sideband separation in a FPGA based back-end.

Bibliography

[1] B. K. Silva, "Chile: A center of global astronomy, 1850–2019," in *Oxford Research Encyclopedia of Latin American History*, Oxford University Press USA, 2020.

[2] A. Nishimura, K. Tokuda, R. Harada, Y. Hasegawa, S. Ueda, S. Masui, R. Konishi, Y. Yamasaki, H. Kondo, K. Yokoyama, *et al.*, "Current status and future plan of Osaka Prefecture University 1.85-m mm-submm telescope project," in *Ground-based and Airborne Telescopes VIII*, vol. 11445, pp. 1342–1354, SPIE, 2020.

[3] M. Aravena, J. Austermann, K. Basu, N. Battaglia, B. Beringue, F. Bertoldi, F. Bigiel, J. Bond, P. Breysse, C. Broughton, *et al.*, "CCAT-prime collaboration: Science goals and forecasts with Prime-Cam on the Fred Young submillimeter telescope," *arXiv preprint arXiv:2107.10364*, 2021.

[4] T. L. Wilson, K. Rohlfs, and S. Hüttemeister, *Tools of radio astronomy*, vol. 5. Springer, 2009.

[5] J. Carpenter, D. Iono, F. Kemper, and A. Wootten, "The ALMA development program: Roadmap to 2030," *arXiv preprint arXiv:2001.11076*, 2020.

[6] D. M. Pozar, *Microwave engineering*. John wiley & sons, 2012.

[7] T. Mroczkowski, C. De Breuck, C. Kemper, N. Phillips, G. Fuller, M. Beltrán, R. Laing, G. Marconi, L. Testi, P. Yagoubov, *et al.*, "Wide bandwidth considerations for ALMA Band 2," *arXiv preprint arXiv:1905.09064*, 2019.

[8] R. Finger, *Design and construction of a digital sideband separating spectrometer for the 1.2-Meter Southern Radio Telescope*. PhD thesis, Universidad de Chile, 2013.

[9] A. Rogalski, "Progress in focal plane array technologies," *Progress in Quantum Electronics*, vol. 36, no. 2-3, pp. 342–473, 2012.

[10] P. F. Goldsmith, "Sub-millimeter heterodyne focal-plane arrays for high-resolution astronomical spectroscopy," *URSI Radio Science Bulletin*, vol. 2017, no. 362, pp. 53–73, 2017.

[11] D. Cunnane, J. H. Kawamura, M. A. Wolak, N. Acharya, X. X. Xi, and B. S. Karasik, "Optimization of parameters of MgB 2 hot-electron bolometers," *IEEE Transactions on Applied Superconductivity*, vol. 27, no. 4, pp. 1–5, 2017.

[12] E. Novoselov and S. Cherednichenko, "Low noise terahertz MgB2 hot-electron bolometer mix-

ers with an 11 GHz bandwidth," *Applied Physics Letters*, vol. 110, no. 3, p. 032601, 2017.

[13] F. Sizov, "THz radiation sensors," *Opto-electronics review*, vol. 18, no. 1, pp. 10–36, 2010.

[14] D. N. Held and A. R. Kerr, "Conversion loss and noise of microwave and millimeterwave mixers: Part 1-theory," *IEEE Transactions on Microwave Theory and Techniques*, vol. 26, no. 2, pp. 49–55, 1978.

[15] M. Britcliffe, D. Hoppe, and V. Vilnrotter, "Focal-plane array receiver systems for space communications," *Interplanetary Network Progress Report*, vol. 170, pp. 1–18, 2007.

[16] T. Ton, T. Chen, K. Chang, H. Wang, T. Tan, G. Dow, G. Hayashibara, B. Allen, and J. Berenz, "A W-band monolithic InGaAs/GaAs HEMT Schottky diode image reject mixer," in *GaAs IC Symposium Technical Digest 1992*, pp. 63–66, IEEE, 1997.

[17] M. Ferndahl, M. Gavell, M. Abbasi, and H. Zirath, "Highly integrated E-band direct conversion receiver," in *2012 IEEE Compound Semiconductor Integrated Circuit Symposium (CSICS)*, pp. 1–4, IEEE, 2012.

[18] J. Zhang, Y. Ye, R. Tong, and X. Sun, "A highly integrated direct conversion receiver for E-band wireless communication," in *2014 IEEE International Wireless Symposium (IWS 2014)*, pp. 1–4, IEEE, 2014.

[19] O. Noroozian, A. R. Kerr, J. G. Mangum, P. K. Day, H. G. Leduc, J. Zmuidzinas, D. P. Woody, A. W. Lichtenberger, M. Cyberey, and R. Weikle, "Superconducting parametric amplifiers: The next big thing in (sub) millimeter-wave receivers," in *2018 United States National Committee of URSI National Radio Science Meeting (USNC-URSI NRSM)*, pp. 1–2, IEEE, 2018.

[20] T. Kojima, A. Gonzalez, S. Asayama, and Y. Uzawa, "Design and development of a hybrid-coupled waveguide multiplexer for a multiband receiver," *IEEE Transactions on Terahertz Science and Technology*, vol. 7, no. 1, pp. 10–19, 2016.

[21] D. Riquelme, L. Bronfman, R. Mauersberger, R. Finger, C. Henkel, T. Wilson, and P. Cortés-Zuleta, "The diffuse molecular component in the nuclear bulge of the Milky Way," *Astronomy & Astrophysics*, vol. 610, p. A43, 2018.

[22] S. Masui, Y. Yamasaki, H. Ogawa, H. Kondo, K. Yokoyama, T. Matsumoto, T. Minami, M. Okawa, R. Konishi, S. Kawashita, *et al.*, "Development of a new wideband heterodyne receiver system for the Osaka 1.85-m mm-submm telescope–receiver development & the first light of simultaneous observation in 230GHz and 345GHz bands with an SIS-mixer with 4-21GHz IF output," *arXiv preprint arXiv:2105.07786*, 2021.

[23] P. Yagoubov, A. Gonzalez, V. Tapia, N. Reyes, F. Mena, R. Nesti, F. Cuttaia, S. Ricciardi, and F. Villa, "67–116 GHz optics development for ALMA band 2–3 receivers," in *2016 41st International Conference on Infrared, Millimeter, and Terahertz waves (IRMMW-THz)*, pp. 1–2, IEEE, 2016.

[24] P. J. Sobis, A. Emrich, and J. Stake, "A low VSWR 2SB schottky receiver," *IEEE Transactions*

on Terahertz Science and Technology, vol. 1, no. 2, pp. 403–411, 2011.

[25] P. Voll, L. Samoska, S. Church, J. M. Lau, M. Sieth, T. Gaier, P. Kangaslahti, M. Soria, S. Tantawi, and D. Van Winkle, "A G-band cryogenic MMIC heterodyne receiver module for astronomical applications," *International Journal of Microwave and Wireless Technologies*, vol. 4, no. 3, pp. 283–289, 2012.

[26] K. Devaraj, S. Church, K. Cleary, D. Frayer, R. Gawande, P. Goldsmith, J. Gundersen, A. Harris, P. Kangaslahti, A. Readhead, *et al.*, "Argus: A scalable W-band 16-pixel focal plane array for the Green Bank telescope," in *The Interstellar Medium in High Redshift Galaxies Comes of Age, NRAO Conference Series*, vol. 28, 2012.

[27] C. Jarufe, *Development of modular components for radio astronomical receivers in the bands Q (30–50 GHZ) and W (80–110 GHZ)*. PhD thesis, Universidad de Chile, 2018.

[28] Analog, "HMC1144 datasheet." `https://www.analog.com/media/en/technical-documentation/data-sheets/HMC1144.pdf`, 2020. Accessed: 2020-05-08.

[29] R. Finger, P. Mena, N. Reyes, R. Rodriguez, and L. Bronfman, "A calibrated digital sideband separating spectrometer for radio astronomy applications," *Publications of the Astronomical Society of the Pacific*, vol. 125, no. 925, p. 263, 2013.

[30] LNF, "Low noise factory W-band LNA datasheet." `https://www.lownoisefactory.com/files/3014/8944/0607/LNF-LNC65_115WA.pdf.`, 2017. Accessed: 2019-09-30.

[31] D. Monasterio, C. Jarufe, D. Gallardo, N. Reyes, F. P. Mena, and L. Bronfman, "A compact sideband separating downconverter with excellent return loss and good conversion gain for the W Band," *IEEE Transactions on Terahertz Science and Technology*, vol. 9, no. 6, pp. 572–580, 2019.

[32] D. Monasterio, N. Castro, J. Pizarro, F. Pizarro, and F. P. Mena, "A mode-suppressing metasurface for large-width mmics suitable for tightly packaged millimeter and submillimeter heterodyne receivers," *IEEE Transactions on Terahertz Science and Technology*, vol. 11, no. 6, pp. 712–715, 2021.

[33] I. Lapkin, C. Lopes, D. Monasterio, F. P. Mena, and V. Belitsky, "Waveguide hybrid for mm and submm wavelengths with enhanced bandwidth, amplitude and phase balance," *to be submitted to IEEE Transactions on Terahertz Science and Technology*, 2022.

[34] D. Monasterio and F. P. Mena, "Development of a multiband heterodyne receiver with 49 GHz of instantaneous if bandwidth," in *ALMA Front End Development workshop*, p. 9, 2021.

[35] R. Güsten, A. Baryshev, A. Bell, A. Belloche, U. Graf, H. Hafok, S. Heyminck, S. Hochgürtel, C. Honingh, K. Jacobs, *et al.*, "Submillimeter heterodyne arrays for APEX," in *Millimeter and Submillimeter Detectors and Instrumentation for Astronomy IV*, vol. 7020, p. 702010, International Society for Optics and Photonics, 2008.

[36] K.-F. Schuster, C. Boucher, W. Brunswig, M. Carter, J.-Y. Chenu, B. Foullieux, A. Greve, D. John, B. Lazareff, S. Navarro, *et al.*, "A 230 GHz heterodyne receiver array for the IRAM

30 m telescope," *Astronomy & Astrophysics*, vol. 423, no. 3, pp. 1171–1177, 2004.

[37] A. Kerr, B. Eric, T. Crowe, N. Erikson, R. Fisher, P. Goldsmith, C. Gottlieb, C. Groppi, J. Hesler, T. Hunter, *et al.*, "In support of instrument technology development for THz astronomy," *Astro2010: The Astronomy and Astrophysics Decadal Survey*, vol. 2010, p. 29, 2009.

[38] UMS, "Take advantage of very high frequency and cost effective UMS BES Schottky diode process." `https://www.ums-gaas.com/wp-content/uploads/2018/01/2018-Fall-UMS-proposes-a-shared-foundry-run-on-BES-process_Euro2.pdf`, 2018. Accessed: 2020-01-13.

[39] J. W. Kooi, *Advanced receivers for submillimeter and far infrared astronomy*. Rijkuniversiteit Groningen, 2008.

[40] OMMIC, "CGY2190UH/C2 datasheet." `https://www.ommic.com/datasheets/OMMIC_DATASHEET_LNA_CGY2190UH-C2.pdf`, 2018. Accessed: 2020-04-29.

[41] R. Gawande, R. Reeves, L. Samoska, K. Cleary, A. C. Readhead, T. Gaier, P. Kangaslahti, M. Varonen, S. Church, K. Devaraj, *et al.*, "W-band IQ sub-harmonic mixers with low LO power for cryogenic operation in large arrays," in *2014 9th European Microwave Integrated Circuit Conference*, pp. 301–304, IEEE, 2014.

[42] T. H. Lee and T. H. Lee, *Planar microwave engineering: a practical guide to theory, measurement, and circuits*, vol. 1. Cambridge university press, 2004.

[43] N. I. Corporation, "Microwave Office for MMICs, Microwave Office application datasheet." `https://www.awr.com/serve/mmics-datasheet`, 2019.

[44] R. Yadava, *Microwave Engineering: Principle and Devices*. Notion Press, 2018.

[45] V. Intertechnology, "High frequency 50 GHz thin film chip resistor." `https://www.vishay.com/docs/53014/ch.pdf`, 2019.

[46] A. U. Zaman, M. Alexanderson, T. Vukusic, and P.-S. Kildal, "Gap waveguide PMC packaging for improved isolation of circuit components in high-frequency microwave modules," *IEEE Transactions on Components, Packaging and Manufacturing Technology*, vol. 4, no. 1, pp. 16–25, 2013.

[47] A. Khudchenko, R. Hesper, A. M. Baryshev, J. Barkhof, and F. P. Mena, "Modular 2SB SIS receiver for 600–720 GHz: Performance and characterization methods," *IEEE Transactions on Terahertz Science and Technology*, vol. 7, no. 1, pp. 2–9, 2016.

[48] Y. Tang, N. Wadefalk, J. W. Kooi, J. Schleeh, G. Moschetti, P.-Å. Nilsson, A. Pourkabirian, E. Cha, S. Tuzi, and J. Grahn, "Cryogenic W-band LNA for ALMA band 2+ 3 with average noise temperature of 24 K," in *2017 IEEE MTT-S International Microwave Symposium (IMS)*, pp. 176–179, IEEE, 2017.

[49] D. Cuadrado-Calle, D. George, G. A. Fuller, K. Cleary, L. Samoska, P. Kangaslahti, J. W.

Kooi, M. Soria, M. Varonen, R. Lai, *et al.*, "Broadband MMIC LNAs for ALMA band 2+ 3 with noise temperature below 28 K," *IEEE Transactions on Microwave Theory and Techniques*, vol. 65, no. 5, pp. 1589–1597, 2017.

[50] J. Ding, Y. Zhao, J.-X. Ge, and S. Shi, "A 90^{o} waveguide hybrid with low amplitude imbalance in full W-Band," *Journal of Infrared, Millimeter, and Terahertz Waves*, vol. 40, no. 4, pp. 429–434, 2019.

[51] F. Xu, G. Guo, E. Li, and J. Wu, "An ultra-broadband 3-dB power divider," in *Proceedings of 2012 5th Global Symposium on Millimeter-Waves*, pp. 347–350, IEEE, 2012.

[52] D. Pukala, L. Samoska, T. Gaier, A. Fung, X. Mei, W. Yoshida, J. Lee, J. Uyeda, P. Liu, W. Deal, *et al.*, "Submillimeter-wave InP MMIC amplifiers from 300–345 GHz," *IEEE Microw. Wireless Compon. Lett*, vol. 18, no. 1, pp. 61–63, 2008.

[53] R. Lai, X. Mei, W. Deal, W. Yoshida, Y. Kim, P. Liu, J. Lee, J. Uyeda, V. Radisic, M. Lange, *et al.*, "Sub 50 nm InP HEMT device with fmax greater than 1 THz," in *2007 IEDM*, pp. 609–611, IEEE, 2007.

[54] H.-J. Song, H. Matsuzaki, and M. Yaita, "Sub-millimeter and terahertz-wave packaging for large chip-width MMICs," *IEEE Microw. Wireless Compon. Lett*, vol. 26, no. 6, pp. 422–424, 2016.

[55] A. Hassona, V. Vassilev, A. U. Zaman, V. Belitsky, and H. Zirath, "Compact Low-Loss Chip-to-Waveguide and Chip-to-Chip Packaging Concept Using EBG Structures," *IEEE Microw. Wireless Compon. Lett*, vol. 31, no. 1, pp. 9–12, 2021.

[56] D. Henke, F. Jiang, and S. Claude, "Mode suppressing packaging for 50 GHz cryogenic low-noise amplifiers," in *2012 42nd Eur. Microw. Conf.*, pp. 623–626, IEEE, 2012.

[57] P.-S. Kildal, A. Zaman, E. Rajo-Iglesias, E. Alfonso, and A. Valero-Nogueira, "Design and experimental verification of ridge gap waveguide in bed of nails for parallel-plate mode suppression," *IET Microw. Antennas Propag.*, vol. 5, pp. 262–270(8), February 2011.

[58] N. Memeletzoglou, C. Sanchez-Cabello, F. Pizarro-Torres, and E. Rajo-Iglesias, "Analysis of periodic structures made of pins inside a parallel plate waveguide," *Symmetry*, vol. 11, no. 4, 2019.

[59] F. Pizarro, C. Sánchez-Cabello, J.-L. Vazquez-Roy, and E. Rajo-Iglesias, "Considerations of impedance sensitivity and losses in designing inverted microstrip gap waveguides," *AEU - Int. J. Electron. Commun.*, vol. 124, p. 153353, 2020.

[60] A. Algaba Brazalez, A. U. Zaman, and P. Kildal, "Improved microstrip filters using PMC packaging by lid of nails," *IEEE Trans. Compon. Packag. Manuf. Technol.*, vol. 2, no. 7, pp. 1075–1084, 2012.

[61] J. Zhang, X. Zhang, D. Shen, and K. Wu, "Gap waveguide PMC packaging for a SIW-GCPW-based filter," *IEEE Microw. Wireless Compon. Lett*, vol. 26, no. 3, pp. 159–161, 2016.

[62] A. Gonzalez, T. Kojima, K. Kaneko, and S. Asayama, "275–500 GHz waveguide diplexer to combine local oscillators for different frequency bands," *IEEE Transactions on Terahertz Science and Technology*, vol. 7, no. 6, pp. 669–676, 2017.

[63] H. H. Nguyen, D. M. Luong, and G. D. Bach, "A novel independently biased 3-stack GaN HEMT configuration for efficient design of microwave amplifiers," *Appl. Sci.*, vol. 9, no. 7, p. 1510, 2019.

[64] J. JCGM *et al.*, "Evaluation of measurement data—guide to the expression of uncertainty in measurement," *Int. Organ. Stand. Geneva ISBN*, vol. 50, p. 134, 2008.

[65] S. Srikanth and A. Kerr, "Waveguide quadrature hybrids for ALMA receivers," *ALMA Memo*, vol. 343, 2001.

[66] P. Yagoubov, T. Mroczkowski, V. Belitsky, D. Cuadrado-Calle, F. Cuttaia, G. Fuller, J.-D. Gallego, A. Gonzalez, K. Kaneko, P. Mena, *et al.*, "Wideband 67- 116 ghz receiver development for alma band 2," *Astronomy & Astrophysics*, vol. 634, p. A46, 2020.

[67] A. R. Kerr, S.-K. Pan, S. M. X. Claude, P. Dindo, A. W. Lichtenberger, J. E. Effland, and E. F. Lauria, "Development of the ALMA Band-3 and Band-6 sideband-separating sis mixers," *IEEE Transactions on Terahertz Science and Technology*, vol. 4, no. 2, pp. 201–212, 2014.

[68] S. Asayama, T. Takahashi, K. Kubo, T. Ito, M. Inata, T. Suzuki, T. Wada, T. Soga, C. Kamada, M. Karatsu, Y. Fujii, Y. Obuchi, S. Kawashima, H. Iwashita, and Y. Uzawa, "Development of ALMA Band-4 (125–163-GHz) receiver," *Publications of the Astronomical Society of Japan*, vol. 66, no. 3, pp. 57–57, 2014.

[69] V. Belitsky, M. Bylund, V. Desmaris, A. Ermakov, S.-E. Ferm, M. Fredrixon, S. Krause, I. Lapkin, D. Meledin, A. Pavolotsky, *et al.*, "Alma band 5 receiver cartridge-design, performance, and commissioning," *Astronomy & Astrophysics*, vol. 611, p. A98, 2018.

[70] S. Mahieu, D. Maier, B. Lazareff, A. Navarrini, G. Celestin, J. Chalain, D. Geoffroy, F. Laslaz, and G. Perrin, "The ALMA Band-7 cartridge," *IEEE Transactions on Terahertz Science and Technology*, vol. 2, no. 1, pp. 29–39, 2012.

[71] N. Satou, Y. Sekimoto, Y. Iizuka, T. Ito, W.-L. Shan, T. Kamba, K. Kumagai, M. Kamikura, Y. Tomimura, Y. Serizawa, S. Asayama, and M. Sugimoto, "A Submillimeter Cartridge-Type Receiver: ALMA Band 8 (385–500 GHz) Qualification Model," *Publications of the Astronomical Society of Japan*, vol. 60, pp. 1199–1207, 10 2008.

[72] F. P. Mena, J. W. Kooi, A. M. Baryshev, C. F. J. Lodewijk, T. Zijlstra, R. Hesper, G. Gerlofsma, T. M. Klapwijk, and W. Wild, "Design and performance of a 600–720-GHz sideband-separating receiver using AlO_x and AlN SIS junctions," *IEEE Transactions on Microwave Theory and Techniques*, vol. 59, no. 1, pp. 166–177, 2011.

[73] J. Reed, "The multiple branch waveguide coupler," *IRE Transactions on microwave theory and techniques*, vol. 6, no. 4, pp. 398–403, 1958.

[74] H. Rashid, D. Meledin, V. Desmaris, and V. Belitsky, "Novel waveguide 3 dB hybrid with

improved amplitude imbalance," *IEEE microwave and wireless components letters*, vol. 24, no. 4, pp. 212–214, 2014.

[75] H. Rashid, V. Desmaris, V. Belitsky, M. Ruf, T. Bednorz, and A. Henkel, "Design of wideband waveguide hybrid with ultra-low amplitude imbalance," *IEEE transactions on terahertz science and technology*, vol. 6, no. 1, pp. 83–90, 2015.

[76] G. Fuller, A. Avison, M. Beltran, V. Casasola, P. Caselli, C. Cicone, F. Costagliola, C. De Breuck, L. Hunt, I. Jimenez-Serra, *et al.*, "The science case for ALMA Band 2 and Band 2+ 3," *arXiv preprint arXiv:1602.02414*, 2016.

[77] D. F. Williams, J. Jargon, U. Arz, and P. Hale, "Rectangular-waveguide impedance," in *2015 85th Microwave Measurement Conference (ARFTG)*, pp. 1–5, IEEE, 2015.

[78] Keysight, "Calibration thru methods." `https://na.support.keysight.com/pna/help/latest/S3_Cals/Calibration_THRU_Methods.htm#UnknownThru`, 2022. Accessed: 2021-10-12.

[79] M. Carter, B. Lazareff, D. Maier, J.-Y. Chenu, A.-L. Fontana, Y. Bortolotti, C. Boucher, A. Navarrini, S. Blanchet, A. Greve, *et al.*, "The EMIR multi-band mm-wave receiver for the IRAM 30-m telescope," *Astronomy & Astrophysics*, vol. 538, p. A89, 2012.

[80] Vadatech, "AMC590 datasheet." `https://www.vadatech.com/media/AMC590_AMC590_Datasheet.pdf`, 2020. Accessed: 2021-12-14.

[81] G. Kefalas, "Frequency diplexing with waveguide bifurcations," *IRE Transactions on Microwave Theory and Techniques*, vol. 10, no. 3, pp. 221–222, 1962.

[82] D. Montofre, A. Khudchenko, F. P. Mena, R. Hesper, and A. M. Baryshev, "Single-layer dichroic filters for multifrequency receivers at THz frequencies," *IEEE Transactions on Terahertz Science and Technology*, vol. 10, no. 6, pp. 690–697, 2020.

[83] I. Barrueto, "Development of microwave devices for millimeter and sub-millimiter receivers," Master's thesis, Universidad de Chile, 2017.

[84] J. Kooi, G. Chattopadhyay, S. Withington, F. Rice, J. Zmuidzinas, C. Walker, and G. Yassin, "A full-height waveguide to thin-film microstrip transition with exceptional RF bandwidth and coupling efficiency," *International Journal of Infrared and Millimeter Waves*, vol. 24, no. 3, pp. 261–284, 2003.

[85] G. Anand, R. Lahiri, and R. Sadhu, "Wide band microstrip to microstrip vertical coaxial transition for radar & EW applications," in *2016 Asia-Pacific Microwave Conference (APMC)*, pp. 1–4, IEEE, 2016.